The Local Structure of Sodium-Ion Anodes During Electrochemical Reactions

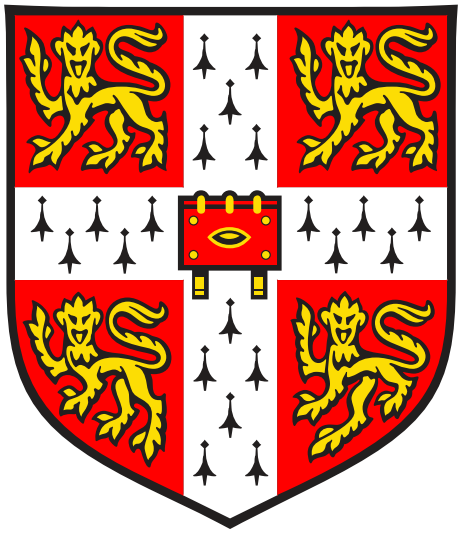

This dissertation is submitted for the degree of Doctor of Philosophy

Joshua Michael Stratford

Robinson College
Department of Chemistry
University of Cambridge

September 2018

This dissertation is the result of my own work and includes nothing which is the outcome of work done in collaboration except as declared in the Preface and specified in the text. It is not substantially the same as any that I have submitted, or, is being concurrently submitted for a degree or diploma or other qualification at the University of Cambridge or any other University or similar institution except as declared in the Preface and specified in the text. I further state that no substantial part of my dissertation has already been submitted, or, is being concurrently submitted for any such degree, diploma or other qualification at the University of Cambridge or any other University or similar institution except as declared in the Preface and specified in the text. It does not exceed the 60,000 word limit prescribed by the Degree Committee for the Faculty of Physics and Chemistry.

Joshua Michael Stratford
September 2018

Abstract

Sodium-ion batteries are seen as an increasingly attractive option for large-scale energy storage, the rising price, and limited availability of lithium being seen as a major challenge for the future of the dominant lithium systems. One of the major bottlenecks for the commercialisation of sodium-ion technology is to find a suitable anode material. This search is hampered owing to major gaps in our understanding of how these systems work. The major objective of this thesis is to gain a better understanding of the mechanisms by which sodium inserts into different anode materials.

Two systems are studied: hard carbons are widely viewed as the most promising anode material in the near future, yet the sodium insertion mechanism is still widely debated. Secondly, tin represents one of the highest capacity anode materials, able to achieve a 847 $mA\,h\,g^{-1}$, with numerous electrochemical features suggesting an interesting (dis)charge mechanism. It has previously been shown that both of these systems proceed through disordered phases, and as such, we focus on pair distribution function analysis (PDF) and solid-state NMR as local structure probes for our structural characterisation. Furthermore, to avoid relaxation effects in metastable intermediates, much of this work uses *operando* methods.

We present evidence from *operando* ^{23}Na NMR that sodium inserts into hard carbon in a two-stage mechanism: the first stage is consistent with charge localisation; after which the ions become progressively more metallic. We further investigate the structure of the pristine carbon, using PDF to demonstrate that the graphene-like fragments exhibit significant curvature. This work is then extended to a number of different carbons, both commercially made and synthesised from glucose. We present a novel method to fit PDF data for the pristine materials: using curved aperiodic, stacked graphene layers to generate the simplest model (fewest number of atoms) that explains all features of the data. *Operando* measurements are presented that demonstrate expansion of the shortest C–C bonds during the first electrochemical process, along with the formation of sodium nano-clusters during the second.

We then apply this novel multi-modal approach to tin anodes. We find that sodium insertion begins by conversion into $NaSn_2$, a phase consisting of stanene layers separated by sodium ions. This is then broken down into an amorphous phase, where reverse Monte Carlo refinements show that the predominant tin connectivity is chains. Further reaction with sodium results in structures containing Sn-Sn

dumbbells, which interconvert through a solid-solution mechanism. Finally, we show that $Na_{15}Sn_4$, can store additional sodium atoms as an off-stoichiometry compound ($Na_{15+x}Sn_4$). The sodium removal (charge) process is shown to begin by forming Sn–Sn dumbbells in a structure similar to the discharge phase, but with a lower sodium content (Na_2Sn). Following this, the structure loses all long-range order. We show, through refinements of suitable models against *operando* PDF data, that the dumbbells are retained, but later transform into a second amorphous phase consisting of tin tetrahedra. Finally, we show that β-tin reforms, with no intermediate analogous to $NaSn_2$. We additionally demonstrate a substantial degree of kinetic control in these (de)alloying reactions.

Acknowledgements

Firstly, and most importantly, I would like to thank my supervisor, Professor Clare Grey, for giving me the opportunity to complete this research. I am extremely grateful for our many interesting and thought-provoking discussions, as well as for making the whole PhD an enjoyable experience. Secondly, to Dr Phoebe Allan, much of the success of this work is thanks to her support, guidance and friendship over the last four years.

Much of the work presented here would not have been possible without the excellent assistance of a number of beamline scientists. In particular I would like to thank Drs Phil Chater and Dean Keeble from I15-1 (XPDF) at Diamond Light Source, and Dr Annette Kleppe at I15, along with Drs Karena Chapman, Olaf Borkiewicz, and Kamila Wiaderek from sector 11 at the Advanced Photon Source.

Several areas of this research were completed in collaboration with external researchers. I would like to thank Drs Andrew Morris and Martin Mayo, whose DFT calculations formed the basis for many of the crystallographic refinements presented here. Many thanks also go to both past and present Grey group members for helping me in countless ways and making each day in the lab enjoyable. In particular, to Dr Oliver Pecher without whose expertise the operando NMR measurements would not have been possible.

I further acknowledge funding from the U.S. DOE under Contract no. DE-AC02--05CH11231, under the BATT Program (no. 7057154), the European Commission (grant no. 696656), and an STFC Futures Early Career Award from STFCBatteries.org. I am also grateful to beamlines 11-ID-B at the Advanced Photon Source, I15 and I15-1 at Diamond Light Source for the provision of beamtime that has enabled this work.

Finally, a special thanks to my family and friends, in particular to my parents for their continual support and encouragement, and to my two brothers for many discussions both scientific and otherwise. You have helped me through the many high and low points over the last few years.

List of Abbreviations

A

AIRSS *Ab Initio* Random Structure Searching

AMPIX Argonne's Multi-Purpose *In Situ* X-ray

C

CMC Carboxymethyl Cellulose

CQ Quadrupole Coupling

CSA Chemical Shift Anisotropy

D

DAWN Data Analysis WorkbeNch

DFT Density Functional Theory

E

EMF Electromotive Force

F

FID Free-Induction Decay

G

GIC Graphite Intercalation Compound

GITT Galvanostatic Intermittent Titration Technique

I

ICSD Inorganic Crystal Structure Database

L

LIB Lithium-Ion Battery

M

MAS Magic Angle Spinning

MD Molecular Dynamics

N

NIB Sodium-Ion Battery

NMR Nuclear Magnetic Resonance

O

OCV Open Circuit Voltage

P

PDF Pair Distribution Function (analysis)

PHS Pump-Hydro-System

PITT Potentiostatic Intermittent Titration Technique

PXRD Powder X-Ray Diffraction

R

RDF Radial Distribution Function

RF Radio Frequency

RMC Reverse Monte Carlo

S

SAXS Small-Angle X-ray Scattering

SEI Solid-Electrolyte Interphase

SHE Standard Hydrogen Electrode

ssNMR Solid-State NMR

T

TEM Transmission Electron Microscopy

X

XRD X-Ray Diffraction

Table of Contents

1 Introduction

The rapidly accelerating demand for electricity is producing a tremendous strain on the planet's resources. These problems extend beyond merely using up the limited available quantities of non-renewable fuels; for example, combustion releases gases, such as CO_2, which are harmful to the environment and contribute to climate change. Hydroelectric dams may disrupt nearby marine life, and the use of biofuels may result in further deforestation and increased pollution upon their combustion. Clean means of electricity generation, such as solar and wind, do exist, but their output can not easily be controlled to match consumer demand. Figure 1.1a shows the UK's electricity generation capacity in 2017 — just 13% of the UK's needs are currently met by these clean sources.[1] A further shift towards such environmentally benign means of production requires the development of low-cost energy storage technologies. This would allow energy to be stored during periods when demand is low, and used when production cannot meet demand. Globally, the majority (approximately 99%) of such storage is provided using pump-hydro-systems (PHSS) (see Figure 1.1b for the UK),[2] however, the development of new sites is geographically restricted, and the power and energy density cannot match that of electrochemical storage systems.[3]

Broadly speaking, there are two major types of electrochemical storage systems: flow batteries — where redox reactions occur at a membrane over which an electrolyte flows on each side, the electrolytes typically being stored in large tanks — and ion batteries — where ions shuttle between two electrodes. Ion batteries themselves can be subdivided based on

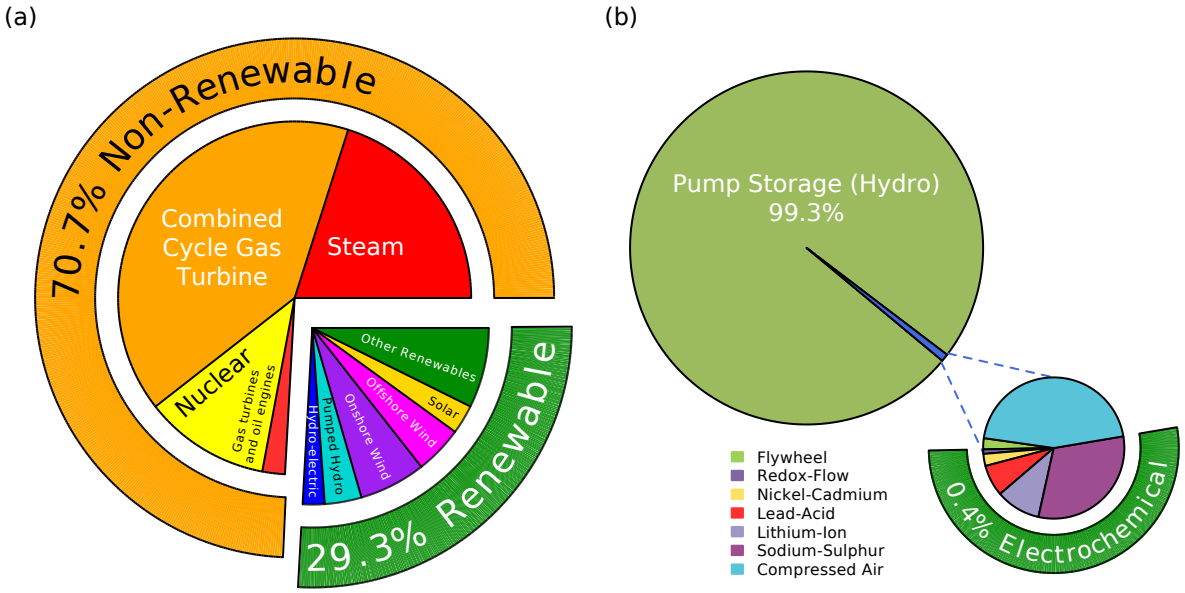

Figure 1.1: (a) Breakdown of the UK's electricity generation capacity from 2017; data from ref 1. (b) Breakdown of the UK's grid-level electricity storage capacity from 2014; data from ref 4.

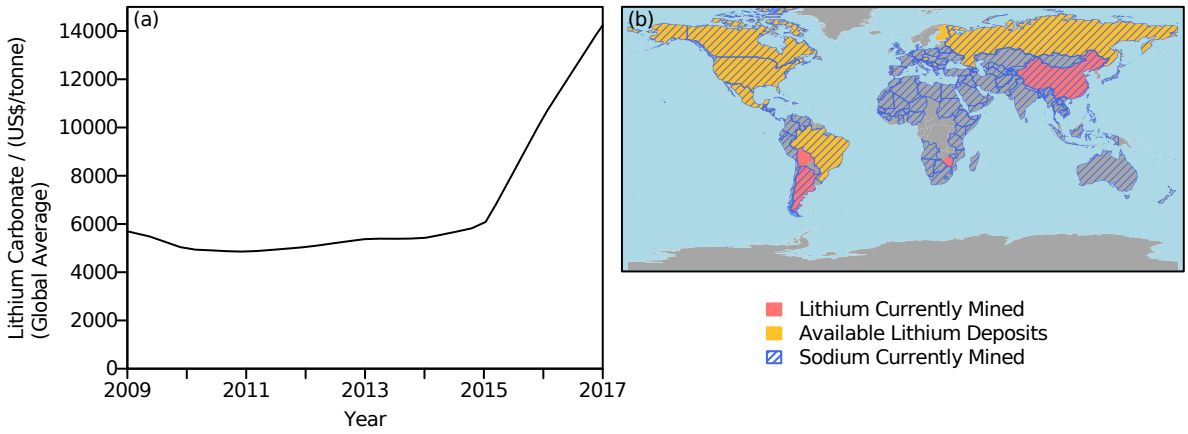

Figure 1.2: (a) Changes to the cost of lithium carbonate over the last decade; data from ref 15. (b) Geographic availability of lithium and sodium. Countries where lithium is currently mined are shown in red, those with un-mined deposits in yellow. Countries in which sodium is currently mined are shaded in blue; data from ref 16.

the ion which is shuttled. Lithium-ion batteries (LIBs) are the most common having been commercialised almost 30 years ago;[5,6] their very high energy density being a strong draw both at the time, and still to this day. Research into sodium-ion batteries (NIBs) lags a little behind, having not really taken-off until the early 2000s (although they were briefly explored prior to the commercialisation of LIBs). Other ion-batteries such as magnesium, calcium and potassium remain in their infancy, but offer promise in terms of energy density and / or cost for the future. It is this more comprehensive understanding of the chemistry and processes involved in the production and running of LIBs that has kept LIBs the dominant means of electrochemical storage on both the small-scale (laptops, mobile telephones etc.) and larger-scale (electric vehicles, grid-level storage).

1.1 Sodium-Ion Batteries

Despite the advantages of LIBs, the low abundance of lithium is likely to cause issues in the near future. The total amount of lithium available is estimated to lie between 12 to 64 million tonnes.[7–12] Current expectations suggest that demand will exceed supply by 2050, or 2100 if significant recycling efforts are started before 2025.[13] Clearly, any such estimate is based upon significant assumption regarding projected Li demand, particularly as the future use cases for these batteries shifts towards cars and large-scale grid storage, both of which place heavy demands on lithium supplies. However, even in the short-term, the difficulty in increasing production to meet demand has led to significant volatility in the price of lithium (Figure 1.2a). Furthermore, commercial cathode materials commonly contain nickel and cobalt, both of which pose an even greater risk of depletion than lithium itself.[14]

Sodium presents an obvious choice for an alternative to lithium. It is chemically similarity, which should allow for a degree of overlap in the types of systems that can be used as effective

battery materials. It is also vastly more abundant, and geographically diverse (Figure 1.2b), which avoids any concern over future availability, and should help to prevent price fluctuations caused by variability in demand. In addition, the state-of-the-art cathode materials for NIBs employ iron rather than nickel or cobalt,[17] further reducing production costs. Finally, aluminium suffers from an alloying reaction with lithium at low potentials that prevents its use as a current collector on the negative electrode side. This means that a more expensive copper current collecter is required for LIBs. This reaction does not occur in NIBs allowing for the use of inexpensive aluminium current collectors on both electrodes.

Disadvantages of NIBs arrise due to the larger ionic radius of sodium (1.02 Å)[18] compared to lithium (0.76 Å)[18] and its higher redox potential (Na: −2.71 V *vs.* standard hydrogen electrode (SHE); Li: −3.04 V *vs.* SHE).[18] Combined, these limit the the achievable energy density of NIBs *vs.* LIBs. It should be noted, however, that there are other interactions present in the host structure which will be different for lithium and sodium (such as the rate of diffusion of ions through the structure). These provide a potential avenue whereby sodium-based technology may surpass its lithium analogue.[19] Indeed, there have been reports of systems which do not perform well with lithium, but perform much better with sodium as the larger size of sodium ions can help to stabilize layered structures.[20]

Currently, the main potential applications for NIBs are seen as those in which the cost of the batteries themselves is more important than the physical footprint of the device — grid storage systems, for example. In addition, the environmental benignity of sodium is seen as an attractive virtue for these devices. Size-critical devices such as mobile phones and other portable electronics are not seen as an area in which sodium-based technology can offer any real advantages.

1.2 Mechanisms of Sodium Insertion

Several possible mechanisms for sodium storage are summarized in Figure 1.3. The most straightforward of these is the intercalation mechanism: the redox reactions take place without large scale changes to the host structure (the bonds of the host structure — typically a metal oxide framework — are not broken). Instead, they proceed via the reversible intercalation of ions into tunnels or between layers in the structure. This often leads to materials with a very high-cycle stability, but a lack of storage capacity when compared with the other mechanisms. Conversion materials are of the form M_aY_b, where M is a transition metal and Y is O, S, F, P, N, etc. In these systems, the metal is fully reduced during sodium insertion – which requires multiple electrons per atom – leading to high capacities. The resulting structure is a Na_xY matrix with embedded metallic nanoparticles. However, the large volume expansion resulting from the incorporation of a large number of sodium ions can result in physical damage to the electrode in the form of cracking or desorption from the current collector. In addition, a large voltage hysteresis is often observed between charge and discharge; these factors result in a loss of capacity leading to poor energy efficiency. Alloying reactions result in the formation of Na_xM structures during sodium insertion, the reaction

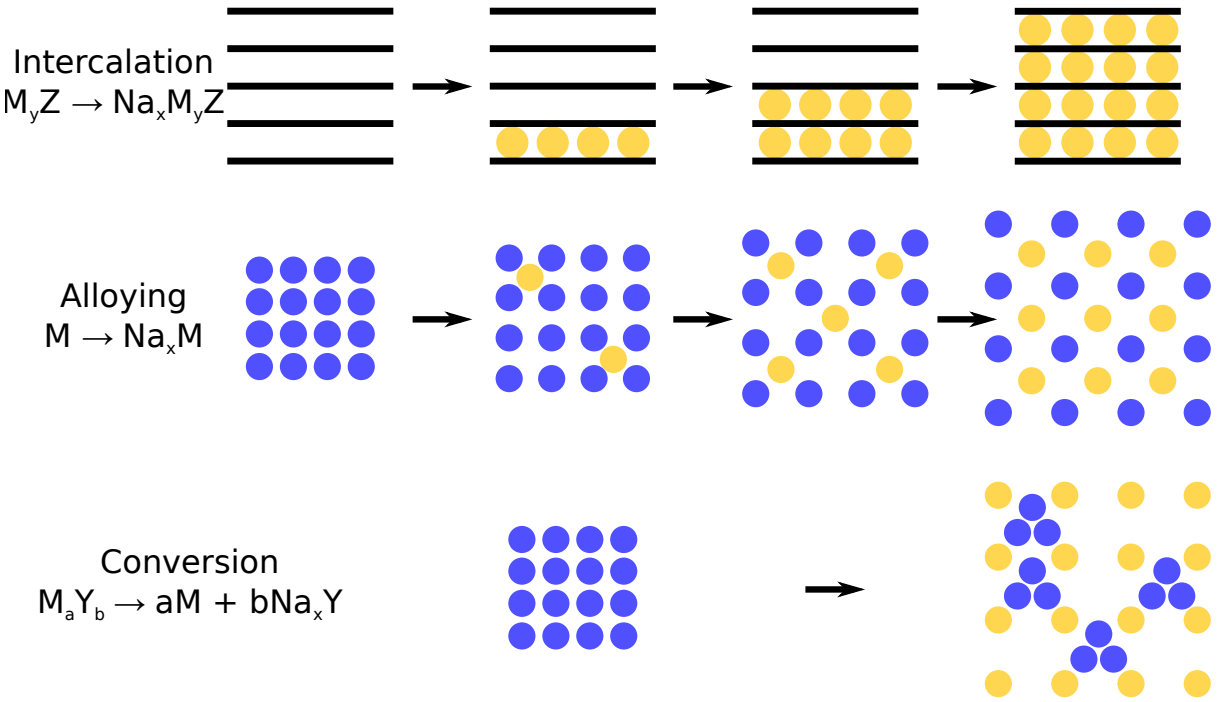

Figure 1.3: A schematic showing the possible reaction mechanisms for sodium-ion batteries. The blue circles represent metal atoms and the yellow circles sodium. Black lines represent electrode (usually metal-oxide) layers.

may proceed via several of these structures allowing the incorporation of a large number of sodium ions. It offers similar benefits and suffers from similar problems to conversion materials.

1.3 Anode Materials

The anode material offering the highest theoretical capacity is metallic sodium. However, similar to lithium metal, it has a tendency to form dendritic structures when sodium is repeatedly stripped and replated, eventually causing short-circuits.[21] The safety of sodium metal is further brought into question by its low melting point (97.7 °C *vs.* 180.5 °C for lithium). Graphite is used as the anode material for almost all commercial LIBs, however, it is ineffective for NIBs.[22–25] There is some debate in the literature as to why this is the case. It is often stated that the larger ionic radius of sodium prevents intercalation,[26–28] however, potassium, rubidium and caesium can all be intercalated into graphite,[29] even electrochemically in the case of potassium.[30] Recent density functional theory (DFT) calculations suggest that the inability of sodium to form graphite intercalation compounds (GICs) is a result of the charge transfer from sodium to the carbon structure being abnormally low in energy,[31] leading to sodium-plating being more exothermic. As a result, there is an ongoing search for a suitable alternative that cycles well, and remains cost-effective.

Disordered carbons have so far been the most popular choice of anode material for NIBs; indeed the feasibility of sodium-ion systems was first proven by Doeff *et al.* in 1993 using such

anodes.[23] There has been continued interest into improving these materials such that they may achieve higher capacities and performance comparable to similar lithium systems. Given carbon's low cost, and non-toxicity, it is a highly attractive choice for companies seeking to commercialise sodium-ion technology. Indeed, three decades of research into lithium anode materials has found many capable of improving on the energy density of carbon based materials on the lab scale, but none have yet been able to be incorporated into commercial cells. It is sensible to assume that the development of commercial NIBs will follow a similar path, with the first anode material being carbonaceous. These carbons themselves have been the subject of much study during the last century (Rosalind Franklin being an early pioneer of this work)[32] and in the battery community for several decades. However, despite this there still remains a great deal of uncertainty regarding the mechanisms of sodium (and lithium) insertion into them, and indeed their very structure. A great deal of work is ongoing in an attempt to answer these questions.[33]

Whilst carbon based materials may be the furthest along in their development, the capacity they are able to achieve is relatively limited (typically 200–300 $\mathrm{mA\,h\,g^{-1}}$).[34] Moving to an alloying, or conversion material allows for a significant increase in capacity. In the lithium case, graphite can only host one lithium ion per six carbon atoms, alloys can allow for up to four lithium ions per metal atom.[35–37] The vastly increased volumetric energy storage capacity makes these materials highly attractive candidates for anode materials. However, there remain significant problems in terms of capacity fade during cycling that must first be overcome. Whilst research into sodium-based alloy materials is not as advanced as that for lithium systems, tin and antimony based systems have been considered.[38–41] They offer a very high first cycle capacity (e.g. $\sim$847 $\mathrm{mA\,h\,g^{-1}}$ for tin)[38] but suffer from a large capacity fade per cycle due to a large volume expansion upon sodium insertion. The structural changes underlying these capacities, i.e. where the sodium ions insert, are often unknown. Only recently has there been interest in the literature in unravelling the (often complex) mechanisms, which has proven particularly challenging due to the prevalence of disordered phases with no long-range ordering in many of these systems.[42] Recently, there has been a drive towards searching for more novel materials,[43] for example amorphous germanium – derived by first undergoing a single lithiation / delithiation cycle with crystalline germainium – has recently been reported.[44] A very promising material for lithium-ion batteries is silicon. Whilst it shows no reversible capacity with sodium,[45] there has recently been a report on the theoretical viability of amorphous silicon,[46] although no experimental evidence has been reported to date.

1.4 Overview of this Thesis

Chapter 2 presents an overview of the different experimental techniques used in this work, and the theory underlying each method. Chapter 3 contains a preliminary investigation into the mechanisms by which sodium is stored within hard carbon anode materials. Two different local structural probes are used to investigate the structure and charge storage ability of a commercial hard carbon. This work is expanded upon in chapter 4 where we

expand the analysis to additional carbons, and further our analysis of the mechanisms. In chapter 5, we investigate the alloying material tin. We address its complex discharge (sodium insertion) mechanism, proposing possible structures for each of the eight stages. This work is continued in chapter 6 where we attempt to unravel the sodium removal processes. Finally, a brief summary of the conclusions from this work and possible future work is given in chapter 7.

2 Experimental Methods

2.1 Electrochemical Energy Storage

Batteries store energy through redox reactions at their electrodes. Discharging the cell causes reactants to be chemically oxidized at the anode (negative electrode); this results in the release of ions into the electrolyte. These ions are then transported, through the electrolyte, to the cathode (positive electrode), which is reduced.[47] A schematic of this process is shown in Figure 2.1. The corresponding Gibbs free energy change is given by $\Delta G = -\nu F E$, where ν is the number of electrons, F is the Faraday constant, and E is the cell potential (also known as the electromotive force, or EMF), which is given by the Nernst equation:[48]

$$E = E^{\ominus} - \frac{RT}{\nu F} \ln\left(\frac{a_{\text{products}}}{a_{\text{reactants}}}\right) \tag{2.1}$$

where $E^{\ominus}$ is the standard cell potential, R is the molar gas constant, and a is the chemical activity of the relevant species.

In order to make comparisons between different systems, it is necessary to measure the potential of the electrodes *vs.* a reference potential. The SHE is defined to be 0 V,[49] however, the challenges imposed through the use of this electrode mean that it is not commonly used. Instead, for alkali-ion batteries, it is typical to measure the cell potential *vs.* that of the pure

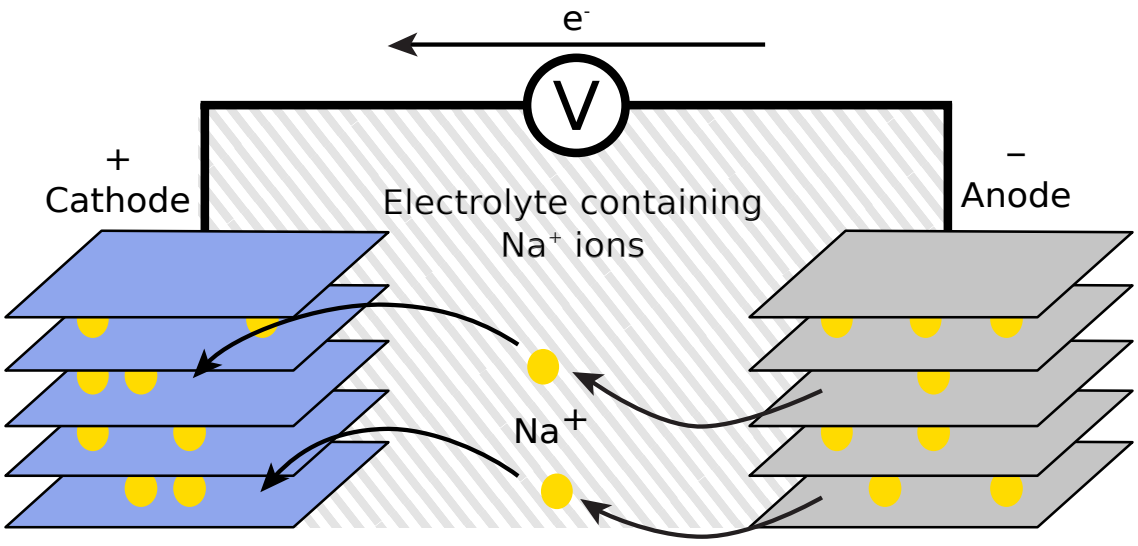

Figure 2.1: Schematic representation of energy storage in a sodium-ion battery.

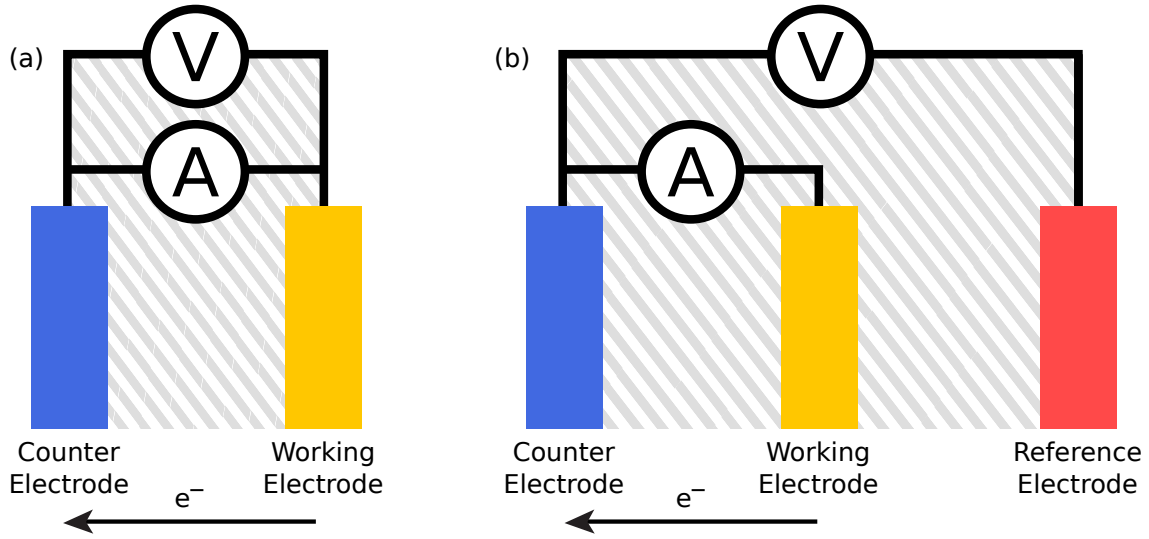

Figure 2.2: Schematic representation of measurements in (a) a two electrode (half-cell) configuration and (b) a three-electrode configuration.

alkali metal. These measurements can be performed using either a half-cell configuration, in which the reference electrode is also a working electrode, or a three electrode configuration in which the reference electrode does not take part in the redox processes. A diagram showing these two systems is given in Figure 2.2. In practical applications, half-cell configurations (those with an alkali metal working electrode) are not safe owing to the possibility of dendrite formation,[50] however, a standardised reference potential is not required at this stage, as battery management circuitry can be calibrated directly against the cell potential.

As stated earlier, the cell potential is given by the Nernst equation (equation 2.1). For a battery containing two solid electrodes in the same electrolyte solution, this simplifies to $E = E^{\ominus}$ in the ideal case. A change in the measured cell potential, E, can only, therefore, be caused by a change in the structure of one of the electrodes, or by a change in temperature. There are two possible mechanisms by which a structure may transform: a two-phase mechanism, or a solid-solution mechanism. In the case of a solid-solution mechanism, the electrode structure is different for each additional ion that reacts with it. This leads to an electrochemical profile whose potential continually decreases with time. For a two-phase reaction, each ion reacts with the same structure. The energy, and therefore potential, of this reaction does not change with time, leading to a flat plateau in the measured potential. These ideas are encapsulated within the Gibbs phase rule, which states that the number of thermodynamic parameters that must be specified in order to define the system (degrees of freedom), $F = C - P + 2$, where C is the number of components in the reaction and P is the number of phases. For a two-phase reaction, the number of degrees of freedom is 2, thus if two thermodynamic parameters are specified (temperature and pressure), then any remaining parameters (such as voltage) must be constant. Thus, we expect flat voltage plateaus whenever two phases are present. For a one-phase (solid-solution) reaction there is an additional degree of freedom and thus the voltage can vary. Figure 2.3 demonstrates the differences in the measured electrochemical profiles for these two reaction types. Sodium insertion into hard carbons gives a characteristic sloping electrochemical process (Figure 2.3a) as a result of a solid-solution mechanism,

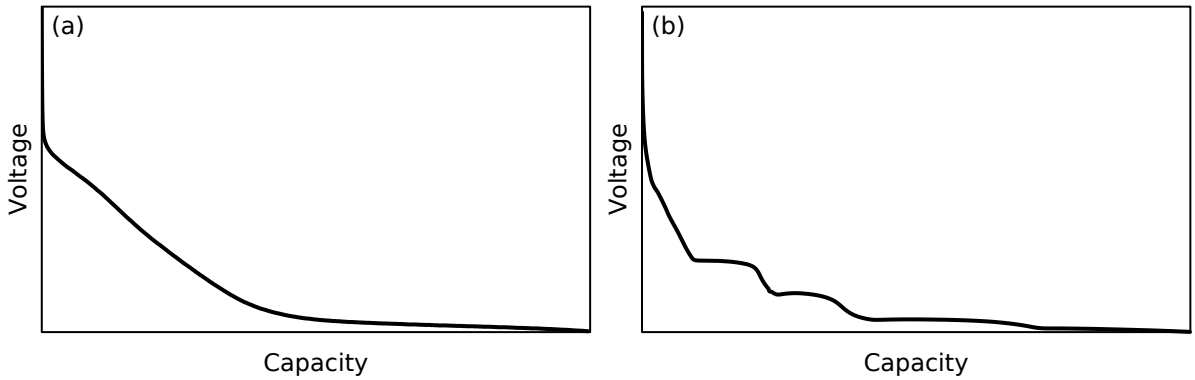

Figure 2.3: Electrochemistry data for (a) a sodium–hard carbon cell and (b) a sodium–tin cell. The sloping process in (a) implies solid-solution behaviour, whereas the flatter plateaus in (b) typically result from two-phase transformations.

whereas sodium alloying with tin gives numerous flatter plateau processes (Figure 2.3b). The underlying structural changes will be discussed in greater detail in chapters 3 and 5.

2.1.1 Experimental Considerations

Cells are most commonly cycled using a galvanostatic (constant current) mode. This results in the insertion of a constant number of ions into (or out of) the electrode per unit time. There exist numerous methods for describing the magnitude of the applied current such that comparisons can be made across samples whose mass and / or surface area differ. The simplest such methods simply divide the current by the mass or surface area to give values in $\mathrm{A\,g^{-1}}$ or $\mathrm{A\,cm^{-2}}$. More common are descriptions that relate the current to the amount of time that a process takes. There exist two incompatible nomenclature systems for rates described in this manner, in both cases the rate is described as $\frac{\mathrm{C}}{x}$. In the first case x refers to the number of hours it takes for one mole of the alkali metal ions to react with the electrode. For example, $\frac{\mathrm{C}}{5}$ refers to adding 0.2 ions/h. The second method uses x to describe the total number of hours for which the current needs to be applied in order to reach the theoretical capacity of the cell. In this case, $\frac{\mathrm{C}}{5}$ indicates that the theoretical capacity would be reached were this current sustained for 5 hours. The latter method will be used exclusively in this work. The theoretical capacity of a cell is given by the formula: $Q = \frac{\nu F}{3600\,\mathrm{M_r}}$ where Q is the capacity in $\mathrm{A\,h\,g^{-1}}$, ν is the number of electrons, F is the Faraday constant and $\mathrm{M_r}$ is the relative molecular mass of the material. An applied current of $\frac{\mathrm{C}}{x}$ is simply the theoretical capacity divided by x hours and multiplied by the electrode mass.

Once a current has been applied to a cell, its measured potential will not be the same as its open circuit potential (often referred to as the equilibrium potential). This is because resistance within the cell results in a drop in the potential when a current is applied. This is known as an overpotential, and is represented by $\eta = E_{OCV} - E_T$, where E_{OCV} is the open circuit voltage (OCV) and E_T is the terminal voltage with a current flowing. For an ohmic resistance, the overpotential is given by $\eta = IR$, where I is the applied current, and R is the magnitude of the resistance. A component displaying non-ohmic behaviour has a more

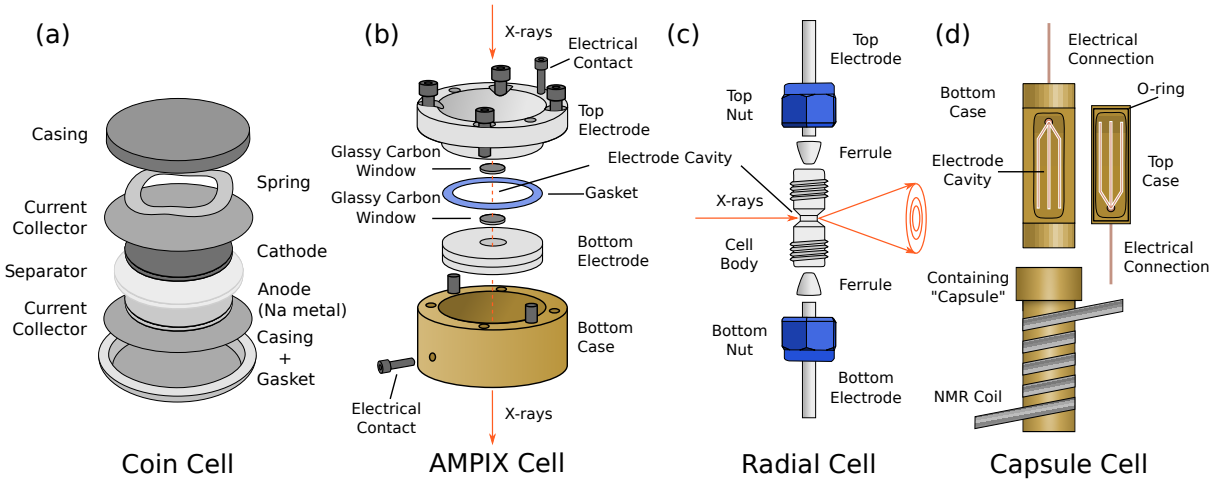

Figure 2.4: A selection of the electrochemical cells used in this work: (a) A coin cell; (b) the argonne's multi-purpose *in situ* X-ray (AMPIX) cell used for pair distribution function analysis (PDF) and powder X-ray diffraction (PXRD) measurements; (c) the radial cell used for PDF measurements and; (d) the capsule cell used for nuclear magnetic resonance (NMR) measurements.

complex dependance on the current. Typically the resistance results from a mix of ohmic and non-ohmic contributions, including: poor conductivity within the electrodes, difficulty in nucleating a new phase, and sluggish kinetics at the electrolyte / electrode interface. A large overpotential can cause difficulties for low potential systems, such as those studied in this work, where the equilibrium potential for an electrochemical process is near to the sodium plating potential (typically around 0 V *vs.* Na/Na+). A large overpotential can result in the preferential plating of sodium rather than the desired redox reaction. Overpotentials can be quantified using techniques such as galvanostatic intermittent titration technique (GITT), where a current is applied in short pulses with the system allowed to return to equilibrium in between, or potentiostatic intermittent titration technique (PITT), which uses potential rather than current pulses.[51,52]

There exist a variety of designs for electrochemical cells, some are designed exclusively for electrochemical measurements, others have been adapted to allow for additional experiments to be performed simultaneously. A selection of the cells used as part of this work are presented in Figure 2.4. Each design consists of a casing, two current collectors (these are part of the casing in some designs) and an electrically-insulating, but ionically-conducting separator. When combined with the two electrodes and the passivating solid-electrolyte interphase (SEI) layers, which grow upon them as a result of electrolyte decomposition, there may be as many as ten interfaces within a typical cell. Each of these interfaces increases the internal resistance (and thus the overpotential) of the cell.

Two of the cell designs used in this work have been adapted for X-ray transmission. The AMPIX cell, Figure 2.4b, can be used for PDF and PXRD measurements. It is designed such that the X-ray beam passes through both electrodes.[53] For lithium, this poses little problem, however, the greater scattering power of sodium along with the propensity for single crystallites within a sufficiently large piece of the metal, results in a strong background that is difficult to subtract

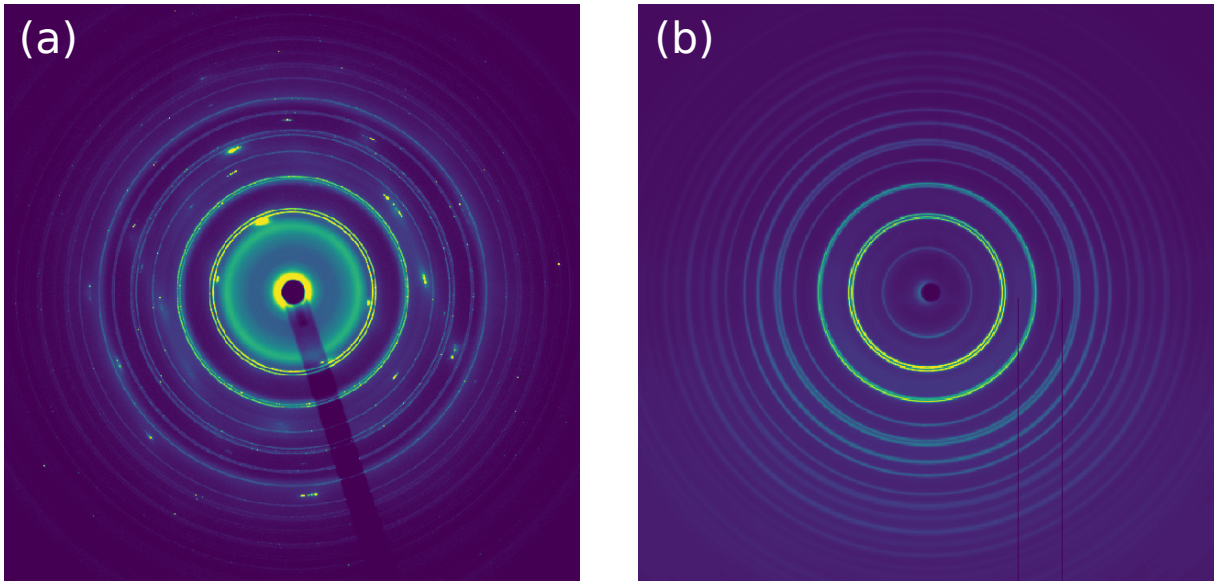

Figure 2.5: 2D diffraction patterns of sodium and tin electrodes within (a) an AMPIX cell, taken in transmission through the electrode stack, and (b) a radial cell taken in an orthogonal orientation, with the beam only passing through the tin electrode. The rings correspond principally to tin, the darker diagonal line to the beamstop, and the bright spots result from sodium single crystallites.

(Figure 2.5). The radial cell, Figure 2.4c, was developed, in part, to address this issue. The X-ray beam travels through only a single electrode, greatly simplifying the background. In addition, this geometry allows for metallic current collectors and greater pressure on the electrodes as the X-ray beam is perpendicular to the electrode stack. Both of these factors improve the electrochemical performance of the cell by reducing the overpotential. This is particularly important for materials whose reactions occur at low potentials. However, the radial geometry limits the achievable resolution for Bragg diffraction owing to the thickness of material through which the beam is travelling. It also places constraints on one or both of the thickness of the electrode of interest and the beam diameter used in order to ensure that the measured diffraction pattern results from only a single electrode.

A cell suited for NMR measurements poses very different challenges. The amount of metallic material in the cell must be greatly limited so as not to shield the radio frequency (RF) radiation from penetrating through to the electrodes. Such a constraint presents a large challenge in ensuring there is good conduction between the electrodes and the exterior of the cell, along with providing pressure to the electrode stack. The cell used for the NMR measurements in this work is presented in Figure 2.4d, it uses copper meshes to provide a connection between the interior and exterior of the cell, and rubber sheeting along with the cell casing to provide pressure to the electrode stack.

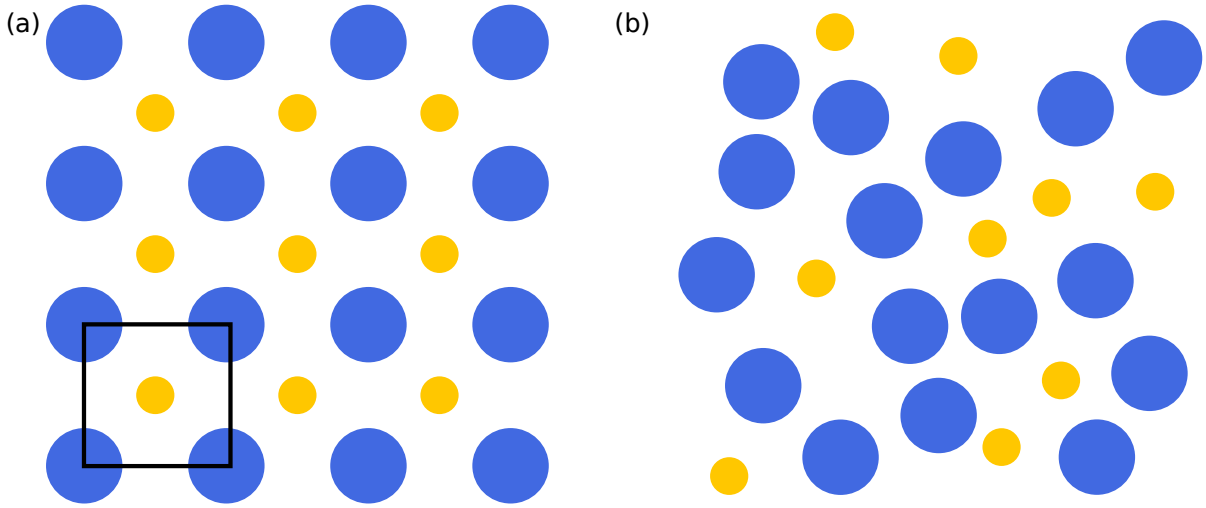

Figure 2.6: Schematics showing (a) a crystalline solid — the unit cell is marked in black — and (b) an amorphous solid.

2.2 Diffraction Methods

A crystal is an ordered array of atoms which is repeated infinitely in all directions. The structure of a crystal is periodic such that it is fully described by the contents of the repeating unit (the unit cell) and the symmetry operations of the space group to which it belongs. By contrast, an amorphous solid contains only short-range ordering. A schematic demonstrating the difference is shown in Figure 2.6. It is common for the (dis)charge mechanisms of many battery materials to include both amorphous and crystalline structures, and thus a complete description must include both local and long-range structural information.

There are three commonly used methods of diffraction: X-ray, neutron and electron. All three can provide similar information, however, each has their own distinct advantages and disadvantages, which may dictate the best method for a particular problem. Neutrons typically provide the highest quality data as they diffract primarily from the nucleus rather than the electron cloud. In addition, the neutron scattering length is not proportional to the atomic number, instead it varies much more randomly. This means that elements adjacent to each other in the periodic table are much easier to distinguish using neutron diffraction than the other methods, and lighter elements such as lithium are typically easier to see. However, neutron sources have an extremely low flux compared to X-ray and electron sources, necessitating the use of much larger amounts of material — the low absorption coefficient of neutrons being an advantage here. Such large sample volumes are very difficult to produce using electrochemical methods, and make *operando* measurements very challenging.

Electrons can be used both to image samples, and in diffraction as their charge allows them to be focused whereas X-rays and neutrons cannot form an image. However, their use poses significant challenges for the characterisation of electrochemically relevant materials. Measurements must be carried out in high vacuum owing to the strong interaction between electrons and other particles, including those in air. This makes *operando* measurements difficult as most electrolytes consist of volatile solvents. Furthermore, the very thin samples

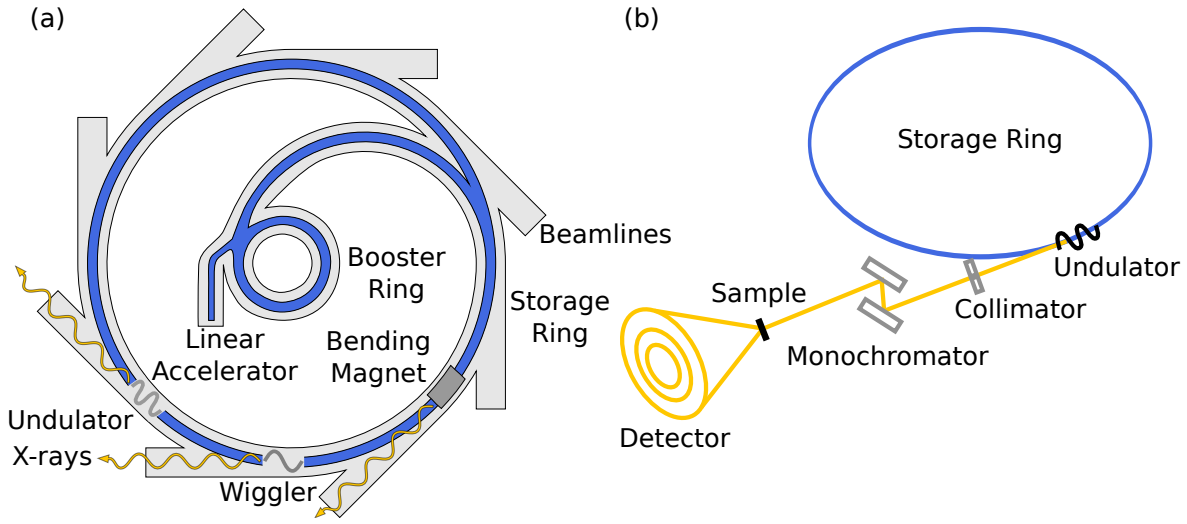

Figure 2.7: (a) A schematic of a synchrotron light source; the key features of its operation are indicated. (b) A schematic of the experimental setup at an individual beamline.

required may affect the observed (dis)charge mechanism. This work focuses on the use of X-ray diffraction in order to avoid these limitations of neutron and electron diffraction.

Whilst there exist numerous sources of X-rays, the majority of laboratory sources consist of an X-ray tube. These tubes operate by firing an electron beam at a metal target. This causes X-rays to be generated through two different methods: the majority of X-rays formed result from bremsstrahlung radiation released during the deceleration of the electrons. Secondly, when an electron collides with an inner shell electron from the metal sheet, it causes both to be ejected. An electron from a higher shell can then fill this hole, releasing an X-ray of a characteristic energy. Typically, a filter would be applied such to remove the bremsstrahlung radiation. This means that only these characteristic X-rays are used during the diffraction measurement, as the bremsstrahlung radiation is not sufficiently monochromatic.

X-ray tubes are sufficient for a large majority of routine diffraction measurements, however, if radiation is required at energies or intensities that these tubes cannot produce, a synchrotron light source is required. Accelerating an electron in an electromagnetic field causes an electromagnetic wave to be emitted. The frequency of this wave is determined by the oscillation frequency of the electron. In order to generate high energy electrons, synchrotron sources accelerate electrons to close to the speed of light, where Lorentz contraction further shortens the wavelength of the emitted radiation. A schematic showing the major components of a synchrotron is given in Figure 2.7. Electrons travel around a continuous path, the acceleration caused by bending magnets around this ring causes X-rays to be emitted. Furthermore, there are many insertion devices placed around the ring containing magnets which cause the electrons to follow an undulating path. This results in further emission of radiation. X-rays travel tangentially from the ring, where beamlines are positioned to make use of the generated X-rays. There are many beamlines around the storage ring, allowing many experiments to be performed simultaneously. These sources produce X-rays with orders of magnitude more intensity than lab sources, the beams are highly monochromatic and their energies are tuneable.

2.2.1 X-Ray Diffraction

The amplitude of scattered radiation from a general object can be described by the following equation:

$$F(\boldsymbol{Q}) = A_0 \int \rho(\boldsymbol{r}) \exp(i\boldsymbol{r}\cdot\boldsymbol{Q})\, dV_r \tag{2.2}$$

where A_0 is the maximum amplitude of the wave, $\boldsymbol{r}$ is the vector between two point scatterers, $\rho(\boldsymbol{r})$ represents the electron density, i.e. the number of electrons in the volume V_r, and $\boldsymbol{Q}$ is the scattering vector with magnitude $|\boldsymbol{Q}| = Q = 4\pi\frac{\sin\theta}{\lambda}$. Equation 2.2 represents the Fourier transform of the electron density. An inverse Fourier transform of the scattering amplitude would, therefore, recover the electron density and thus the structure of the material. However, the measured intensity of the scattered radiation is proportional to $F(\boldsymbol{Q})F^*(\boldsymbol{Q})$, which contains no information on the phase of the waves. The inverse Fourier transform cannot then be directly carried out. This is commonly referred to as the "phase problem".

For a group of atoms, equation 2.2 becomes:

$$F(\boldsymbol{Q}) = \sum_{j=1}^{N} f_j(Q) \exp(i\boldsymbol{r_j}\cdot\boldsymbol{Q}) \tag{2.3}$$

where $f_j(Q)$ is the atomic form factor of the jth atom.

The scattered radiation coming from the object can interfere in either a constructive or destructive manner. We refer to the case when scattering amplitudes add constructively as Bragg diffraction. For a regular array of atoms separated by a distance, a, constructive interference occurs when the path difference between the incident and scattered rays is equal to an integer multiple of the wavelength. This occurs when $a(\cos\alpha - \cos\alpha_0) = h\lambda$, where α and α_0 are the angles of the incident and diffracted beams, respectively, and λ is the wavelength. Equivalently, $\boldsymbol{a}\cdot\boldsymbol{q} - \boldsymbol{a}\cdot\boldsymbol{q_0} = 2\pi h$ or $\boldsymbol{a}\cdot\boldsymbol{Q} = 2\pi h$, where $\boldsymbol{Q} = \boldsymbol{q} - \boldsymbol{q_0}$. This is the Laue condition for diffraction from a one dimensional crystal, for a three dimensional crystal, there are two similar conditions for the additional dimensions. For constructive interference to occur, all three conditions must be met simultaneously, constraining $\boldsymbol{Q}$ to be of the form $\frac{\boldsymbol{Q}}{2\pi} = h\boldsymbol{a}^* + k\boldsymbol{b}^* + l\boldsymbol{c}^*$, where $\boldsymbol{a}^*$,$\boldsymbol{b}^*$ and $\boldsymbol{c}^*$ are orthogonal to $\boldsymbol{a}$, $\boldsymbol{b}$ and $\boldsymbol{c}$. This defines a reciprocal lattice. For a crystal there is also a restriction on $\boldsymbol{r_j}$: as each atom must be located within a lattice, $\boldsymbol{r_j}$ must be of the form $\boldsymbol{r_j} = x_j\boldsymbol{a} + y_j\boldsymbol{b} + z_j\boldsymbol{c}$. These constraints on $\boldsymbol{Q}$ and $\boldsymbol{r_j}$ mean that diffraction from a crystalline material can be described by the following expression:

$$F(\boldsymbol{Q}) = \sum_{j=1}^{N} f_j(Q) \exp\left(2\pi i(hx_j + ky_j + lz_j)\right) = F(hkl) \tag{2.4}$$

where $F(hkl)$ is known as the structure factor. It is a vector quantity and therefore has both amplitude and phase, however, in a diffraction experiment, only the magnitude, $|F(hkl)|$, is accessible.

The condition for diffraction can be represented much more simply by recognising that $hx_j + ky_j + lz_j$ represents a plane of atoms. This allows simple geometric considerations

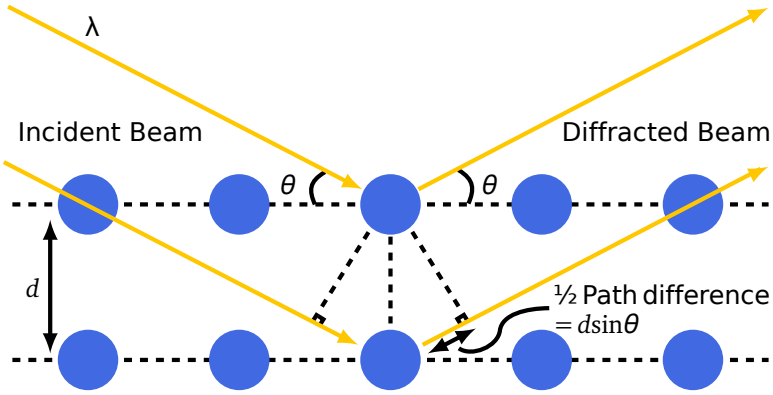

Figure 2.8: A schematic representation of X-ray diffraction for a simple two-dimensional lattice. The path difference between the incident and diffracted beams, $2d \sin\theta$, must be an integer number of wavelengths, this gives Bragg's law.

(Figure 2.8) to be used to derive Bragg's law for diffraction from a crystal lattice:

$$n\lambda = 2d_{\text{hkl}} \sin\theta \tag{2.5}$$

The planes from which these reflections can occur are described by Miller indicies. Each Miller plane has three values, h, k and l, which describe its orientation within the unit cell. For diffraction to occur, the Bragg condition must be satisfied, i.e. the plane must lie at the correct angle to the incident radiation.

If the structure is not perfectly ordered, for example, a vacancy defect or an atom slightly off-position, the amplitude of the Bragg peak decreases. This intensity is still present, but appears over a much broader range of angles than that from Bragg diffraction. In general, scattering that arises from any departures of the structure from a perfectly ordered lattice is known as Diffuse scattering. It is possible for a highly disordered structure to have no Bragg peaks at all in its measured diffraction pattern, however, there will be a broad distribution of diffuse scattering intensity over a wide range of angles. Conventional diffraction measurements typically only look at Bragg diffraction.

Powder X-ray diffraction

Single crystal X-ray diffraction is commonly used to determine the structure of a material. However, if a single crystal cannot be produced, or if an analysis of the bulk material is required, then powder X-ray diffraction (PXRD) must be used instead. Within a battery, it is not possible to form a single crystal. Any analysis must therefore be performed upon a polycrystalline powder sample. In a PXRD measurement, at any instant a very large number of crystallites are being simultaneously irradiated by the incident beam. This leads to many crystallographic planes, from many different crystallites, fulfilling the Bragg condition simultaneously, and as such the position of Bragg peaks in the PXRD pattern may be determined very accurately. This allows unit cell parameters and symmetry to be accurately determined by assigning the peaks to the crystallographic planes from which they originated. However, at higher angles the intensity drop-off, due to the Debye-Waller factor, combined with significant peak overlap can make peak assignment difficult. This means that solving

a structure using PXRD data alone is very difficult and time consuming. If the sample has a known structure, techniques such as Rietveld refinement may be used to refine the structure, giving an accurate description of the material in question.

2.2.2 Total Scattering and the Pair Distribution Function

As stated earlier, (dis)charge mechanisms of battery materials often include both amorphous and crystalline structures. Total scattering measurements treat all diffracted radiation equally (no special preference is applied to Bragg scattering). This allows measurements to probe the local structural information present in diffuse scattering from the sample. Diffraction from a disordered material takes a different form to that from a crystal as the constraints on $\boldsymbol{Q}$ and $\boldsymbol{r}$ no-longer apply. The intensity of scattered radiation for N scatters ($NF(\boldsymbol{Q})F^*(\boldsymbol{Q})$) becomes:

$$\begin{aligned} I(Q) &= N \sum_j f_j(Q) \exp\left(i\boldsymbol{r_j}\cdot\boldsymbol{Q}\right) \sum_k f_k(Q) \exp\left(i\boldsymbol{r_k}\cdot\boldsymbol{Q}\right) \\ &= N \sum_j \sum_k f_j(Q) f_k(Q) \exp\left(i\boldsymbol{r_{jk}}\cdot\boldsymbol{Q}\right) \end{aligned} \tag{2.6}$$

Assuming that the material is isotropic simplifies equation 2.6 by taking a spherical average of the exponential term. This results in the Debye scattering equation:

$$I(Q) = \sum_{j,k=1}^{N} f_j(Q) f_k(Q) \frac{\sin\left(Qr_{jk}\right)}{Qr_{jk}} \tag{2.7}$$

where r_{jk} is the distance between atoms j and k. $I(Q)$ in equation 2.7 relates to the coherently scattered intensity. Experimentally measured intensities additionally contain several components which must first be subtracted to obtain solely the coherent intensity: $I_{\text{exp}}(Q) = I_{\text{coh}}(Q) + I_{\text{incoh}}(Q) + I_{\text{MS}}(Q) + I_{\text{bkg}}(Q)$, where $I_{\text{coh}}(Q)$ is the coherent scattered intensity, $I_{\text{incoh}}(Q)$ is the incoherent scattered intensity, $I_{\text{MS}}(Q)$ is the intensity that arrises due to multiple scattering and $I_{\text{bkg}}(Q)$ is the background intensity. This function can be normalised per scatterer to give the structure function, $S(Q)$:

$$S(Q) = \frac{1}{N\left\langle f(Q)\right\rangle^2}\left(I_{\text{coh}}(Q) + \left\langle f(Q)\right\rangle^2 - \left\langle f^2(Q)\right\rangle\right) \tag{2.8}$$

where the angle brackets represent an average over atom types. The pair distribution function (PDF), G(r), is then given by the following Fourier transformation:

$$G(r) = \frac{2}{\pi}\int_0^\infty Q\left(S(Q)-1\right)\sin Qr\, dQ \tag{2.9}$$

In practice, the maximum value of momentum transfer that can be achieved, Q_{max}, is finite. This results in the truncation of the above Fourier series, which results in ripples at low-r in the resultant PDF. If necessary, these can be minimised (sacrificing some spatial resolution)

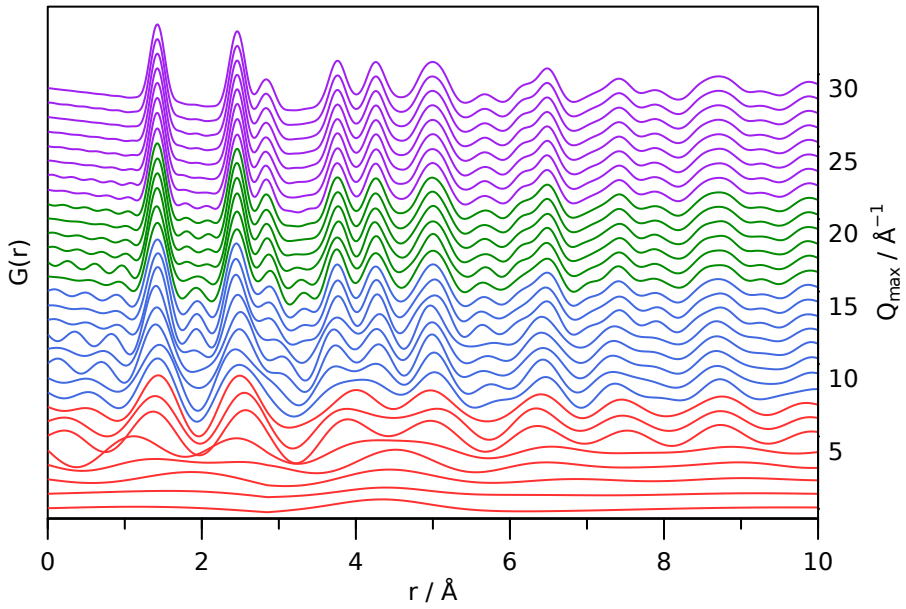

Figure 2.9: Simulated PDFs for a hard carbon in the range r=0–10 Å with different Q_{max} values. Red lines represent Q_{max} values that are within the energy range of Cu X-ray tubes, blue lines can be measured with a Mo X-ray tube, and green lines can be measured with a Ag X-ray tube. Q_{max} values greater than this can only be achieved at a synchrotron.

through the use of the Lorch modification function by first multiplying $Q(S(Q)-1)$ by:

$$\frac{\sin\left(\pi \frac{Q}{Q_{max}}\right)}{\pi \frac{Q}{Q_{max}}} \tag{2.10}$$

Perhaps more importantly, the value of Q_{max} also affects the achievable real-space resolution of the measurement, given by $\Delta r \approx \pi/Q_{max}$.[54] PDFs with sufficient resolution to allow detailed modelling are typically measured with a Q_{max} of approximately 20 $Å^{-1}$ or greater, the effect of different Q_{max} values on a simulated PDF for a hard carbon is shown in Figure 2.9. Lab sources typically use either copper K_α or molybdenum K_α radiation, which do not provide sufficiently high Q_{max} values (approximately 8 $Å^{-1}$ and 18 $Å^{-1}$, respectively). A large enough Q_{max} is achievable using a silver K_α X-ray tube ($Q_{max} \approx 22 Å^{-1}$), however, the low flux of this source means measurement times are prohibitively long for many experiments. For this reason, PDF measurements are usually carried out at a synchrotron.

A schematic showing the extraction of a PDF for a hard carbon sample from the measured data, providing examples of the functions $I(Q)$, $S(Q)$, and $G(r)$, is shown in Figure 2.10.

Interpretation

The PDF is a function which gives the probability of finding a pair of atoms with a given separation in the material. The PDF is a weighted histogram of atomic separations: where an atom pair is likely we find a peak, and where the probability of finding a pair of atoms with the given separation is low, the function returns to the baseline. This means that even if there is no long-range ordering within the structure, any local structure that exists may still

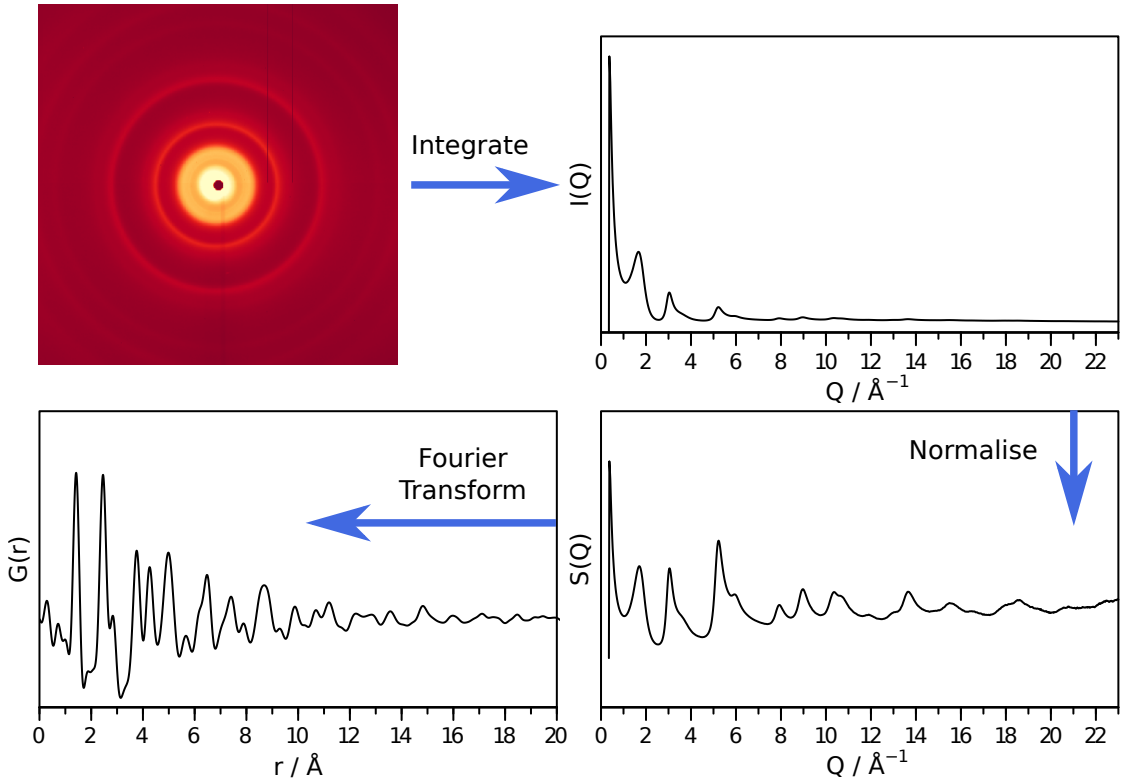

Figure 2.10: A schematic showing the major processes involved in extracting a PDF for a hard carbon.

be observed. This is in contrast to conventional methods that rely on Bragg scattering, which only contains information on the average structure. Furthermore, the magnitude of random errors (noise) in the data is constant with r. This allows for modelling of the data in a manner resilient to the underlying uncertainties in the data. There are several pieces of information which may be readily extracted from the PDF in a model-independant manner:

- The centre of each peak gives the atomic separation.
- The area under each peak is related to the coordination number. However, care must be taken to account for overlapping peaks (especially at higher-r) and the chemical origin (and thus the weighting factor) must be known in order for the coordination number to be calculated accurately.
- The width of each peak is related to the local disorder around that site. For a perfectly ordered structure at a temperature of 0 K, all the peaks would be delta functions with infinite height. In practical scenarios, peaks have finite height, and both thermal and structural disorder contribute to the width of a peak along with the Q_{max} value used in the Fourier transform.
- The value at which peaks are no-longer present gives the correlation length of the sample. A highly crystalline sample will have well defined peaks in the PDF beyond 100 Å, disordered materials may have no discernable peaks after the first one or two coordination spheres (typically a few Å).

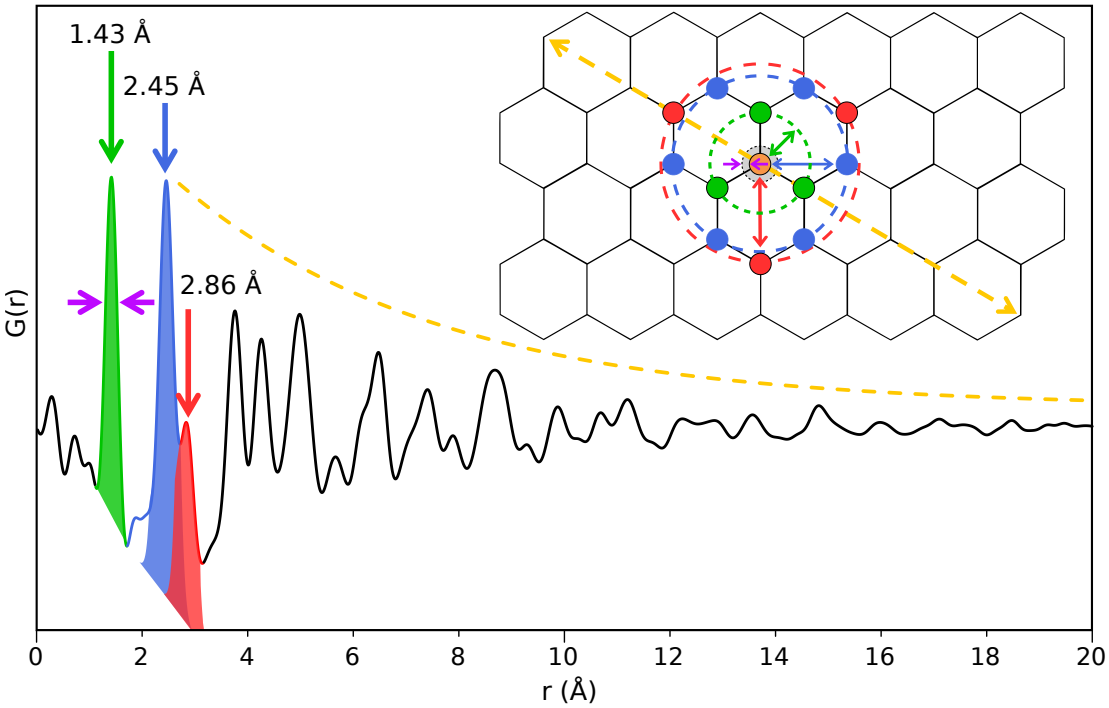

Figure 2.11: An example of the relationship between a structure and its PDF. The PDF of a hard carbon is shown with the first three peaks highlighted, and their positions indicated. Inset: A graphene fragment whose first three distances are indicated by red, green and blue arrows. The purple arrows indicate local disorder, which is, in part, responsible for the width of the peak. The yellow arrow indicates the size of the fragment which is the major contributor to the decay of the PDF.

This is summarised in Figure 2.11 using the measured PDF of a hard carbon as an example, with the features in the PDF linked to their structural origin from a graphene layer. The first peak is found at 1.43 Å, this is the shortest distance between two atoms within a graphene layer. Any peaks in experimental PDF below this value result from Fourier truncation errors and are a good indication of the quality of the data — smaller ripples typically indicate higher quality data. As carbon-carbon bond lengths are well defined, the peaks in the PDF are reasonably sharp, however, the intensity of the peaks decays rapidly with increasing r. This is due to the limited size of the graphene domains within the sample, which limits the correlation length of the material.

Modelling

Whilst the model-independant information described above can be useful in the qualitative interpretation of structural changes, a full description of the PDF requires more detailed modelling. *Ab initio* structure determination is not usually possible from PDF data, although it has been demonstrated for some model cases such as C_{60}.[55] Instead, it is most common to find a reasonable initial model either from existing crystal structures, or theoretical calculations. This model is then refined against the experimental data (in either or both of real-space and reciprocal-space). In a real-space refinement, a calculated PDF from a structural model is compared to the experimentally determined PDF to give information about the local structure of the material. PDFs can be calculated by one of two methods, the first takes the sum of all

atomic correlations, weighted by their scattering power, and subtracts a baseline based upon the atomic number density:

$$G_{\text{calc}}(r) = 4\pi r\left[\rho(r) - \rho_0\right] \tag{2.11}$$

$$= \frac{R(r)}{r} - 4\pi r\rho_0$$

$$= \frac{1}{r}\sum_i\sum_j\left[\frac{f_i f_j}{\langle f\rangle^2}\delta\left(r - r_{ij}\right)\right] - 4\pi r\rho_0 \tag{2.12}$$

where $\rho(r)$ is the real-space pair density, $R(r)$ is the radial distribution function (RDF), ρ_0 is the number density of the material, f_i is the atomic scattering factor of the ith atom, and r_{ij} is the distance between atoms i and j. As all pair correlations in this sum are modelled as infinitely thin delta functions, equation 2.12 is only valid if the model is sufficiently large to statistically account for thermal vibrations of the atoms as static distortions within the structure. For this reason, it is more common to replace the delta function with a modified gaussian for smaller strucutures, based upon the thermal displacement parameters for the material:

$$T_{ij}(r) = \frac{1}{\sqrt{2\pi\sigma_{ij}}}\exp\left[-\frac{(r - r_{ij})^2}{2\sigma_{ij}^2}\right]\left[1 + \left(\frac{r - r_{ij}}{r_{ij}}\right)\right] \tag{2.13}$$

where σ_{ij} comes from the anisotropic thermal displacement parameters of the atoms i and j. In addition, the limited Q-resolution of the instrument results in a damping of the measured PDF, this is included in the calculation via the damping function $\exp\left(-\frac{(Q_{\text{damp}}r)^2}{2}\right)$. Where Q_{damp} is an experimentally determined parameter representing the degree of damping. It is typically refined against a known standard. Finally, the measured PDF has a finite value for Q_{max}, which results in ripples in the observed PDF and broadening of the observed peaks. These are commonly modelled using one of two methods, either by the convolution of G_{calc} with the Fourier transform of a step function, $\frac{\sin(Q_{\text{max}}r)}{r}$, or by a combination of a Fourier transform and an inverse Fourier transform with appropriate limits.

However, equation 2.12 is only valid for large structures (or crystals with periodic boundary conditions if using the modification provided by equation 2.13). Structures with lower dimensionality (for example nanosystems) have PDFs with a different form. This is because equations 2.9 and 2.11 are not equivalent. For the given integration limits (0 and ∞), equation 2.9 actually gives the following result:

$$G(r) = \frac{2}{\pi}\int_0^\infty Q\left(S(Q) - 1\right)\sin Qr\, dQ$$

$$= \frac{R(r)}{r} = 4\pi r\rho(r) \tag{2.14}$$

In practical measurements, however, both of the integration limits are finite. The effects of a finite upper limit (Q_{max}) are well understood and described earlier. A finite value of the lower limit (Q_{min}) results in the removal of small angle scattering (SAXS) data from the measured

PDF, i.e:

$$G(r) = \frac{2}{\pi}\int_{Q_{\min}}^{\infty} Q\,(S(Q)-1)\sin Qr\,dQ$$
$$= 4\pi r\rho(r) - \frac{2}{\pi}\int_{0}^{Q_{\min}} Q\,(S(Q)-1)\sin Qr\,dQ \tag{2.15}$$

The second term in equation 2.15 was evaluated for a general scatterer of uniform density by Farrow and Billinge:[56]

$$\frac{2}{\pi}\int_{0}^{Q_{\min}} Q\,(S(Q)-1)\sin Qr\,dQ = 4\pi\rho_0 r\gamma_0(r) \tag{2.16}$$

where $\gamma_0(r)$ is a characteristic function of the shape of the nanoparticle. Thus the correct form of equation 2.11 for an experimentally obtained PDF is:

$$G_{\text{calc}}(r) = 4\pi r\rho(r) - 4\pi\rho_0 r\gamma_0(r) \tag{2.17}$$

For bulk structures, i.e. those whose correlation length is much greater than the r-range over which the PDF is calculated, $\gamma_0(r) \approx 1$ for all values of r, equation 2.17 simplifies to equation 2.11, and the previously described approach for calculating a PDF is valid. However, if the r-range is of similar magnitude to (or smaller than) the correlation length, this damping of the atomic correlations must be accounted for. Characteristic functions for a variety of simple geometries can be determined analytically,[57] and are commonly applied for the case of spherical particles. This means that a PDF can be calculated for a number of common nanoparticle morphologies simply by multiplying the PDF calculated for the bulk material (equation 2.12) by the characteristic function, i.e. $G_{\text{calc}}(r) = \gamma(r)G_{\text{bulk}}(r)$. However, when the particle morphology is influenced by the underlying structure, this approach typically fails. The second approach to calculating a PDF does not require such a modification function to account for particle morphology, and can therefore be used in a greater number of situations, but it is computationally expensive for larger structures (e.g. crystals). Firstly, the scattered intensity is calculated using the Debye equation (equation 2.7), which is then normalised and Fourier transformed to give the PDF. In this case the experimental values of $Q_{\min}$ and $Q_{\max}$ can be used directly in the Fourier transform. Both approaches to PDF calculation are used in this work.

Refinement

Calculated and experimental PDFs can be compared, and the underlying structural model adjusted in order to minimise the difference between them. There are a number of methods by which this may be performed. The most common method is analogous to Rietveld refinement for Bragg diffraction data (as such it is commonly referred to as "real-space Rietveld"). This is a least-squares method that fits the PDF in real-space. Parameters that depend on the experimental setup, such as Q_{damp}, may be refined along with those that derive from the structure, such as lattice parameters, atomic positions, and anisotropic thermal displacement parameters. The goodness of fit for such a refinement, R_w is given by the following expression:

$$R_w = \sqrt{\frac{\sum_{i=1}^{N} w(r_i)\left[G_{\text{exp}}(r_i) - G_{\text{calc}}(r_i)\right]^2}{\sum_{i=1}^{N} w(r_i) G_{\text{exp}}^2(r_i)}} \tag{2.18}$$

where $w(r_i)$ is the weighting factor for data point r_i, which depends upon the statistical quality of the data point. Whilst there are obvious analogies between real- and reciprocal-space Rietveld methods, the sensitivity to local ordering in real-space results in R_w values often being greater than 15% even for well-ordered materials. Conversely, R values for reciprocal-space refinement should usually be around 5% or less for a good fit.

A second, commonly used method for fitting PDF data is reverse Monte Carlo (RMC) refinement. This is a so called "big box" method often employing many thousands of atoms within a single model. Typically both real- and reciprocal-space data are fitted simultaneously, with the differences to both functions minimised. For each iteration of the algorithm, a parameter is adjusted (for example an atomic position) and the diffraction patterens are calculated. If an improvement to the fit is found, the move is accepted. If the move results in a worsened fit, the move may still be accepted subject to an underlying probability distribution. This makes the method more resilient towards energy landscapes containing local minima, given infinite time, the global minimum should be located.

2.3 Nuclear Magnetic Resonance

NMR is a technique that probes the interaction between nuclear spins and an external magnetic field. All nuclei posses intrinsic spin angular momentum, $\boldsymbol{I}$, whose magnitude — the spin quantum number, I — can be zero or any positive integer or half-integer value. Any nuclei with a spin not equal to zero can be studied by NMR. The projection of this angular momentum onto the z-axis is given by $I_z = m_l\hbar$, where m_l is the magnetic quantum number, whose values range from $-I$ to $+I$, giving a total of $2I + 1$ states. In the absence of an external magnetic field, all these states are degenerate in energy, resulting in randomly orientated spins. Applying a field, B_0, lifts this degeneracy, resulting in preferential alignment of the spins relative to B_0. This is known as the Zeeman interaction. Under standard conditions, there will be a small excess of spins in the lower energy level, giving rise to a net magnetisation vector orientated in the direction of the B_0 field.

A formal treatment of spin requires quantum mechanical operators, however, to a first approximation, it is possible to understand the processes in a simpler, classical manner. The "vector model" considers only the bulk magnetisation vector described above. If rotated away from the direction of the applied field, the net magnetisation vector would precess about the field at a characteristic frequency given by $\omega_0 = -\gamma B_0$, where γ is the gyromagnetic ratio. It is this precession which is detected in an NMR measurement, where the frequency is given the name the Larmor frequency. By placing a coil in a direction orthogonal to the B_0 field, it is possible to detect this precession to give a signal known as a free-induction decay (FID), which can be Fourier transformed to give the NMR spectrum. Figure 2.12 presents a summary of these processes. Different local magnetic environments result in slight per-

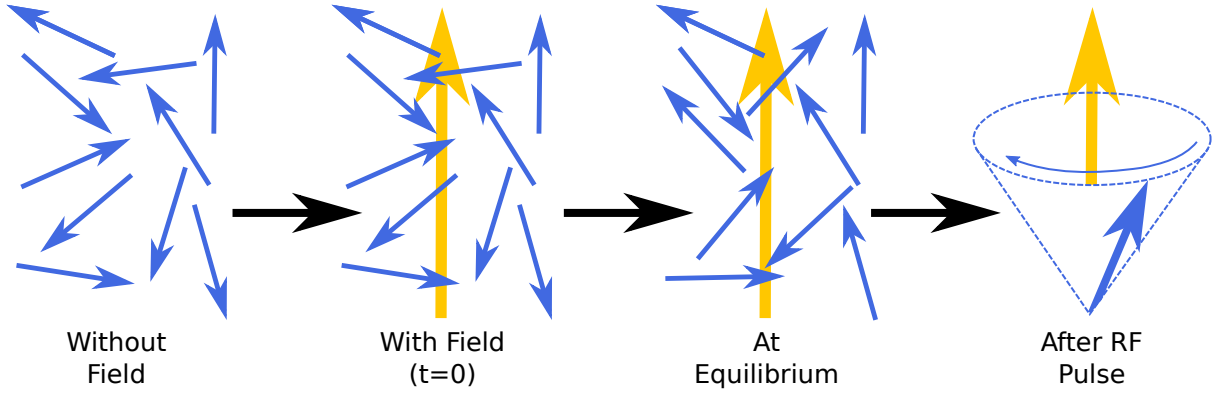

Figure 2.12: Schematic showing the interaction of nuclear spins with an applied magnetic field and the bulk magnetisation vector following the application of an RF frequency pulse.

turbations to the Larmor frequency, which is now given by $\omega = -\gamma B_{\text{local}}$. Each peak in the frequency domain spectrum, therefore, derives from a different local magnetic environment of the probed nucleus. This allows local structural information to be obtained. As almost all stable elements in the periodic table possess NMR active isotopes, whose Larmor frequencies all differ, this structural information can be obtained on an element specific basis.

In order to rotate the magnetisation vector away from the direction of the applied field, one could conceivably rotate the external field. However, practical issues caused by the superconducting magnets required make this impossible. Instead, we introduce a second, oscillating, field, B_1, much smaller than B_0 and orientated in an orthogonal direction. This has the effect of reducing the effective field felt by the nuclear spins, which is now given by the expression $B_{\text{eff}} = \sqrt{B_1^2 + \frac{\omega_0 - \omega_1}{\gamma}^2}$, where ω_1 is the frequency of the B_1 field. It is this field about which the magnetisation precesses, with frequency $\omega_{\text{eff}} = \gamma B_{\text{eff}}$. If the frequency of the B_1 field, ω_1, is the same as, or close to, the Larmor frequency, ω_0, then the effective field felt by the spins is simply the B_1 field (or very close to it). This is the resonance condition. Precession about this field causes the magnetisation vector to rotate away from the B_0 field. By applying this field for short periods of time, the amount of rotation can be controlled. This is the principle behind pulsed NMR: short RF pulses create an oscillating B_1 field for a period of time given by the pulse length, which has the effect of rotating the magnetisation away from B_0. In practice, these pulses can be supplied by the same coil used to detect the FID.

The simplest pulse sequence consists of only a single pulse. It is applied at a power and for a duration that causes the magnetisation vector to rotate by 90°, giving the largest amount of signal. Following this, the FID is acquired. In practice, there is a short delay (DE in Figure 2.13a) prior to acquisition to allow for noise (caused by acoustic ringing within the probe, pulse breakthrough, and imperfect pulses) to reduce, and to account for finite electronic switching times. This has two important consequences: if acquisition were to begin immediately following a perfect pulse, the FID would consist solely of cosine functions, which could be Fourier transformed to give an in-phase spectrum. Owing to the dead-time required, some phase information is lost and a manual phase correction is required post-acquisition. Secondly, a delay that is sufficiently long to allow for all acoustic ringing effects to decay

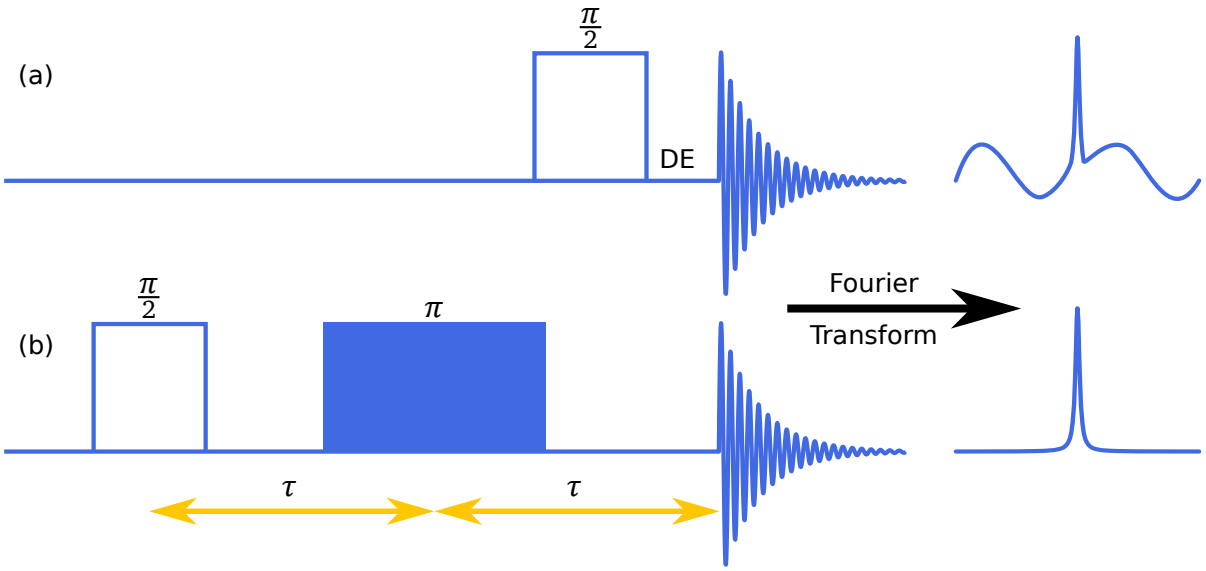

Figure 2.13: (a) A one-pulse (zg) pulse sequence and (b) a Hahn-echo pulse sequence. The filled rectangle represents a π pulse, whilst the empty rectangles represent $\frac{\pi}{2}$ pulses. τ is the delay between pulses, and DE is the dead time prior to acquisition.

would result in much of the FID not being acquired. In practice, this means that some of these effects persist into the Fourier transformed spectrum, manifesting as a non-linear baseline.

The problems with a one-pulse sequence can be mitigated, to some extent, through the use of a Hahn-echo pulse sequence (Figure 2.13b). In this situation, a 180° pulse is used following the 90° pulse, after a delay τ. This causes the magnetisation to be refocussed after a total time of 2τ. This increases the delay between the end of the pulse and the start of acquisition, allowing both the whole FID to be acquired and reduced a acoustic resonant signal — thereby improving the baseline. However, this increased time also results in a greater amount of relaxation of the spins and therefore a signal of lower intensity.

Solid-State Nuclear Magnetic Resonance

The electrons within a material shield the nuclear spins from the B_0 field. This can result in a variety of local magnetic fields within a material, and thus a variety of different Larmor frequencies as discussed earlier. These different frequencies give rise to distinct chemical shifts in the resultant NMR spectrum. However, as the electrons are not spherically distributed, there is also an orientation dependance on the chemical shift. This is known as chemical shift anisotropy (CSA). In a liquid, the rapid tumbling of molecules averages out this anisotropy so that sharp peaks are observed in the spectrum. This is not the case in a solid. Instead, each individual crystallite has a chemical shift dependant upon its orientation, and the observed lineshape is the sum of these components. An example of a CSA lineshape is shown in Figure 2.14a. This broadening of the observed signal can result in overlapping signals, and a reduced signal-to-noise ratio, which can make solid-state NMR (SSNMR) spectra difficult to interpret.

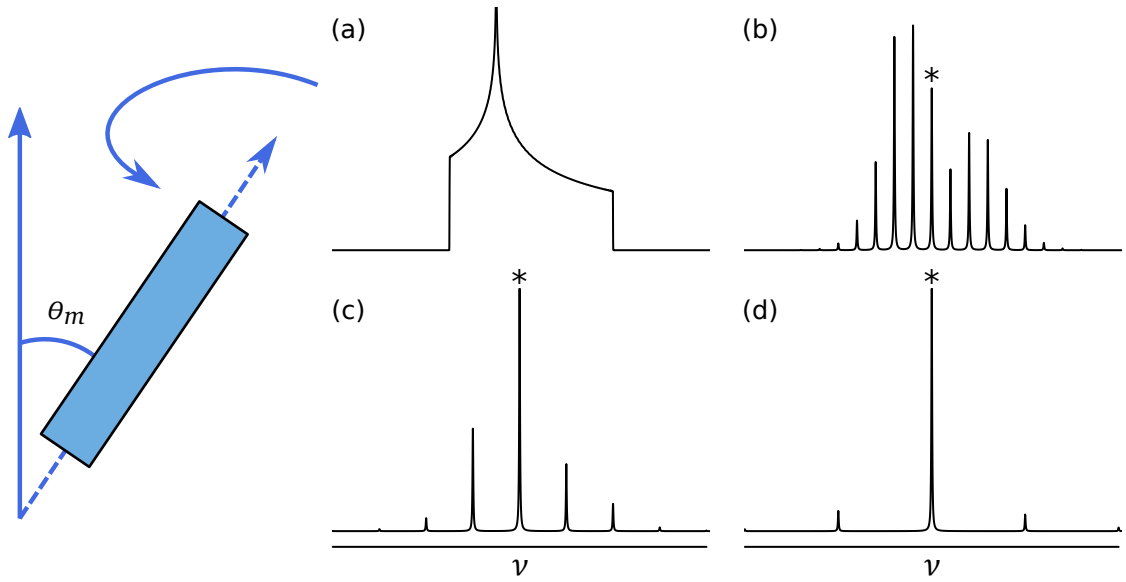

Figure 2.14: Schematic representation of spinning at the magic angle, θ_m, with simulated spectra for a spin $\frac{1}{2}$ nucleus (a) static and (b–d) with increasing spinning speed. $*$ indicates the isotropic frequency.

CSA is not the only cause of broadening in SSNMR spectra: dipolar coupling can also result in significant broadening. Furthermore, for nuclei with $I > \frac{1}{2}$, the non-spherical distribution of electrons results in another (orientationally dependant) broadening. This quadrupolar interaction is the second strongest interaction behind Zeeman splitting.

A full quantum-mechanical treatment of these interactions reveals a first order dependance on $3\cos^2\theta - 1$, where θ is the angle between the sample and the B_0 field. This is at a minimum when $\theta_m = 54.7°$, where θ_m is known as the magic angle. Spinning the sample at this angle (magic angle spinning (MAS)) doesn't completely remove all broadening effects, owing to second-order terms, but can have a significant effect on the resolution of the acquired spectrum (Figure 2.14). As the orientation of the sample returns to its initial value after one complete rotation (a rotational echo), the FID for a spinning sample contains additional terms with periodicity equal to integer multiples of the spinning rate. This results in a spinning sideband manifold in the Fourier transformed spectrum. These sidebands contain information on the CSA, but may overlap with other peaks, complicating the interpretation.

For metals (i.e. materials containing a conduction band), there is a further important NMR interaction to be considered. The electrons in the conduction band generate an additional magnetic field around the nuclei. This enhances the applied field, resulting in significantly greater chemical shifts. For example, the ^{23}Na chemical shift of sodium chloride is close to 0 ppm, whereas that of sodium metal is closer to 1100 ppm. The difference between the chemical shift of a metallic material, and that of the same atoms in a nonmetallic environment is known as the Knight shift. This interaction is particularly important for electrochemically relevant materials, where the conductivity of a material can vary as a function of its stoichometry.

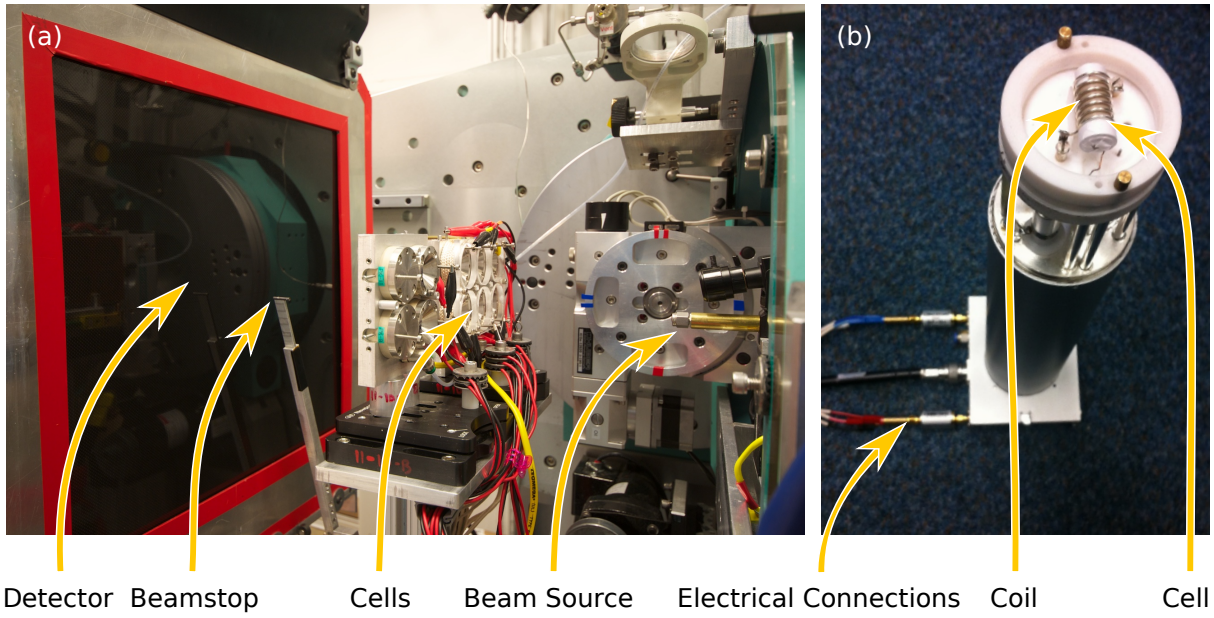

Figure 2.15: Photographs showing the setup for *operando* (a) PDF experiments and (b) NMR experiments.

2.4 *Operando* Measurements

In order to characterise the mechanisms by which materials cycle within a battery, it is necessary to examine the materials following sodium (or lithium) insertion. This is commonly performed using post-mortem analysis techniques, whereby the battery is disassembled and the electrodes recovered. However, following sodium (or lithium) insertion, electrochemical materials often become highly air-sensitive, leading to a high probability of sample contamination or structural change during such *ex situ* measurements. In addition, many systems proceed via metastable phases, which relax upon removing the current, causing immediate changes to the structure even without any sample exposure.

In order to avoid these issues, this work has focused on the use of *operando* (commonly referred to as *in situ*) techniques. By making alterations to the electrochemical cell in which the material is cycled, it is possible to (for example) collect X-ray diffraction (XRD) or NMR data on the material whilst it is still being cycled. This can introduce additional challenges as the cell must be compromised in some manner to allow for external characterisation, which can impact upon the electrochemical performance. It can also have consequences for the achievable quality of the spectroscopic data. For example, it is not currently possible to spin a battery in a magnetic field — preventing MAS. However, it allows for a much more complete understanding of the changes that a material undergoes whilst cycling. Examples of the setup for *operando* PDF and SSNMR measurements are shown in Figure 2.15, the cells used are shown in Figure 2.4.

3 Preliminary Investigations into Sodium Storage Mechanisms in Hard Carbon Anodes

Preface

The PDF work described in this chapter was performed together with Dr Phoebe Allan. The work described in this chapter may be found in the following publication, whose text and figures are adapted here:

Stratford, J. M.; Allan, P. K.; Pecher, O.; Chater, P. A.; Grey, C. P. Mechanistic insights into sodium storage in hard carbon anodes using local structure probes. *Chemical Communications* **2016**, *52*, 12430–12433

3.1 Introduction

NIBs are an attractive option for low-cost and environmentally benign energy-storage technologies. Whilst graphite shows almost no ability to store sodium electrochemically, non-graphitizable hard carbons demonstrate good reversible capacity and are among the cheapest proposed anode materials to date.[23,24,34] Early studies reported two electrochemical processes: a sloping region followed by a process close to 0 V versus sodium. By analogy with the lithium system, it was suggested that sodium insertion proceeded via a two-stage mechanism associated with these two electrochemical signals: intercalation of sodium between nearly parallel layers, followed by the formation of metallic species within the pores of the material at low voltages,[58] experimental support for this mechanism coming from SAXS data.[59] These studies indicated that pores are filled during the low-voltage process, the same authors later attributing a change in intensity of the graphitic (002) reflection to sodium intercalation within the structure.[24]

A decade later, other reports began to appear proposing alternative mechanisms. For example, Gotoh *et al.* did not observe metallic sodium environments in *ex situ* ^{23}Na SSNMR studies.[60] Recent DFT calculations generated similar electrochemical profiles to those seen

experimentally through consideration of intercalation alone: at higher voltages, Na intercalates near mono- and di-vacancy defects, essentially complete charge transfer to the carbon sheets takes place (charge primarily being localised near the defects) resulting in ionic Na^+ ions. This increased iconicity was proposed to help to overcome the van der Waals attractions holding the graphene layers together.[28] The low voltage region is then ascribed to further intercalation in graphitic interlayer spaces near the defects, in combination with intercalation between layers with larger interlayer spaces. The importance of defects was tested experimentally in 2015; a range of hard carbons at different annealing temperatures were prepared, and the number of structural defects was quantified via the ratio of the areas of the Raman G and D band peaks.[61] A correlation between the D:G band ratio and the observed capacity during the sloping region was then observed, intercalation being proposed to occur at lower voltages. The same authors presented PDF analysis of neutron scattering data for their carbons, analysing the size of the graphene domains in these materials. Following this, it was shown that the systematic carbonisation of carbon nanofibers at temperatures ranging from 650–2800 °C was able to tailor the graphitisation degree of the resulting carbons.[62] They classified the carbons into three different stages, stage I showing only the first (sloping) electrochemical process, stage II showing both processes and stage III which only exhibits the second (plateau) process; stage III being formed at the highest temperatures and stage I the lowest. They conclude that the sodium storage mechanism consists of three processes: (i) storage at defect sites created by heteroatoms (ii) adsorption on disordered isolated graphene sheets between 1–0.1 V, and (iii) mesopore filling below 0.1 V.

More recently, gas adsorption measurements were made employing several different gasses (N_2, Kr and CO_2) to carefully asses the porosity of cellulose derived hard carbons prepared at different temperatures.[63] They found that the capacity resulting from the sloping process decreased as the specific area of ultramicropores reduced, the plateau capacity having the opposite behaviour. They found that carbons prepared at temperatures exceeding 1400 °C had no porosity, which the authors claim disqualifies pore-filling as a possible mechanism, leaving only intercalation between pseudo-graphitic layers. It should be noted, however, that they did not account for any non-accessible internal porosity in their measurements. They also found a decrease in the oxygen heteroatom concentration with increasing temperature, which correlates with a decrease in the slope capacity. In 2018, a series of carbon nanospheres with differing graphitisation degrees were prepared.[64] The authors used GITT based diffusion measurements, along with diffraction and Raman measurements to conclude a three-stage storage mechanism: chemi- / physisorption, followed by intercalation, and finally pore-filling. In this chapter, we explore the different proposed mechanisms for sodium insertion, studying a commercial hard carbon using X-ray total scattering PDF analysis and ^{23}Na SSNMR. We see distinct electronic and local structures for the Na inserted in the higher and lower voltage processes.

3.2 Experimental

Except were otherwise stated, all experiments were performed under ambient conditions.

3.2.1 Electrode Preparation

Carbotron P(J) (Kureha Corporation) was mixed with 10% polyvinylidene fluoride-co-hexafluoropropylene (Kynar), to which one drop of dibutyl phthalate (Sigma-Aldrich) was added for every 10 mg of binder. Acetone (Sigma-Aldrich, anhydrous) was added, and the resultant slurry spread onto a glass substrate using a 300 µm doctor blade. After drying in air, the film was washed three times with diethyl ether (Sigma-Aldrich) and dried at 100 °C *in vacuo* prior to use.

3.2.2 PDF Analysis

Cells for PDF analysis were cycled at a rate of C/20 (based on the mass of carbon, with 1C corresponding to achieving a capacity of 300 mA h g^{-1} in one hour) to the point of interest on the electrochemical curve. The electrodes were recovered inside an argon atmosphere glovebox, washed with dimethylcarbonate (Sigma Aldrich, anhydrous, > 99%) and immediately dried *in vacuo*. The electrode films were then individually ground and sealed into thin walled quartz capillary tubes (Hampton Research, OD=2 mm).

PDF data were collected at beamline I15-1 at Diamond Light Source using a wavelength of 0.163 000 Å and a Perkin-Elmer flat panel detector. A CeO_2 standard was used to calibrate the sample geometry and the sample-to-detector distance. The data were converted to a function of intensity vs. Q using Data Analysis WorkbeNch (DAWN).[65] Standard corrections (background, Compton scattering, detector effects) were applied, and the data Fourier transformed (Qmax = 20.5 Å) to obtain G(r) using the software PDFGetX2.[66] Structural models were refined against PDF data using PDFGUI.[67] Difference PDFs were calculated by subtracting the PDF for the pristine electrode from the PDFs of the electrodes at various stages of charge. Difference PDFs were r-averaged over termination ripples.

3.2.3 Solid-State NMR Spectroscopy

Operando SSNMR measurements were performed using an in house designed electrochemical cell based upon a cylindrical capsule (Figure 2.4d on page 10). Cells were prepared in an argon atmosphere glove box (O_2, H_2O < 0.1 ppm) using metallic sodium (Sigma Aldrich, 99.9%) as an anode. The electrolyte was 1 M $NaPF_6$ (Alfa Aesar, 99%) in propylene carbonate (Sigma Aldrich, anhydrous), and the separator was borosilicate glass fibre (Whatman, GF/A). Electrochemical measurements were conducted on a Bio-Logic VSP battery cycler. Cells were cycled at a rate of C/20 (based on the mass of carbon, with 1C corresponding to achieving a capacity of 300 mA h g^{-1} in one hour) and held at 5 mV until the applied current dropped to C/100.

A Bruker Avance 300 MHz spectrometer with a ^{23}Na Larmor frequency of 79.39 MHz was fitted with an in house designed static probe with automatic tuning and matching capabilities

(along with connections for an external battery cycler) and used for the measurements reported.[68] The electrochemical cell was aligned such that the electrodes were parallel to the applied field.

In order to maximise the signal-to-noise ratio for a time-restricted measurement, a one-pulse sequence was used. A 90° pulse corresponded to 3.5 µs at 200 W using an 11 mm diameter silver coil. 30000 transients were collected for each spectrum, using a recycle delay of 0.05 s (31 minutes per spectrum). The resonance circuit was recalibrated immediately prior to each acquisition by minimising the standing wave ratio of the forward and reflected power for a low power (0.01 W) continuous wave pulse.[68] The ^{23}Na signals were referenced using a 1 M solution of NaCl at a shift of 0 ppm.[69] Spectra were Fourier transformed and individually phased using Bruker Topspin 3.2. Backgrounds were subtracted using fityk.[70]

Ex situ ^{23}Na MAS NMR measurements were performed using a Bruker Avance III 200 MHz spectrometer with a ^{23}Na Larmor frequency of 52.92 MHz and a Bruker Avance III 500 MHz spectrometer with a ^{23}Na Larmor frequency of 132.29 MHz. 1.3 mm zirconia rotors were spun at 60 kHz using a Bruker double resonance probehead. A MAS speed synchronised Hahn-echo pulse sequence with 90–180° pulses corresponding to 2–4 µs at 25 W was applied for the lower field measurements, at higher field, a one pulse sequence was applied; a recycle delay of 0.05 s was used. Spectra were referenced using NaCl powder at 7.21 ppm.[71]

Samples for *ex situ* MAS NMR investigations were prepared electrochemically; cells were cycled at a rate of C/20 (based on the mass of carbon, with 1C corresponding to achieving a capacity of 300 mA h g^{-1} in one hour) to the point of interest on the electrochemical curve. The electrodes were recovered inside an argon atmosphere glovebox (O_2, H_2O < 0.1 ppm), washed with dimethylcarbonate (Sigma Aldrich, anhydrous, >99%) and immediately dried *in vacuo*. The respective electrode films were then individually ground and packed into rotors immediately.

3.3 Results

3.3.1 Pair Distribution Function Measurements

The PDF for the pristine hard carbon, derived from the Fourier transform of the corrected, normalised total scattering data, is shown in Figure 3.1a. The position of peaks in the PDF, which correspond to atom-atom distances within the structure, are well-matched to those in a graphene fragment. The position and intensity of peaks at interatomic distances, r, greater than 5 Å deviate strongly from those observed in the PDF for graphite Figure 3.3, implying non-parallel stacking of graphene fragments within the hard carbon. Peaks are observed until around 25 Å. The loss of the correlations beyond this distance arises from disorder within the structure; a combination of sheet curvature (caused in part by defects within the graphene sheets) or termination of the carbon fragments is likely to be responsible. Curvature may result from small numbers of non-hexagonal carbon rings; however, our PDF

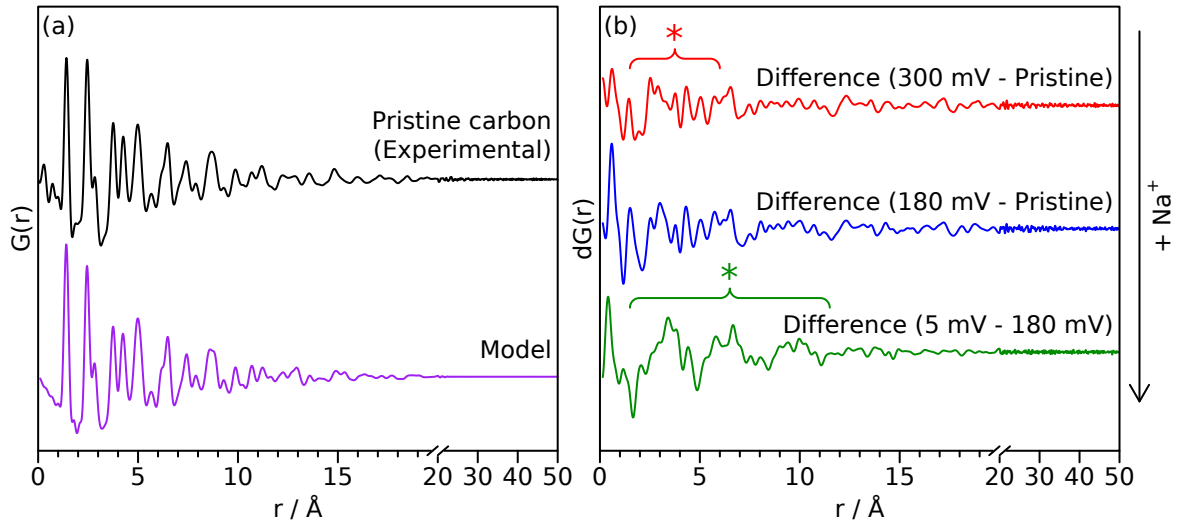

Figure 3.1: (a) Experimental PDF data for pristine hard carbon and a PDF simulated using a turbostratically disordered graphite model (offset below); (b) Difference PDFs of hard carbon anodes at various states of charge. The red line (top) corresponds to a sample discharged to 300 mV, the blue (middle) to 180 mV and the green (bottom) to 5 mV. Difference PDFs were r-averaged over termination ripples. The red $*$ highlights the range over which additional interactions are formed in the high-voltage process, the green $*$ highlights the additional interactions observed during the low-voltage process. Weaker peaks are a result of minor changes to the carbon structure and termination ripples. Full experimental data may be found in Figure 3.2, a breakdown of the intermediate stages in generating the model, plus a comparison with graphite is presented in Figure 3.3.

data does not show major correlations at the expected distances for 5- or 7-membered rings (2.34 and 3.2 Å, respectively), indicating that any such features can only be present in small concentrations.[72]

The experimental PDF can be simulated using a starting model of graphite, with large displacement parameters in the c-lattice direction; this is used to model disorder between fragments (i.e., layer stacking) (Model in Figure 3.1a). An extended unit cell parameter in the c-direction accounts for the lower density of the hard carbon compared to graphite (1.52 g cm^{-3} compared to typical values of 2.26 g cm^{-3}).[73,74] This model can account for significant turbostratic disorder in the material, as has been suggested by PDF studies of similar materials.[61,72,75]

Real-space least-squares refinements of this graphite-derived model against experimental PDF data are unable to fit the entire r-range of the dataset using a single value for the a-lattice parameter. Instead, we discover a systematic decrease of the a-parameter in refinements against data in longer interatomic distance ranges (Table 3.1 and Figure 3.4). The PDF simulated for a planar graphene sheet using the a-parameter obtained from refinement of the model against low-r peaks (1–5 Å) consistently overestimates the position of peaks at high-r ($>$ 10 Å). This means that atoms in the graphene sheet are found to be systematically closer together with increasing r than would be predicted by a planar arrangement, implying a significant degree of curvature of the fragments. This result implies a more complex arrangement of fragments in space than the commonly used "house-of-cards" model.[58,76] Notably, we would expect fewer parallel layers and a wider range of interlayer spaces.

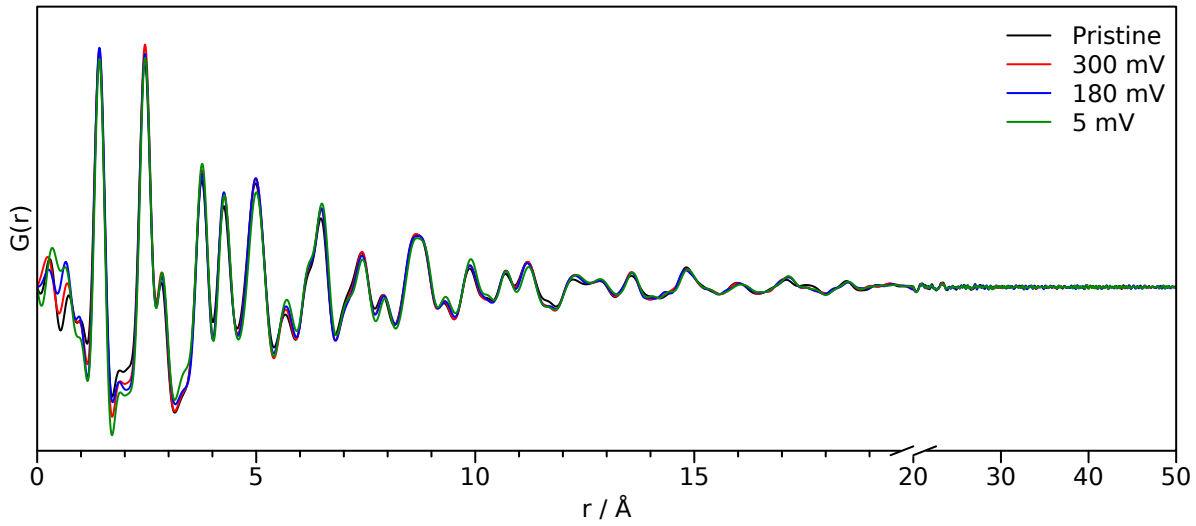

Figure 3.2: PDF data for electrodes at various stages of discharge. The black line corresponds to the pristine film, the red line to a sample discharged to 300 mV, the blue to 180 mV and the green to 5 mV. Data were Fourier transformed using a Q_{max} of 20.5 Å.

3.3.2 Solid-State NMR Measurements

Operando ^{23}Na SSNMR experiments are able to probe different local atomic environments present during cycling, and additionally are not susceptible to degradation or relaxation effects that might affect the *ex situ* results.[77] Two peaks at −10 ppm and 1135 ppm are observed for the pristine electrochemical cell corresponding to the $NaPF_6$ electrolyte and the sodium metal counter electrode, respectively (Figure 3.5). During the initial sloping electrochemical process, down to a voltage of 0.8 V, only changes to the intensity in the region around 0 ppm are observed. This is consistent with either the formation of diamagnetic species within the bulk of the electrode or of electrolyte decomposition on the surface to form the SEI layer. At voltages lower than 0.8 V, an additional signal at approx. −40 ppm emerges and grows in intensity. Throughout the low voltage region of the electrochemistry, (i.e., below 180 mV) this peak continues to grow but now proceeds to shift to higher frequencies, finally reaching 760 ppm at the end of sodium insertion. Upon sodium removal, the reverse of these processes occurs, returning to a spectrum showing only the original two features. The behaviour is identical on subsequent cycles.

Ex situ ^{23}Na MAS SSNMR spectra were obtained in order to gain additional resolution in the diamagnetic shift region without overlap from an electrolyte signal (Figure 3.6). The spectra are consistent with the *operando* measurements; two regions of intensity are observed with peak maxima at −70 ppm and 660 ppm, which appear at similar states of charge to the *operando* measurements. It should be noted that differences in the value of the shift between static and MAS spectra are commonly observed owing to bulk magnetic susceptibility effects.[78] Additional peaks in the *ex situ* spectra are assigned to sodium present in the SEI and residual electrolyte. The observation of the shifted peaks at positive frequencies in the *ex situ* spectra is highly dependent on the time for which the cell was allowed to rest prior to recovering the electrode, with relaxation occurring over the course of several hours; this observation indicates that the material formed after sodium insertion continues to react with

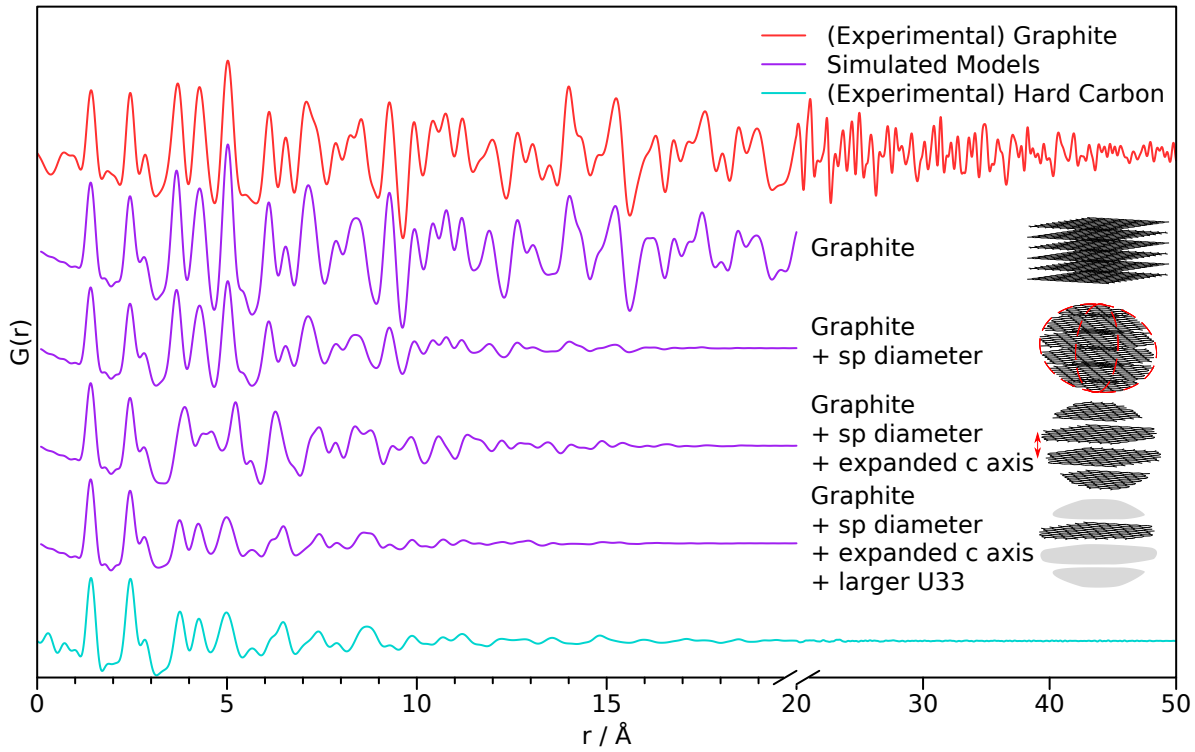

Figure 3.3: Experimental PDF data for the pristine hard carbon (blue, bottom) and graphite (red, top). The purple lines (middle) show the intermediate stages in generating the model.

electrolyte resulting in self-discharge and oxidation of the electrode. The samples, once extracted from the cell, were also found to be highly air and moisture sensitive and extreme care needed to be taken to prevent unwanted side reactions; these factors may explain why peaks in this frequency range were not observed in the previously reported ^{23}Na NMR spectra.[60]

3.4 Discussion

Additional spectra obtained at two different magnetic fields (Figure 3.7) indicate that the shift of the signal with a peak maximum at −70 ppm is dominated by second order quadrupolar coupling. Fits of these spectra (Figure 3.7 and Table 3.2) reveal an isotropic shift of approximately −4 ppm, this small negative shift being at least in part ascribed to the ring current (local field) effects observed for ions above graphene sheets and fragments.[79,80] This indicates that the sodium that is initially inserted at higher voltages is ionic in nature, implying essentially complete transfer of spin density from a Na atom to the carbon sheets, i.e., the presence of Na^+ ions. Furthermore, this observation suggests that there is little disruption to the aromatic ring currents that give rise to this phenomenon during the sloping region, consistent with mechanisms that localise charge near the carbon defects and not throughout the graphene sheets. We therefore suggest that sodium is largely deposited on pore walls and in interlayer regions, most likely near defects.

Table 3.1: Unit cell *a*-parameter values determined by performing real-space least-squares refinements in PDFGUI. A starting model of graphite was used. U_{33} parameters for all atoms were set to an initial value of 1, U_{11}, U_{22}, were set to 0.08. A spherical particle diameter of 20 Å was set. Unit cell parameters, phase scale factor, the spherical particle diameter, $delta_1$ (low-*r* peak sharpening parameter) and the thermal parameters were all refined during refinements including low-*r* ($r < 5$ Å) data. For refinements not using low-*r* data, the value of $delta_1$ was fixed to the value determined in refinements at low-*r*.

Range / Å	*a*-parameter / Å
0–2	2.465
2–5	2.459
5–10	2.451
10–15	2.444
15–20	2.440

The shift of the resonance to positive frequencies during the low voltage region of the electrochemistry, observed both during the *operando* experiment and *ex situ* (Figure 3.6), indicates that the local structural and / or electronic environment of the sodium ions that were inserted at higher potentials changes as more sodium is incorporated into the structure at lower potentials. This shift is due to an increased contribution from the Knight shift, which arises from the interaction of the nuclear spins with the unpaired electrons located at the Fermi level of the conduction band,[78] larger shifts indicating an increase of the Na 2s density of states at the Fermi Level. This implies that the sodium species becomes increasingly metallic during this period of the electrochemistry. We ascribe this process to Na^+ intercalation between appropriately-spaced disordered graphene layers, along with further insertion into empty environments nearby the defects, insertion now resulting in a reduction of the more ordered graphene sheets. The Na^+—C interaction gradually becomes less ionic as the carbon is reduced, affecting the shifts of sodium already in environments close to the defects. Secondly, where pores are sufficiently large, extended sodium clusters are formed that are more metallic in nature, resulting in even larger Knight shifts. This is consistent with DFT calculations and experimental data, suggesting the importance of defects,[28,61] and which also suggest that any clusters formed may be two dimensional in nature, reflecting the insertion between the expanded graphene sheets, and with SAXS measurements which imply that the carbon pores are filled at lower voltages.[59]

^{7}Li *operando* SSNMR measurements on similar electrode materials exhibit a peak at low-voltage which is shifted to approximately 40% of that of lithium metal.[81,82] This is significantly higher than for stage 1 GICs, which is presented as evidence for quasimetallic lithium contained in pores. In comparison, the peak at the end of sodium insertion is found shifted to much higher values, almost 70% the shift of sodium metal. In both cases, it is possible that the larger shift is in part due to insertion between carbon sheets with larger interlayer spacing. In addition, we note that the first ^{23}Na resonance to appear (−40 ppm) does not appear to shift during the sloping region of the electrochemistry. This is in contrast to the ^{7}Li measurements, where the first peak shifts from 0 to 18 ppm during the same period.[81,82] However, such a shift in the sodium spectra could be masked by the strong electrolyte signal

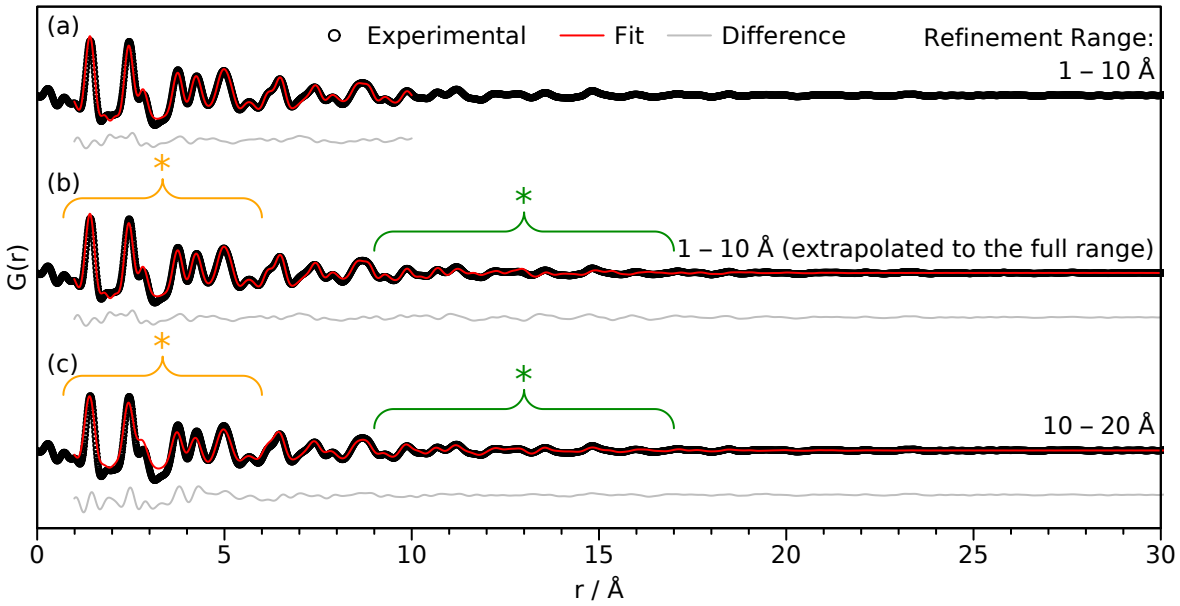

Figure 3.4: Real-space least-squares refinements of turbostratically disordered graphite against PDF data for the pristine electrode in the distance ranges (a) 1–10 Å, (b) 1–10 Å extrapolated to the full range over which peaks are observed experimentally, (c) 10–20 Å extrapolated to the full range. Black circles show experimental data, the red line shows the calculated PDF for the model, the offset grey line shows the residual ($G(r)_{model} - G(r)_{expt}$). The region marked by a green $*$ has a poor fit to the experimental data when using the parameters determined by a refinement at low-r, whereas the region marked by an orange $*$ has a poor fit when using the parameters determined by a refinement at high-r.

around −10 ppm or could be a result of using a different hard carbon than was used in the published lithium spectra.

Our preliminary PDF measurements for the electrodes after sodium insertion are consistent with this interpretation of the NMR data. A differential PDF, where the PDF for the pristine carbon is subtracted from the PDF at various points of discharge, highlights additional interactions present on the insertion of sodium (Figure 3.1b): samples discharged to 300 mV and 180 mV along the sloping region show only minor features at very low-r (< 7 Å), shown by the red asterisk in Figure 3.1b. A differential PDF between the samples discharged to 180 mV and 5 mV, obtained by subtracting the PDF for the sample discharged to 180 mV from the PDF of the sample discharged to 5 mV, shows the additional structure forming during the low potential electrochemical process (Figure 3.1b, bottom) implying clusters with a correlation length of approximately 10 Å are formed during the low-voltage region. These interactions are locally similar to those found in sodium-metal (Figure 3.8). This is consistent with increased Na ordering in this regime consistent with intercalation and/or Na pooling.

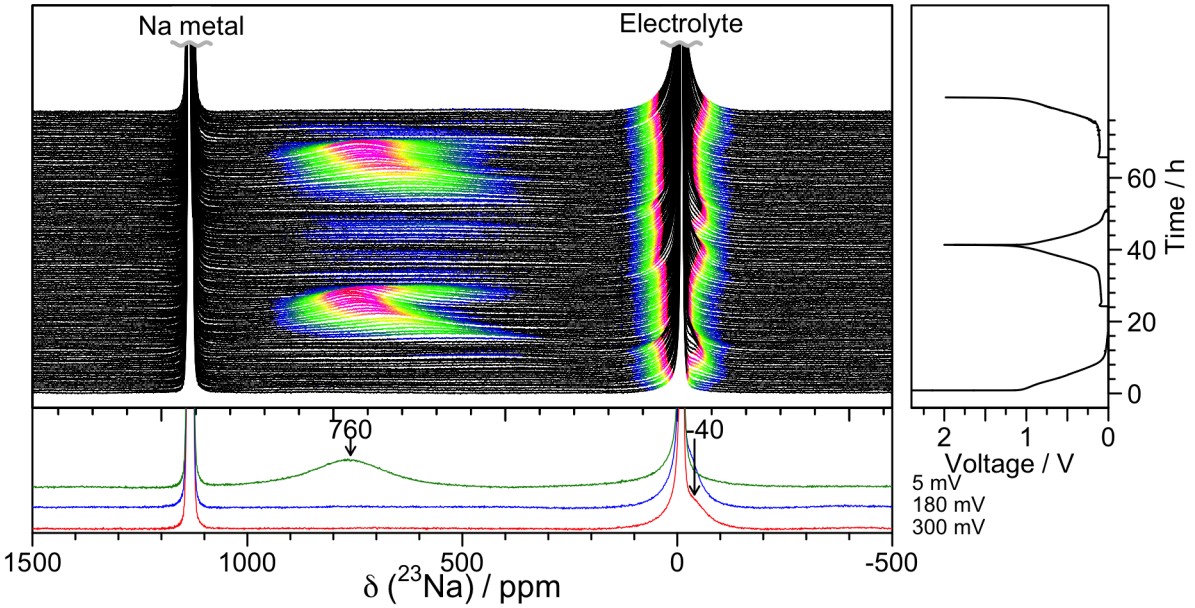

Figure 3.5: *Operando* ^{23}Na NMR spectra for an electrochemical cell with sodium metal and hard carbon electrodes, and a $NaPF_6$ electrolyte. Strong features corresponding largely to the electrolyte or metal have been truncated for clarity. Spectra are coloured in the region −200–1000 ppm according to their intensity. The corresponding electrochemistry is shown on the right-hand side and selected spectra are offset below. The cell was cycled at a rate of C/20 (corresponding to achieving a capacity of 300 mA h g^{-1} in 20 hours) between 2 and 0.05 V, and held at the end of each discharge until the current dropped to below C/100. The coulombic efficiency for the 1st cycle is 84% owing to additional capacity observed during discharge as a result of electrolyte breakdown to form an SEI layer. The coulombic efficiency increases to 97% for the 2nd cycle.

3.5 Conclusions

These results highlight new mechanistic aspects of the electrochemical insertion of sodium into hard carbons. *Operando* ^{23}Na ssNMR spectra are dominated by a single resonance, initially present close to 0 ppm, then shifting to positive frequencies. This is consistent with a two-stage mechanism. Ionic sodium ions are formed in the sloping region, consistent with charge localization, presumably near defects. Since defects are also responsible for creating regions with larger interplanar distances, some insertion between larger spaced graphene sheets may commence in this region, again this being associated with charge localization. At lower voltages, increased charge transfer to the Na^+ ions occurs, the ions becoming progressively more metallic. In this region, intercalation and Na pooling occurs, forming Na clusters or domains with coherence lengths of > 10 Å. PDF data additionally indicates that the turbostratically disordered, graphene-like fragments exhibit significant curvature. This will have significant effects on the interlayer arrangements and thus the regions which are available for sodium insertion. Our results imply that control of the pore architecture during synthesis could determine the size of sodium clusters formed, and thus grant the ability to tune the relative capacities of the high- and low-voltage processes.

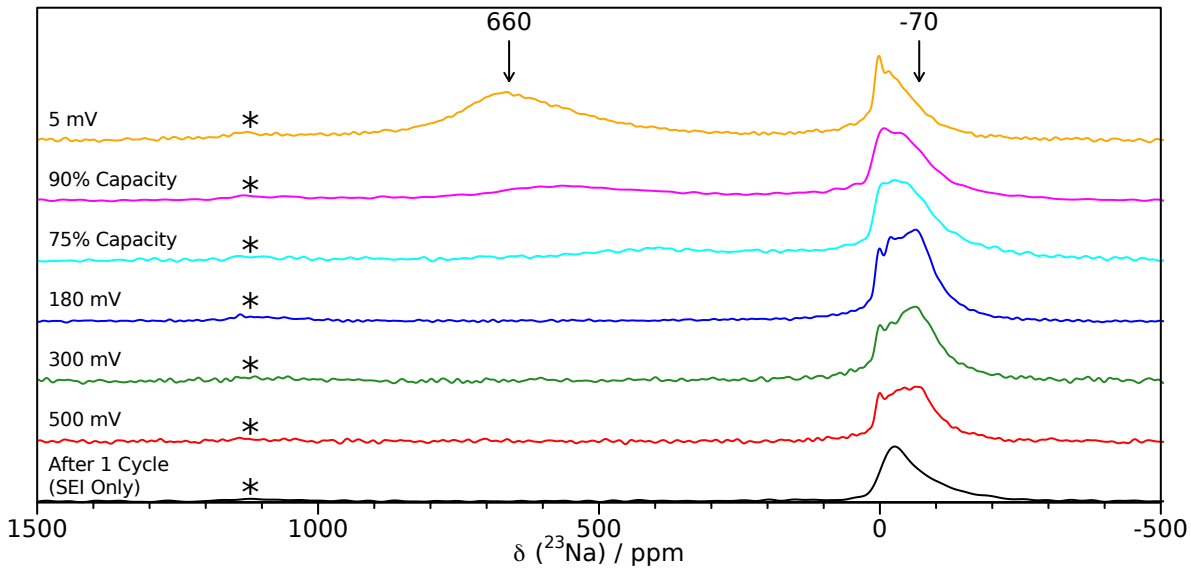

Figure 3.6: *Ex situ* ^{23}Na 60 kHz MAS NMR spectra of hard carbon anodes at various states of charge. Shifts are indicated for peaks not resulting from SEI or electrolyte. Spinning sidebands are indicated with an asterisk (∗). The black line corresponds to a spectrum after a complete discharge / charge cycle and represents the sodium that is irreversibly stored in the hard carbon. Intensities are normalised based upon the sample mass and the number of transients collected.

Table 3.2: Isotropic shift (δ_{iso}), quadrupolar coupling constant (C_Q), and asymmetry parameter of the quadrupole coupling (η_Q) for the three peaks used to deconvolute the spectra given in Figure 3.7.

	Peak 1 (Magenta)	Peak 2 (Cyan)	Peak 3 (Blue)
δ_{iso} / ppm	1.6	9.0	-4.0
C_Q / kHz	0	1500	2400
η_Q	0	0.6	0.6

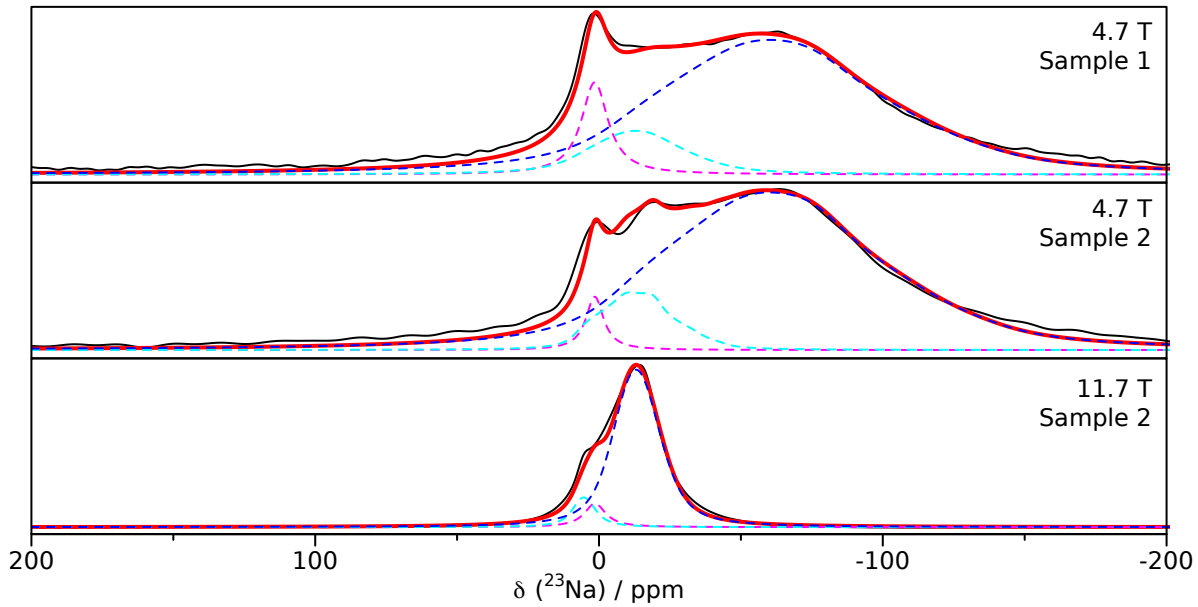

Figure 3.7: *Ex situ* ^{23}Na 60 kHz MAS NMR spectra of two different samples discharged to 180 mV and measured at magnetic fields of 4.7 T (samples 1 and 2) and 11.7 T (sample 2). Each spectrum was fit using the NMR parameters for 2nd order quadrupole coupling (central transition) in Bruker Topspin SOLA. A deconvolution of the spectra results in three peaks and is consistent with the influence of the magnetic field strength on the NMR signal line shape; the respective NMR coupling parameters are summarised in Table 3.2. Line broadening of 400 to 1800 Hz was applied to each signal to account for the breadth of each peak, resulting in the lack of the characteristic line shape features found in spectra of quadrupolar nuclei with large quadrupole coupling (CQ) values. The magenta peak (peak 1) is assigned to residual electrolyte as its intensity was found to vary based on the electrode washing procedure performed (samples 1 and 2 at 4.7 T). The cyan peak (peak 2) is assigned to SEI as its intensity does not vary in a similar manner. Peak 3 (blue) corresponds to sodium reversibly stored within the hard carbon framework.

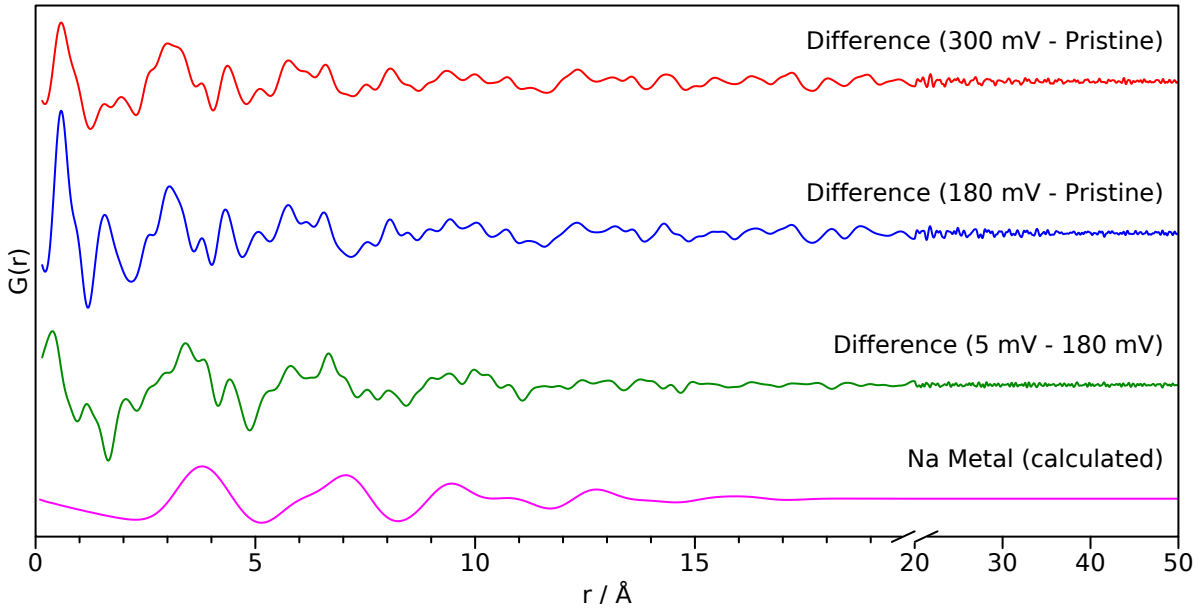

Figure 3.8: Difference PDFs during sodium insertion compared with the calculated PDF for sodium-metal. The PDF for sodium metal was calculated using PDFGUI, with $U_{11} = U_{22} = U_{33} = 0.13$ and a spherical particle diameter of 20 Å.

4 Structure-Property Relationships in Hard Carbon Anodes

Preface

In the following chapter, the carbon described as 1500 °C was provided by Professor Magdalena Titirici (Queen Mary University of London).

4.1 Introduction

There are a wealth of reports in the literature on the electrochemical performance of hard carbons as anodes for sodium-ion batteries.[34] It is clear that not all carbons are created equal, their performance in a battery being highly dependant on the synthetic procedure used to make them. This implies a strong link between the structure and electrochemical properties of these carbons. Recently, there have been reports showing that the performance of some carbons can be predicted using empirical relations between measurable properties.[83] However, the fundamental origins of this capacity are still poorly understood. Indeed, the mechanisms for the electrochemical reactions of sodium with hard carbon has developed into a somewhat popular problem in the literature. This is an area of constant study, but seemingly contradictory evidence means that the mechanisms are still under debate. For example, a study of sodium insertion into pseudographitic carbon did not find any evidence for pore filling by Raman and XRD,[84] nor did several NMR studies.[60,85,86] This is in contrast to, for example, *in situ* SAXS measurements,[59] our previous work (chapter 3), and a recent

DFT study,[87] all showing evidence of sodium pooling during the second discharge process. It has been suggested that such discrepancies may be as a result of the structure of each carbon under study, although it should be noted that several studies have used the same commercial carbon (Carbotron P(J) *Kureha Battery Materials Japan Co., Ltd.*),[74] not always reaching the same conclusions.[33] Hard carbons are widely regarded as the most likely anode material to be commercialised in the near future, so understanding these synthesis-structure-property relationships is vital for their optimisation to make them viable for large-scale use. To investigate this in more detail, we look at the structures of a number of hard carbons synthesised from glucose, and compare them to two commercially produced carbons. We then consider the sodium insertion mechanisms for a number of these carbons through *operando* PDF and SSNMR.

4.2 Experimental

4.2.1 Synthesis of Hard Carbons

Glucose (Sigma-Aldrich ≥ 99.5%) was dehydrated in air at 180 °C for 24 h. The resultant caramel was ball-milled in a zirconia jar for 5 minutes using a SPEX 8000M Mixer / Mill. The powder was then heated at 2 °C/min to the final pyrolysis temperature under flowing argon (40 cm^3/min) in a tube furnace. The overall yield from this process was 20–30 wt % for all samples. Following this, the samples were crushed prior to further characterisation.

4.2.2 Electrode Preparation for *Operando* Measurements

Each hard carbon was mixed with 10% polyvinylidene fluoride-co-hexafluoropropylene (Kynar) in an acetone (Sigma-Aldrich, anhydrous) solution, to which one drop of dibutyl phthalate (Sigma-Aldrich) was added for every 10 mg of binder. The resultant slurries were spread onto a glass substrate using a 300 µm doctor blade. After drying in air, the films were washed three times with diethyl ether (Sigma-Aldrich) and dried at 100 °C *in vacuo* prior to use.

4.2.3 Electrode Preparation for *Ex Situ* Measurements

Each hard carbon was mixed with 5% polyvinylidene fluoride-co-hexafluoropropylene (Kynar) in an N-Methyl-2-pyrrolidone (NMP, Sigma-Aldrich, anhydrous) solution. The resultant slurry was sonicated for 1 hour and spread onto a copper foil substrate using a 150 µm doctor blade. The films were dried in air, then at 100 °C *in vacuo* prior to use.

4.2.4 Electrochemical Experiments

Cells were prepared under an argon atmosphere using metallic sodium (Sigma Aldrich, 99.9%) as an anode. The electrolyte was 1 M $NaPF_6$ (Alfa Aesar, ≥99%) in propylene carbonate (Sigma Aldrich, anhydrous), and the separator was borosilicate glass fibre (Whatman, GF/A). *Ex situ* electrochemical measurements were per-formed with standard 2032 coin cell parts using a Biologic MPG2 battery cycler.

4.2.5 PDF Analysis

Operando PDF measurements were performed at beamline I15 at Diamond Light Source using a modified Swagelok cell adapted for X-ray transmission (Figure 2.4c on page 10). Cells were prepared in an argon atmosphere glove box (O_2, H_2O < 0.1 ppm). Electrochemical measurements were performed using an Ivium-n-Stat battery cycler. Cells were galvanostatically cycled in the potential range 2–0.005 V at a rate of C/20 (based on achieving 300 mA h g^{-1}) and held at the end of discharge until the applied current dropped to C/100.

Measurements were taken using an X-ray beam of energy 76 keV (λ = 0.1631 Å) and an amorphous silicon area detector (Perkin Elmer) in order to gather data to large values of momentum transfer. Data were collected at 60 minute intervals, using a total exposure time of 60 s per scan.

Ex situ PDF measurements were taken at beamline I15-1 (XPDF) at Diamond Light Source using 2.5 mm quartz capillaries. Measurements were taken using an X-ray beam of energy 76 keV (λ = 0.1631 Å) and an amorphous silicon area detector (Perkin Elmer). The total exposure time per scan was 900 s.

For all PDF experiments, background measurements were taken using identical cells / capillaries, but without the active material present. CeO_2 or Si standards were used to determine the sample geometry and the sample-to-detector distance. The data were converted to a function of intensity vs. Q using DAWN.[65] Standard corrections (background, Compton scattering, detector effects) were applied, and the data Fourier transformed to obtain G(r) using the software PDFGetX2.[66]

For the *operando* measurements, a number of issues outside of our control mean that the intensity of the raw data is not comparable between different scans on the same sample:

- The beam position of the beamline is not controlled within a feedback loop, which results in an inconsistent photon flux as a function of time; with no I0 monitor to allow for the correction of this post-measurement
- The volume expansion of the electrode results in a changing volume (and possibly density) of material within the beam
- It is not possible to know the exact composition of the section of the electrode we are observing

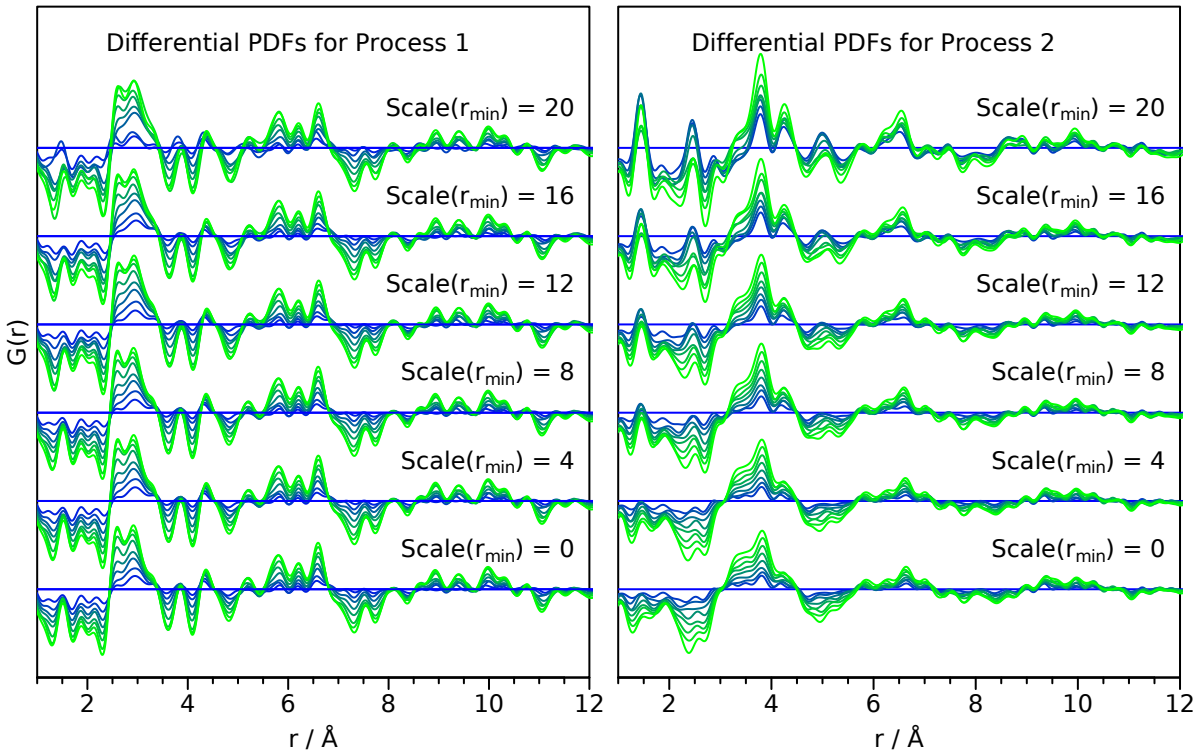

Figure 4.1: The effect of different lower bounds for the region over which data are rescaled, i.e. $r_{\text{min}} < r < 25\,\text{Å}$. The left hand plot corresponds to the first electrochemical process, the right to the second; in each case differential PDFs are plotted with blue lines corresponding to the start of the process and green to the end.

As such it was necessary to rescale the data after collection. PDFs were rescaled such that the total intensity over the range $15\,\text{Å} < r < 25\,\text{Å}$ remained constant as a function of time. This range was chosen to be greater than the range over which we observe changes in the PDFs. The region over which data are rescaled has an effect on the intensity of the first two peaks in the PDFs (and thus in the differential PDFs calculated from them), but no significant impact beyond this (Figure 4.1).

Structural refinements were performed using the DiffPy-CMI complex modelling infrastructure software.[88] The reduced structure function $F(Q)$ was calculated from a Debye sum (equation 2.7 on page 16) and Fourier transformed over the range 1–24 Å^{-1} to give the real-space PDF. Refinements were performed simultaneously in reciprocal-space ($F(Q)$) and real-space ($G(r)$). R_w values were calculated using the following modification to equation 2.18 on page 22:

$$R_w = \sqrt{\frac{\sum_{i=1}^{N} w(r_i)\left[G_{\text{exp}}(r_i) - G_{\text{calc}}(r_i)\right]^2 + \sum_{i=1}^{N} w(Q_i)\left[F_{\text{exp}}(Q_i) - F_{\text{calc}}(Q_i)\right]^2}{\sum_{i=1}^{N} w(r_i) G_{\text{exp}}^2(r_i) + \sum_{i=1}^{N} w(Q_i) F_{\text{exp}}^2(Q_i)}} \tag{4.1}$$

where $w(r_i)$ and $w(Q_i)$ are the weighting factors for data points r_i and Q_i, which depend upon the statistical quality of the data point.

Creating a Curved Graphene Fragment

PDFs for the pristine carbons were modelled as curved graphene fragments. Curvature being introduced by constraining a graphene layer to lie on the surface of an imaginary ellipsoid. The radii of curvature of this ellipsoid may then be changed to adjust the curvature in the model. These fragments are created from a planar, rectangular graphene fragment of width x and height y by placing it at the centre of a box with dimensions $1 \times 1 \times 1$ such that each atom (i) has normalised coordinates ($x_{\text{layer},i}$, $y_{\text{layer},i}$, 0). An ellipsoid with radii ($A^{-0.5}$, $B^{-0.5}$, 0.5) is placed at (0.5, 0.5, 0.5) such that it just touches the graphene layer at its lowest point. The ellipsoid is described by the following expression:

$$A\left(x_{\text{ellipsoid}} - 0.5\right)^2 + B\left(y_{\text{ellipsoid}} - 0.5\right)^2 + 4\left(z_{\text{ellipsoid}} - 0.5\right)^2 = 1 \tag{4.2}$$

We create a model where the carbon atoms are placed at the intersection of a line drawn from each atom to the centre of the ellipsoid with the surface of the ellipsoid, the parametric equations for these lines are as follows:

$$x_{\text{line},i} = x_{\text{layer},i} + t\left(0.5 - x_{\text{layer},i}\right) \tag{4.3}$$

$$y_{\text{line},i} = y_{\text{layer},i} + t\left(0.5 - y_{\text{layer},i}\right) \tag{4.4}$$

$$z_{\text{line},i} = 0.5t + nd \tag{4.5}$$

Where the parameter n is included to allow us to create multiple identical layers separated by a distance d, it takes integer values from 0 to one fewer than the total number of layers. The points of intersection are then given by solving the following equation:

$$\begin{aligned} &\left\{A\left(0.5 - x_{\text{layer},i}\right)^2 + B\left(0.5 - y_{\text{layer},i}\right)^2 + 1\right\} t_i^2 \\ &+2\left\{Ax_{\text{layer},i}^2 + By_{\text{layer},i} - By_{\text{layer},i}^2 - 0.25A - 0.25B - 1\right\} t_i \\ &+ \; Ax_{\text{layer},i}^2 - AX_{\text{layer},i} + By_{\text{layer},i}^2 - By_{\text{layer},i} + 0.25A + 0.25B = 0 \end{aligned} \tag{4.6}$$

Solving for t_i gives the coordinates for atom i on the curved surface of the ellipsoid:

$$t_{\text{i}} = \frac{-b - \sqrt{b^2 - 4ac}}{2a} \tag{4.7}$$

Where:

$$a_i = A\left(0.5 - x_{\text{layer},i}\right)^2 + B\left(0.5 - y_{\text{layer},i}\right)^2 + 1 \tag{4.8}$$

$$b_i = 2\left(A\left(x_{\text{layer},i} - x_{\text{layer},i}^2\right) + B\left(y_{\text{layer},i} - y_{\text{layer},i}^2\right) - 0.25A - 0.25B - 1\right) \tag{4.9}$$

$$c_i = A\left(x_{\text{layer},i}^2 - x_{\text{layer},i}\right) + B\left(y_{\text{layer},i}^2 - y_{\text{layer},i}\right) + 0.25A + 0.25B \tag{4.10}$$

In addition, the coordinates in each direction are scaled by a factor in the same manner as the lattice parameters a, b, and c for a crystal. As the initial model is 2D, the radius of curvature in the c direction is simply given by half of the c scale factor / lattice parameter. The parameters A, B, and d may be refined along with the scale factors.

4.2.6 Solid-state NMR Spectroscopy

Operando ssNMR measurements were performed using in-house designed cells based upon a cylindrical capsule (Figure 2.4d on page 10). Cells were prepared in an argon atmosphere glove box (O_2, $H_2O < 0.1$ ppm) using the same materials as for the coin cell measurements. Electrochemical measurements were performed using a Bio-Logic VSP battery cycler. Cells were galvanostatically cycled in the potential range 2–0.005 V at a rate of C/20 (based on achieving 300 mA h g^{-1}) and held at the end of discharge until the applied current dropped to C/100.

A Bruker Avance 300 MHz spectrometer (^{23}Na Larmor frequency = 79.39 MHz) was fitted with a static probe system with automatic tuning and matching capabilities (along with connections for an external battery cycler).[68] The resonance circuit was recalibrated immediately prior to each measurement by minimising the standing wave ratio of the forward and reflected power for a low power (0.01 W) continuous wave pulse. The electrochemical cell was aligned such that the electrodes were perpendicular to the applied field.

In order to maximise the signal-to-noise ratio for a time-restricted measurement, a one-pulse sequence was used. A 90° pulse corresponds to 3.5 µs at 200 W using an 11 mm diameter silver coil. 30000 transients were collected for each spectrum, using a recycle delay of 0.05 s (31 minutes per spectrum). The ^{23}Na signals were referenced using a 1 M solution of NaCl at a shift of 0 ppm.[69] Spectra were Fourier transformed using Bruker Topspin, individually phased and backgrounds subtracted.

4.3 Results

In the following, we refer to a number of different hard carbons. In order to differentiate between them, the following nomenclature will be used: two commercial carbons are studied, for which the synthesis procedures are unknown. The first is produced by *Kureha Battery Materials Japan Co., Ltd.* and is referred to as "carbotron".[74] The second is produced by *Faradion Ltd.* and is referred to as "Faradion". Furthermore, a number of glucose-derived hard carbons are studied (produced as per section 4.2.1), these are referred to by their pyrolysis temperatures — e.g. "1100 °C" represents a hard carbon produced by pyrolysis of glucose at 1100 °C.

4.3.1 Elemental Analysis

Table 4.1 shows the composition of each of the carbons studied. In all cases, we see ≥ 90 w.t.% carbon, for the higher temperature carbons, and the commercial samples ≥ 97 w.t.% carbon is seen.

Table 4.1: The C, H, and N wt. % for each of the carbons as determined by elemental analysis. The remainder is assumed to be oxygen.

Carbon	C	H	N	O (Assumed)
900 °C	90.2	0.4	0.0	9.6
1000 °C	94.2	0.5	0.3	5.0
1100 °C	97.1	0.4	0.0	2.5
1500 °C	100.0	0.0	0.0	0.0
Carbotron	97.2	0.0	0.0	2.8
Faradion	99.5	0.0	0.0	0.5

4.3.2 PDF Analysis of Pristine Carbons

Figure 4.2 shows the PDF, derived from the Fourier transformed X-ray total scattering data, of a commercial hard carbon (carbotron). The positions of peaks at interatomic distances, r, are close to those in a graphene fragment. The rapid decrease in intensity at $r > 5$ Å shows clear evidence of the lack of any long-range ordering within the structure. In addition, the absence of any inter-layer graphitic peaks (the shortest of which would be found at 3.35 Å and 3.64 Å) implies turbostratic disorder in the stacking of these graphene layers. Beyond 25 Å, no further correlations are observed. This lack of long-range ordering results from disorder within the structure, which likely results either from termination of the fragments or curvature of the sheets.

The experimental PDF can be simulated using a number of different methods. The simplest uses a periodic graphite model with expanded layers and a large value for the U_{33} thermal displacement parameter to simulate disorder between the layers (chapter 3). However, it is not possible to simulate curvature of the graphene-like sheets using such a model. More complex models can be created using methods such as RMC refinement,[89,90] and DFT.[87]

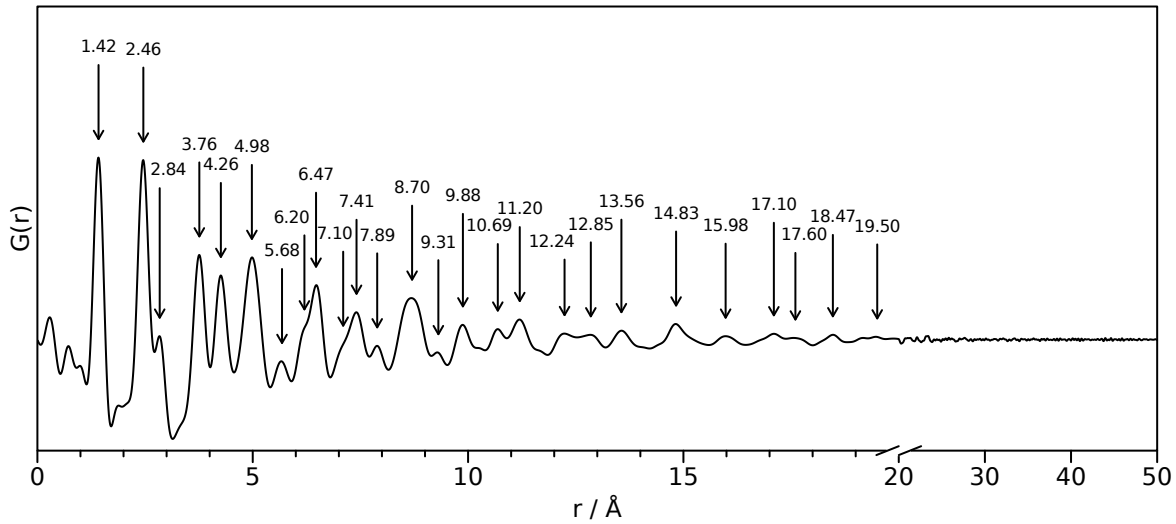

Figure 4.2: Experimental PDF data for a commercial hard carbon (carbotron), significant peaks ($r < 20$ Å) are labelled.

However, such models are unlikely to provide a unique fit to the data owing to the large number of atomic positions that are refined. Furthermore, the complexity of such models makes interpretation difficult. Herein we attempt to model the carbons using the smallest number of atoms, and the smallest number of refined parameters that can provide a good fit to the data. In effect, this gives the "average" local structure analogous to a unit cell, which describes the smallest set of atoms required to describe a crystal structure.

We take n aperiodic graphene fragments with dimensions $x \times y$, which are stacked in either an eclipsed or staggered arrangement with separation d. These fragments are constrained to lie on the surface of an ellipsoid with three independent radii of curvature (full details in section 4.2.5). We then refine this structure against the real-space PDF and the reciprocal-space total scattering data simultaneously. The radii of curvature are allowed to vary, along with the layer separation (d), an overall scale factor, delta_1 (low-r peak sharpening parameter), and intra- and inter-layer thermal displacement parameters (using the method outlined by Billinge *et al.*)[91] for a total of eight refined parameters. This refinement is then repeated for different values of x and y, and different numbers of layers. These parameters cannot be refined directly as changing the number of atoms introduces a discontinuity into the fit. We then select all models within 10% of the lowest R_w value, and choose the model with the lowest inter-layer thermal displacement parameter. From this we interpret the number of layers. The fit containing this number of layers, with the lowest R_w is chosen as the final model.

This method for choosing a "best" model from the candidates accounts for situations in which a larger number of layers that are more disordered with respect to each other, via a larger inter-layer thermal displacement parameter, gives a marginal improvement to the fit. We aim to find the simplest possible model to explain the total scattering data, and as such favour a smaller, more ordered model over a more disordered variant when the quality of the fit is equivalent. In reality, there is likely to be a distribution of different structures within the material which is not captured using this method of modelling.

Using this method, the experimental real- and reciprocal-space scattering data for two commercial hard carbons, and four glucose derived hard carbons (with different pyrolysis temperatures) were fitted. In each case, we obtain good fits to both the entire r-range of the real space data, and Q-range of the reciprocal space data. Raw data is shown in Figure 4.3, and an example of the fit to data for the 1100 °C sample ($R_w = 0.16$) is shown in Figure 4.4. Note that fitting in both real- and reciprocal-spaces is important as, whilst $G(r)$ is sensitive to the curvature of the sheets, it is less sensitive to the number of layers. Conversely, $F(Q)$ is extremely sensitive to the number of layers via the (002) peak as shown in Figure 4.5. The advantages gained through such dual refinements are also more generally true for other systems, where refinements of $G(r)$ tend to place more emphasis on the short-range structure, whereas $F(Q)$ gives a more even weighting across all length scales.[92]

Performing this analysis on four glucose-derived carbons prepared at pyrolysis temperatures of 900 °C (cyan), 1000 °C (magenta), 1100 °C (green), and 1500 °C (blue) reveals significant changes to the model structures that provide the best fit (Table 4.2 and Figures 4.6 and 4.7). As the synthesis temperature increases, we find that the dimensions of the frag-

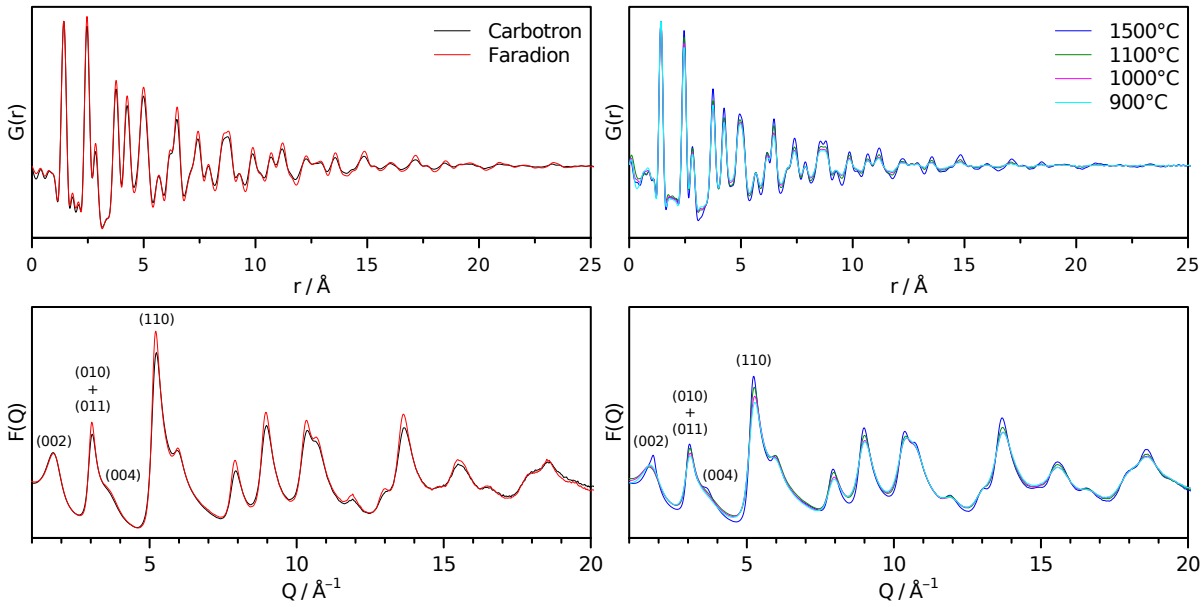

Figure 4.3: A comparison of the PDFs and reduced structure functions, $F(Q)$, for two commercial carbons: carbotron (black), and Faradion (red), and four glucose-derived carbons with pyrolysis temperatures of 900 °C (cyan), 1000 °C (magenta), 1100 °C (green), and 1500 °C (blue). $F(Q)$ peaks below 6 Å^{-1} are indexed based on the graphite unit cell.

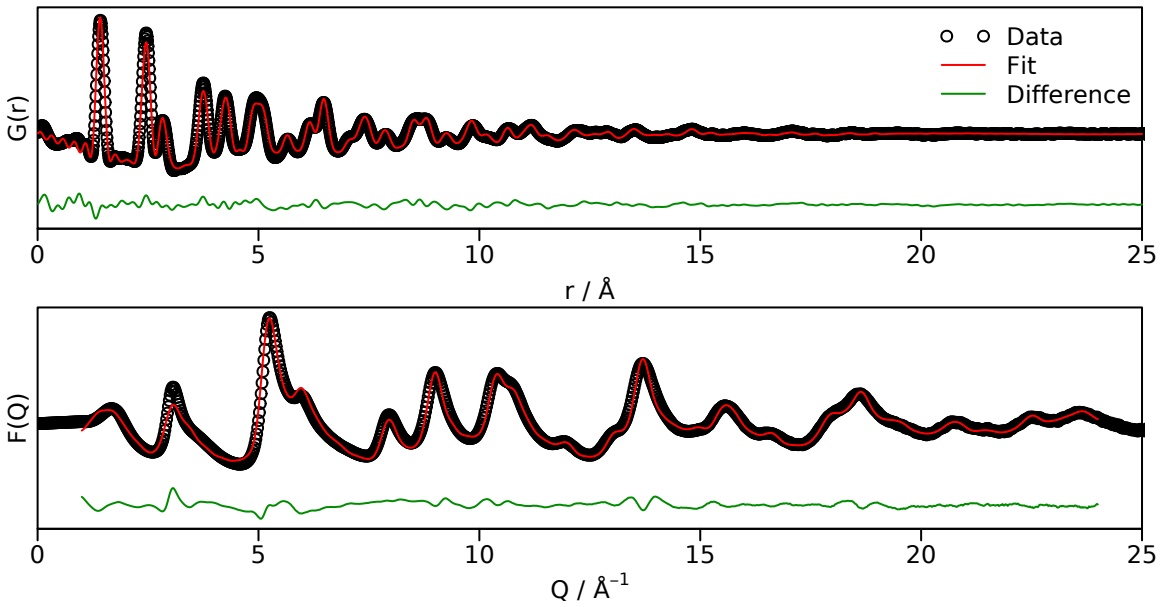

Figure 4.4: A fit of the PDF and reduced structure function, $F(Q)$, of the 1100 °C sample using a model consisting of curved graphene sheets ($R_w = 0.16$).

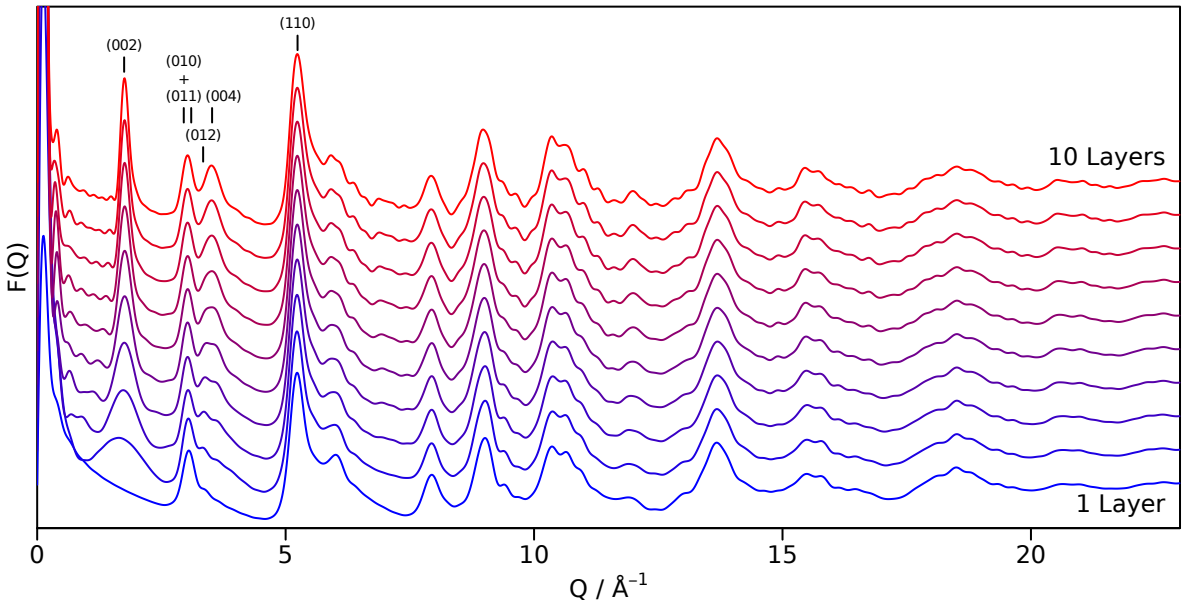

Figure 4.5: Simulations of the reduced structure function, $F(Q)$, for models with different numbers of identical carbon layers. Peaks below 6 Å^{-1} are indexed based on the graphite unit cell.

ment increases, however, the curvature of the fragment appears to remain consistent. At all temperatures, we observed cylindrical curvature of a similar magnitude. The commercial carbons appeared notably less asymmetrical, both having approximately square (rather than rectangular) fragment shapes. Faradion has the larger fragment size, and displays similar curvature to the glucose based carbons. Carbotron, however, displays spherical, rather than cylindrical, curvature. Enforcing cylindrical curvature in this case results in a minor decrease in the quality of fit; R_w = 0.19 (spherical), 0.20 (cylindrical) — an equivalent difference to a change in one of the x, y dimensions of the model by 4–6 Å.

Table 4.2: Fragment sizes, number of layers, and number of atoms in the best fit models for each carbon.

Carbon	Dimensions of Model / Å	# Layers	# Atoms in Model
Carbotron	18 × 18	2	240
Faradion	22 × 20	2	340
900 °C	15 × 15	2	132
1000 °C	20 × 12	2	204
1100 °C	22 × 12	2	204
1500 °C	26 × 18	2	360

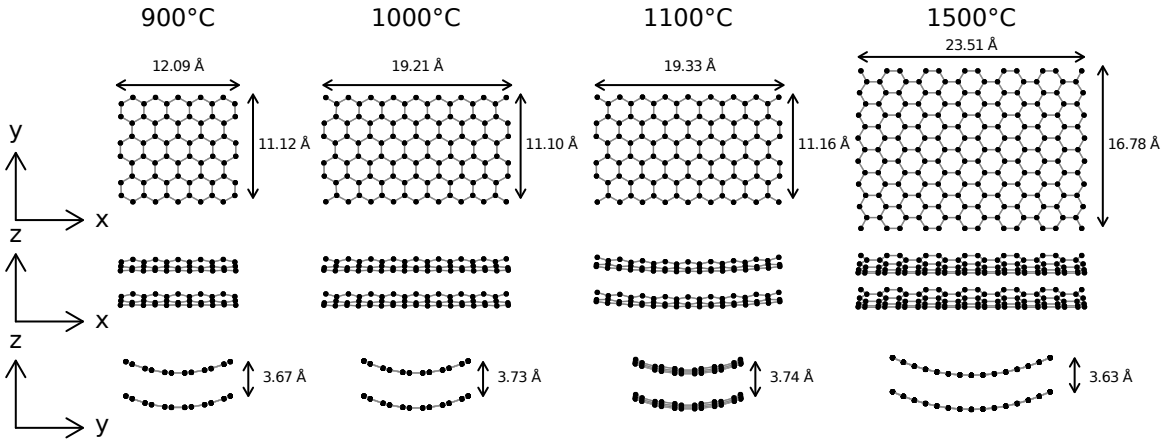

Figure 4.6: Structures resulting from PDF and $F(Q)$ refinements of the glucose-derived carbons.

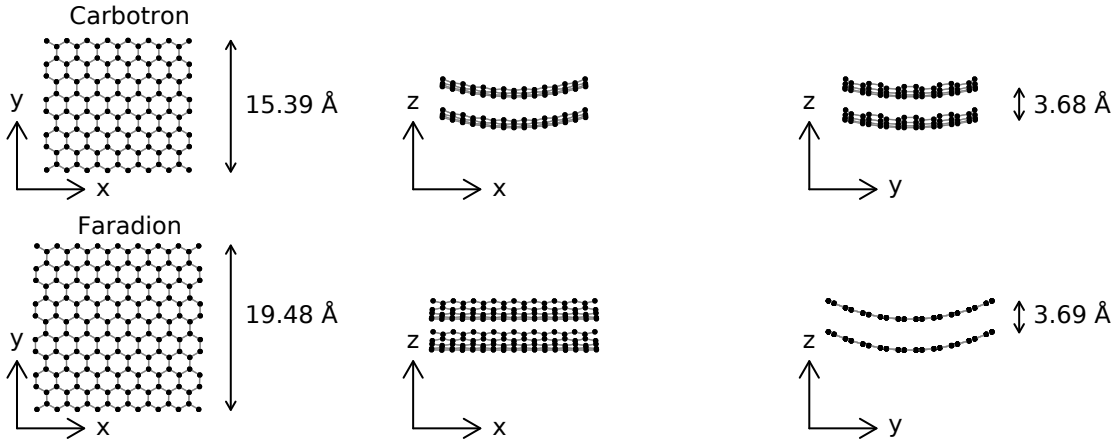

Figure 4.7: Structures resulting from PDF and $F(Q)$ refinements of the commercial carbons.

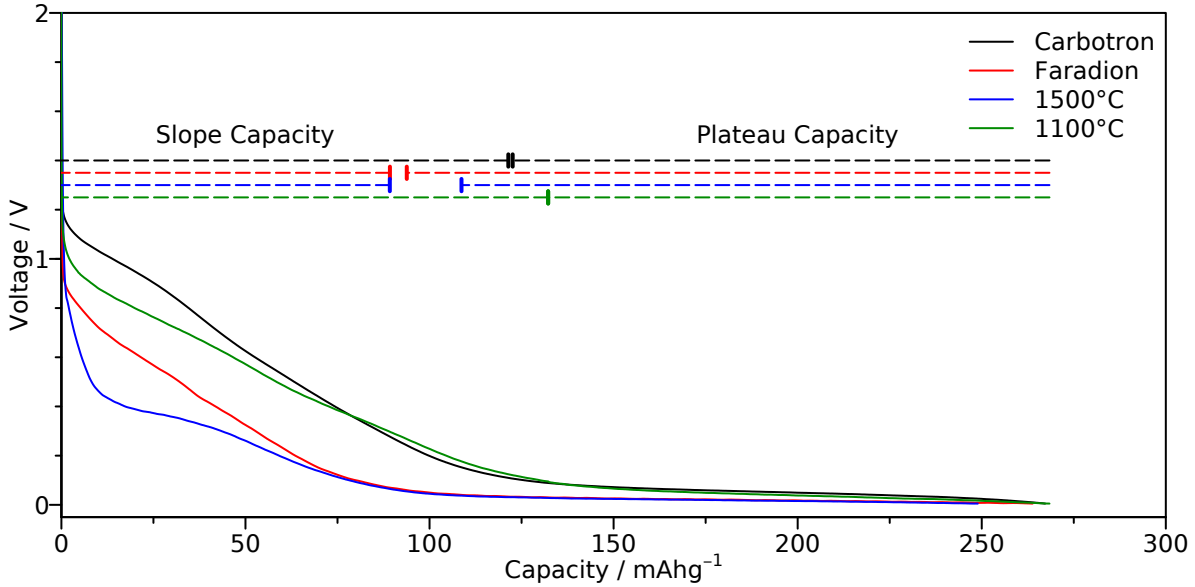

Figure 4.8: Electrochemistry data for a sodium–hard carbon cells cycled at a rate of C/20 (corresponding to achieving a capacity of 300 mA h g^{-1} in 20 hours) between 2 and 0.005 V. The black line represents carbotron, red Faradion, blue 1500 °C, and green 1100 °C. The dashed lines offset above illustrate the total capacity achieved on the slope and plateau processes for each carbon.

4.3.3 Electrochemistry

Figure 4.8 shows the experimental galvanostatic electrochemical profile obtained at a rate of C/20 for the two commercial carbons, and the two high temperature glucose-derived carbons (1100 °C, and 1500 °C). In agreement with previous reports, we see both a sloping process, and a plateau process for each of the carbons. In order to differentiate between these two processes, we performed differential capacity analysis on each of the datasets, defining the plateau process to begin when $dQ/dV \leq$ -0.4, i.e. the point immediately following the change in gradient. This method was used rather than the more typical potential-based definition in order to be resilient towards different overpotentials; these maybe caused by differences in resistance between the different carbons, film formulation, differences in thickness, porosity, etc. This is equivalent to potentials of 0.15 V, 0.17 V, 0.16 V, and 0.14 V for carbotron, Faradion, 1500 °C, and 1100 °C, respectively. It is clear that the capacity achieved on the two processes is different for each of the carbons, this is summarised in Table 4.3.

4.3.4 *Operando* NMR

Operando ^{23}Na ssNMR measurements were performed on four of the carbons. The results are shown in Figure 4.9. In all cases, two peaks are observed at −10 ppm and 1135 ppm corresponding to the $NaPF_6$ electrolyte and the sodium metal counter electrode, respectively. From the start of discharge, until approximately 0.8 V, these are the only peaks observed. This is consistent with electrolyte decomposition on the surface to form the SEI layer.

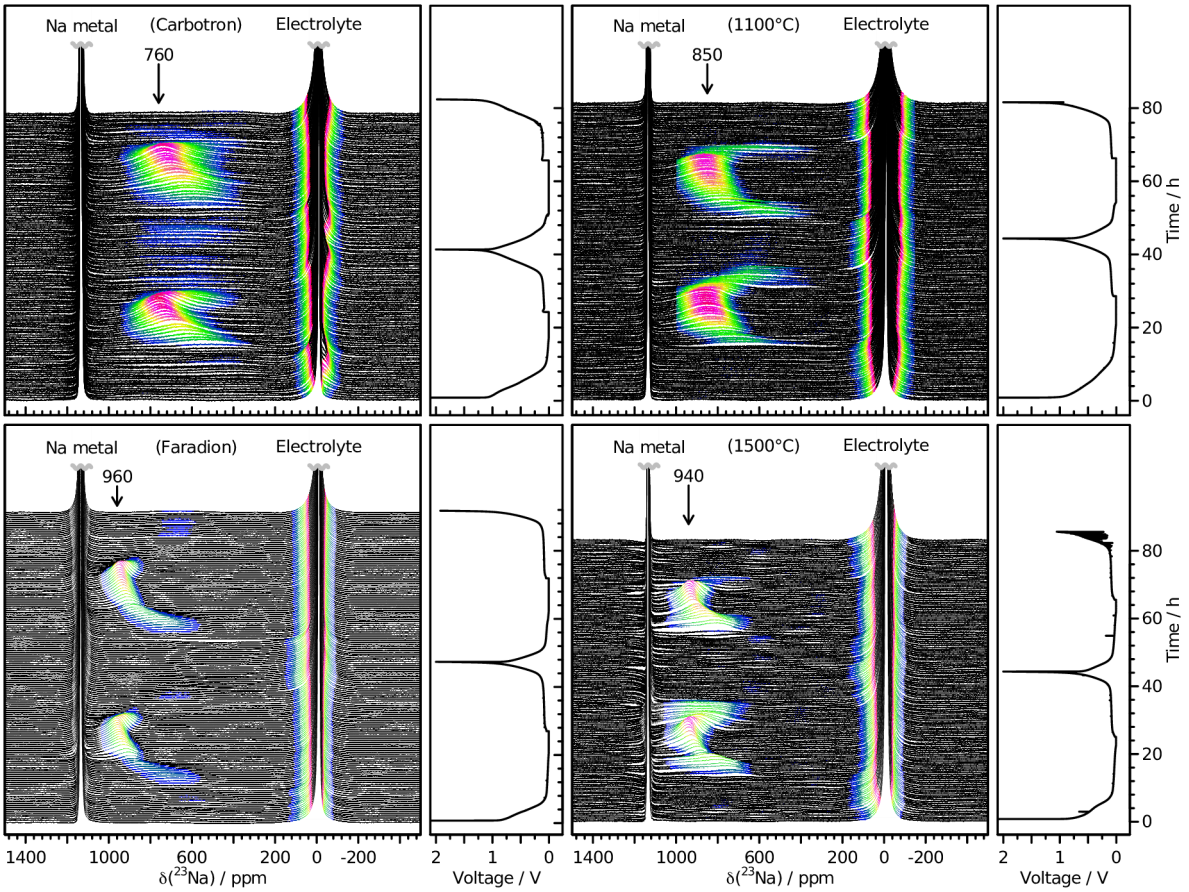

Figure 4.9: Four *operando* ^{23}Na NMR spectra for electrochemical cells with sodium metal and hard carbon electrodes, and a $NaPF_6$ electrolyte. Strong features corresponding largely to the electrolyte or metal have been truncated for clarity. Spectra are coloured in the region −200–1000 ppm according to their intensity. Peak maxima for the spectra following complete sodium insertion are indicated. The corresponding electrochemistry is shown on the right-hand side of each spectrum. The cells were cycled at a rate of C/20 (corresponding to achieving a capacity of 300 mA h g^{-1} in 20 hours) between 2 and 0.005 V, and held at the end of each discharge until the current dropped to below C/100. The hard carbons used were (clockwise from top-left) carbotron, 1100 °C, 1500 °C, and Faradion.

Table 4.3: A breakdown of the capacity obtained on each of the two processes for the four carbons whose electrochemical profiles are shown in Figure 4.8.

Carbon	Slope Capacity / mA h g^{-1}	Plateau Capacity / mA h g^{-1}	Plateau / Slope
Carbotron	121	146	1.21
Faradion	89	175	1.97
1500 °C	89	160	1.80
1100 °C	132	136	1.03

During the first electrochemical process, we only observe changes in the diamagnetic region around 0 ppm. Unfortunately, this is masked by the strong electrolyte signal, this means that comparison of the shift produced by sodium insertion into the different carbons is not easily possible. However, the diamagnetic nature of the shift in all cases indicates that the sodium inserted is ionic in nature, rather than metallic. During the second electrochemical process, a peak is observed to grow and to shift to higher frequencies, for each of the carbons tested. The final shift ranged from 760 ppm to 960 ppm depending on the carbon (Figures 4.9 and 4.10). In all cases the high value of the chemical shift is consistent with the formation of a metallic sodium species during this stage of the electrochemistry.

4.3.5 *Operando* PDF

Operando PDF data were collected for the two commercial carbons. Whilst changes to the real-space $G(r)$ are subtle (Figure 4.11), they are highlighted by differential PDFs, and are clearly visible in the reciprocal-space $F(Q)$. Figure 4.12 shows the first few peaks in the $F(Q)$ for carbotron, there are clear isosbestic points in the first broad feature around 2 Å^{-1}, that occur both during the sloping process, and during the plateau process. This provides clear evidence for two two-phase reactions during these regions of the electrochemistry.

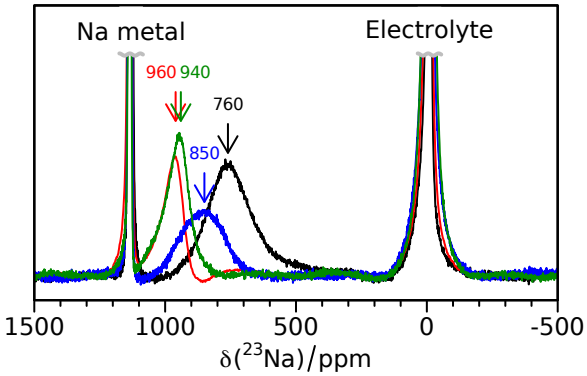

Figure 4.10: A single spectrum representing the end of discharge from each of the four *operando* measurements shown in Figure 4.9. Strong features corresponding largely to the electrolyte or metal have been truncated for clarity, and shifts are indicated for the peaks corresponding to sodium within the hard carbon structures. Black represents carbotron, red Faradion, blue 1100 °C, and green 1500 °C.

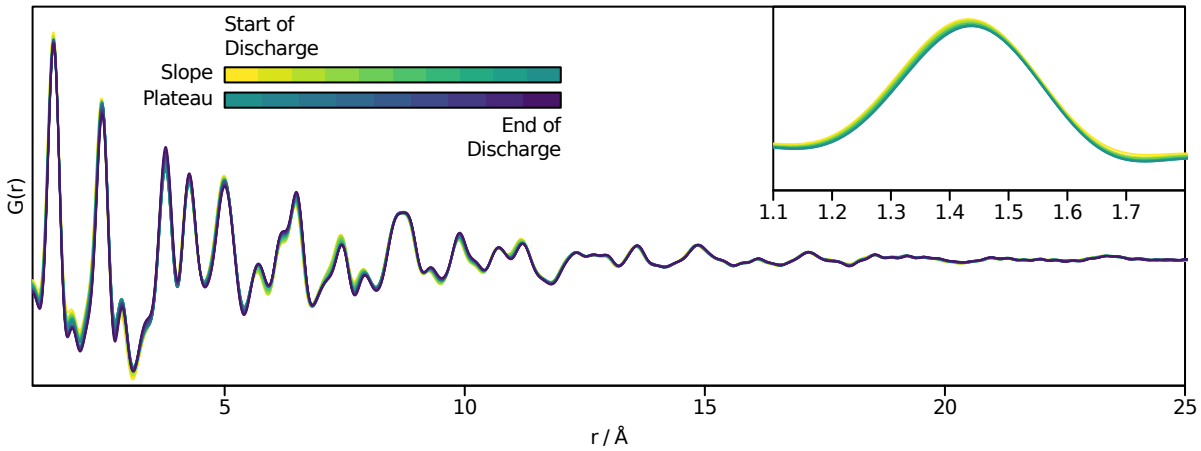

Figure 4.11: *Operando* PDFs obtained during the first discharge of a sodium-carbotron cell plotted on top of each other, demonstrating that the changes during cycling are extremely subtle. Inset: A close-up of the first peak during the sloping electrochemical process showing the sharpening of the left hand side of the peak during sodium insertion.

Moving into real-space, differential PDFs, obtained by subtracting the first PDF obtained during an electrochemical process (i.e. slope or plateau) from the PDFs measured during that process, show more clearly the changes that are occuring (Figure 4.13). Both carbons appear to form similar phases during the two processes. The sloping process results in a phase with a correlation length of approximately 12 Å, it shows broad features at 2.8 Å, 6.0 Å, and 9.5 Å, which are overlaid by peaks with a lower periodicity. During the plateau process, the phase formed shows a much smoother PDF, with broad peaks around 3.8 Å, 6.5 Å, and 9.7 Å, there are no additional sharp peaks in this phase beyond Fourier truncation errors.

As noted earlier, the differential PDFs for the sloping process appear to contain numerous sharp peaks superimposed on a broader component. To investigate this more closely, we have attempted to deconvolve the differential PDF corresponding to the end of this process into two components: a "sharp" component containing all the peaks of low-periodicity, and

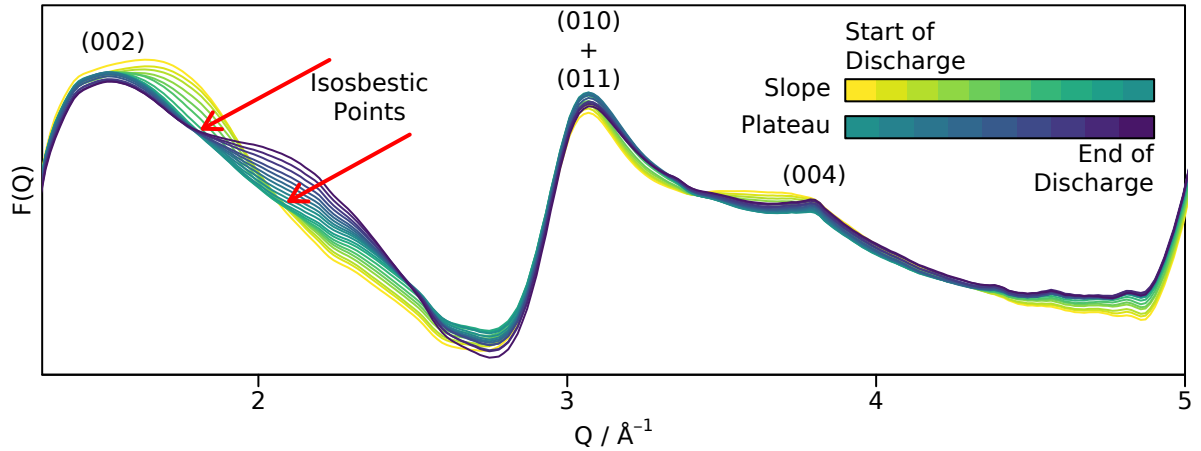

Figure 4.12: The reduced structure function, $F(Q)$, obtained during the same experiment as the PDF data in Figure 4.11. The two isosbestic points observed during discharge (one during each of the two processes) are indicated on the first peak. Peaks are indexed based on the graphite unit cell.

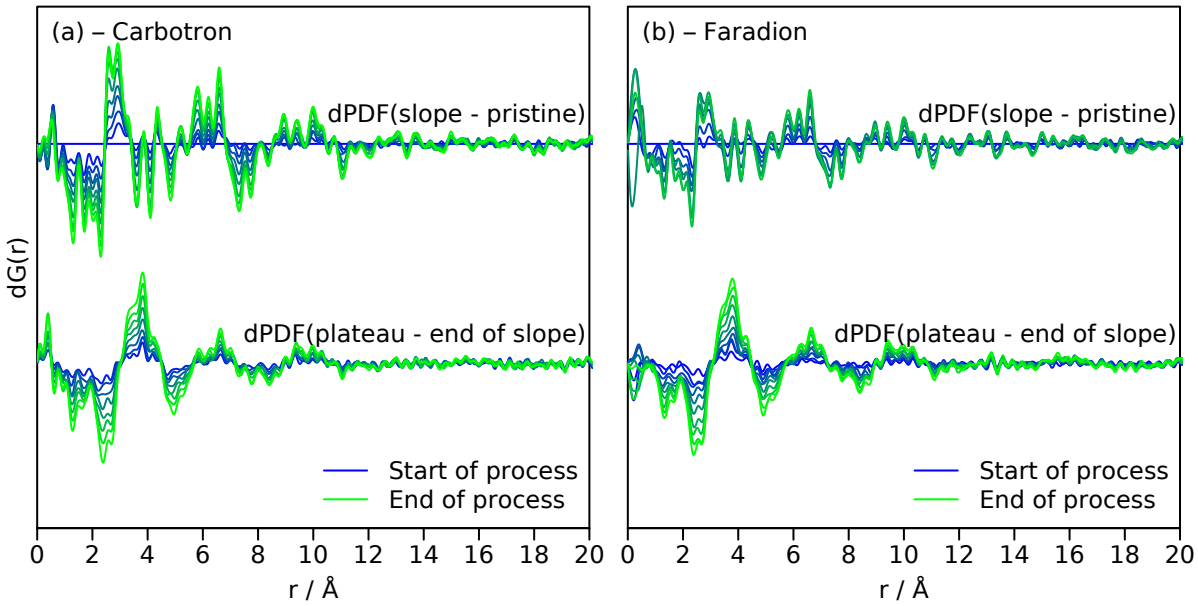

Figure 4.13: Differential PDFs obtained by subtracting PDFs taken during an *operando* experiment of (a) a sodium-carbotron cell, (b) a sodium-Faradion cell from the PDFs obtained at the start of each electrochemical process.

a "broad" component, which is as smooth as possible and only contains the broad humps around 2.8 Å, 6.0 Å, and 9.5 Å. The sharper peaks appear at distances slightly greater than the C-C interactions within the pristine material. This implies there may be some changes to the carbon framework during this process, specifically the expansion of some of the C-C bonds. In order to test whether this explains this component, we created a PDF for an expanded carbon matrix by taking the PDF acquired before sodium insertion, and expanding the r-axis in a linear manner (equation 4.12). To assess whether this is a valid model for the sharp component of the differential, we need to convert this into a differential PDF by subtracting from it the PDF for the pristine material (equation 4.13). The broad component is then simply the difference between the measured differential PDF and this calculated differential (equation 4.14).

$$dG(r) = G_{\text{end of slope}}(r)/s_1 - G_{\text{pristine}}(r) \tag{4.11}$$

$$r_{\text{expanded}} = r_{\text{add}} + r_{\text{min}} + (r - r_{\text{min}})\, r_{\text{multi}} \tag{4.12}$$

$$dG_{\text{sharp}}(r) = s_2 \left(G(r_{\text{expanded}}) - G(r) \right) \tag{4.13}$$

$$dG_{\text{broad}}(r) = dG(r) - dG_{\text{sharp}}(r) \tag{4.14}$$

Where s_1, and s_2 represent scale factors, r_{add} represents the additive expansion of the carbon matrix, r_{multi} represents the multiplicative expansion of the carbon matrix, and r_{min} represents the distance below which expansion does not occur. The necessity of scale factors is discussed further in section 4.2.5. If expanded carbon is a good model for the sharp component, we will be able to find values for r_{add}, r_{multi}, and r_{min} that give a smooth broad component. We optimised these parameters by minimising the sum of squares of the first derivative of the broad component:

$$\sum_r \left\{ \frac{\partial G_{\text{broad}}(r, s_1, s_2, r_{\text{add}}, r_{\text{min}}, r_{\text{multi}})}{\partial r} \right\}^2 \tag{4.15}$$

The result of this deconvolution is shown in Figure 4.14a. It is clear that this deconvolution method is able to effectively separate a sharp component from the underlying broad component. This demonstrates that a combination of expansion of the carbon matrix along with the growth of a more disordered phase is a valid model for the structural changes during this region of the electrochemistry. Looking closely at the experimental PDF (Figure 4.11 inset), we see that the intensity of the left hand side of the peak reduces slightly more than the right during sodium insertion, suggesting that we selectively lose the shortest C-C bonds. Together, this implies that only the regions with the shortest C-C bonds are suitable for Na insertion at higher voltages, and, following reaction with sodium, the C-C bonding within the layer expands, resulting in a narrower distribution of C-C bond lengths. Preliminary modelling suggests that the broad component may be explained simply through the addition of sodium atoms above the curved graphene layer that was used to model the pristine material. Using a NaC_{15} model (Figure 4.15), the PDF calculated using only Na-C and Na-Na correlations is a reasonable match to the broad component. Further work is necessary to confirm this, and to optimise the number and positions of sodium atoms. There appear to be slight differences between the two carbons, however, this may be explained simply by lower intensity in the Faradion dPDF along with significant noise.

During the plateau process, both the phases formed are extremely similar for both carbons. The final differential PDFs for these processes are shown in Figure 4.14b along with the calculated PDF for sodium metal. The strong similarity between the PDF for sodium metal and those resulting from sodium insertion within the carbon is a strong indication that we are forming nano-sized clusters of sodium during this electrochemical process. A possible additional correlation not expected for a cluster consisting solely of sodium atoms is observed around 2 Å in both datasets. We tentatively assign this to the sodium-carbon separation distance between the cluster and the host carbon framework.

4.4 Discussion

As discussed in chapter 3 the likely locations for sodium storage during the first electrochemical process are nearby defects. With the exception of some fullerenes, curvature in carbon comes about as a result of five or seven membered rings. Thus it is possible to use the curvature in our models as a measure of the defect concentration in the carbons. Given that the curvature is largely constant in each of our models, even when the fragment size increases, this suggests that the defect concentration reduces as the fragment size increases (fewer defects per unit volume). Thus if storage at defect sites is the prevailing mechanism at this stage of the electrochemistry, we expect the capacity during this process to correlate with the inverse of the fragment size. Our electrochemical measurements confirm this to be the case. The two carbons with the largest capacity during the sloping process consist of fragments with the fewest number of atoms — carbotron (121 $mA\,h\,g^{-1}$; 240 atoms) and 1100 °C (132 $mA\,h\,g^{-1}$; 204 atoms). The carbons with more atoms having a lower capacity on this process — Faradion (89 $mA\,h\,g^{-1}$; 340 atoms), and 1500 °C (89 $mA\,h\,g^{-1}$; 360 atoms).

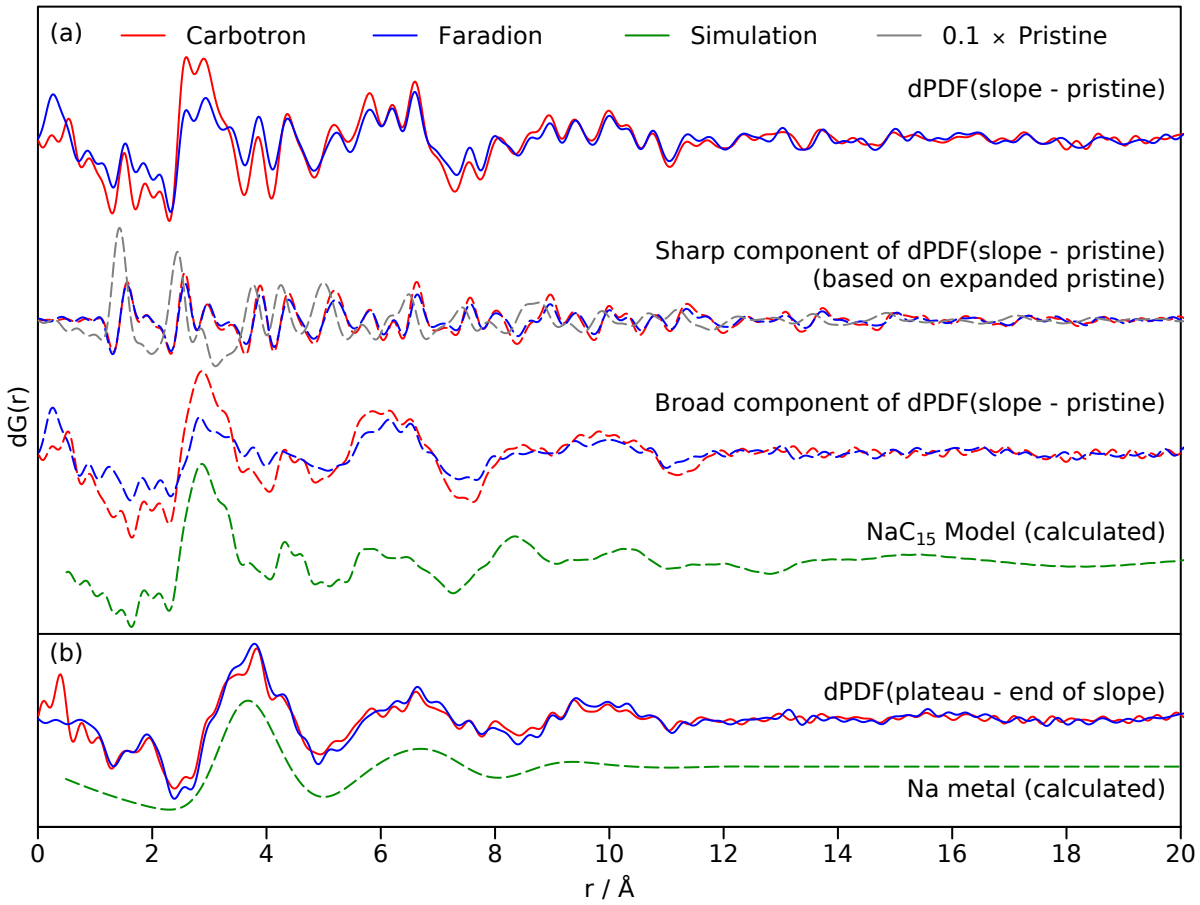

Figure 4.14: (a) Differential PDFs for carbotron (red) and Faradion (blue) for the end of slope process. The dashed red / blue lines represent the deconvolution into sharp (based on an expansion of the carbon matrix) and broad components. The dashed grey line shows the (scaled) PDF for pristine carbotron for comparison, and the dashed green line shows the calculated PDF for a NaC_{15} model (Figure 4.15). (b) Differential PDFs for the end of plateau process. The dashed green line shows the calculated PDF for sodium metal (with U_{iso} = 0.35; spherical particle diameter = 12.9 Å).

From our PDF data, it is clear that reaction occurs preferentially near the carbon atoms with the shortest bond lengths. This results in an expansion of the graphene sheets. This occurs at the same time as we observe a negatively shifted peak in our NMR data. This shift results from aromatic ring currents, and indicates that the sodium atoms are above the plane of the carbon rings. Combined, these observations suggest that the sodium atoms are interacting with the π orbitals that form part of the carbon bonding framework. An expansion of the carbon-carbon bond lengths could result from either a withdrawal of π bonding electron density, or the addition of electron density to the π antibonding orbitals. This is also consistent with the diamagnetic nature of the NMR shift implying the presence of Na^+ ions, which indicates that adding electron density to the π antibonding orbitals is the likely mechanism. It should be noted that this behaviour is not unique to sodium, similar effects having been observed during the intercalation of potassium into graphite, where a stage-III potassium graphite intercalation compound was found to have an average C-C bond expansion of 0.2%.[93]

During the second process, we observe that the carbons with the largest domain size exhibit

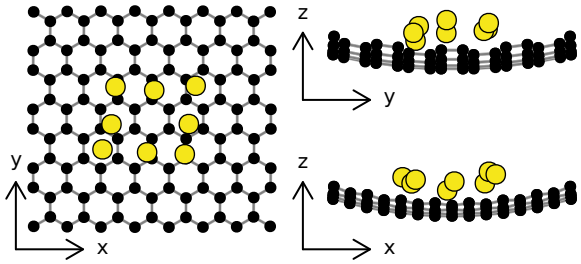

Figure 4.15: The structure of NaC_{15}, used as a preliminary model for the phase formed at the end of the sloping electrochemical process. Carbon atoms are shown in black, sodium in yellow.

the highest capacity. It has been previously been theorised that the mechanism for sodium storage during this process is either intercalation,[94] or sodium pooling within pores.[59] An increase in the domain size of the carbons would be expected to result in an increase in the number of regions accessible to intercalation, consistent with the observation of increased capacity with larger carbon sheets. We cannot assess the second mechanism so easily, however, as our models do not contain any pores given they consist only of a single "unit". To assess the possibility of the pooling mechanism, we consider the effect of increasing the number of atoms needed in the model to fit the experimental data. As the carbon domains increase in size, the structure is necessarily becoming more ordered. This could occur as a result of smaller fragments joining together, moving closer to each other, or of one fragment "donating" its atoms to allow another fragment to grow. Regardless of which mechanism occurs, they are all likely to result in the destruction of very small pores within the structure. The closing of smaller pores is likely to result in the formation of larger pores unless there is a significant change in the overall density of the material. Further work, in the form of small angle scattering measurements, is needed to verify this for these carbons, although it has been shown that the pore size increases with pyrolysis temperature for a range of similar carbons.[95] Thus the mechanism of sodium pooling is also likely consistent with the observed capacity trend. We therefore rely on our differential PDF data (Figure 4.14b) being a good match to a sodium metal cluster, with no strong, distinct carbon correlations, to suggest that sodium pooling is the more likely mechanism.

Interestingly, the differential PDFs obtained for the two carbons at the end of discharge are effectively identical (Figure 4.14b), whereas their NMR shifts vary by 200 ppm. This implies that the NMR shift does not correlate with the size of the sodium clusters, correlating instead with the size of the graphene fragments. Therefore, we propose that the likely origin of this shift is from reduction of the graphene sheets. The Na^+–C interaction becoming less ionic as the carbon is reduced, affecting the shifts of all sodium atoms in close proximity to the carbon. This effect increases in magnitude with the correlation length of the carbon.

4.5 Conclusions

We have synthesised a number of different hard carbons, varying the temperature of pyrolysis in order to generate different structures. By fitting PDF data using the simplest possible model that is able to explain the data well, we have been able to link the different synthesis conditions to different atomic structures. We then took the carbons synthesised at the highest temperatures, along with two commercial carbons, and performed electrochemical measurements in combination with *operando* PDF and NMR. We presented clear evidence for the expansion of the carbon-carbon bonds during the first process along with the formation of a new, sodium containing phase. We propose that this expansion is caused by the addition of electron density to the carbon π antibonding orbitals, and is most likely to occur near defects. We further demonstrate that the sodium inserted during the second process is likely in the form of sodium clusters, their PDFs being very similar to that of sodium metal.

4.5.1 Further Work

Further work is necessary to confirm the validity of the curvature modelling presented for the pristine carbons. Additional measurements using a complementary technique (e.g. transmission electron microscopy (TEM)) are necessary both to compare the magnitude of any observed curvature, as well as assessing the distribution of different structural motifs within the materials. Furthermore, expanding this work to additional carbons would assist in the understanding of synthesis-structure-property trends, eventually allowing for "designer" carbons. In terms of the sodium storage mechanism, additional modelling is necessary to identify the broad phase formed during the sloping electrochemical process. Moreover, quantifying the pore sizes within the carbons would help to confirm the suggested mechanism for the plateau process. Finally, expanding the *operando* analyses to a greater number of carbons will allow for the assessment of how much impact different carbon structures have on the mechanisms.

5 Investigating Discharge Mechanisms in Tin Anodes using PDF and SSNMR

Preface

The DFT and molecular dynamics (MD) calculations referenced here were performed by Dr Martin Mayo and Dr Andrew Morris. Many of the structures described in this chapter derive from these calculations; a brief summary may been found in section 5.3.1 and Figure 5.1a. Full details may be found in the following publication, whose text and figures are adapted here in order to describe the experimental results within this chapter:

Stratford, J. M.; Mayo, M.; Allan, P. K.; Pecher, O.; Borkiewicz, O. J.; Wiaderek, K. M.; Chapman, K. W.; Pickard, C. J.; Morris, A. J.; Grey, C. P. Investigating Sodium Storage Mechanisms in Tin Anodes: A Combined Pair Distribution Function Analysis, Density Functional Theory, and Solid-State NMR Approach. *Journal of the American Chemical Society* **2017**, *139*, 7273–7286

5.1 Introduction

Alloying materials, such as Sn, Sb, Ge and Pb, are of great interest because of their large gravimetric capacities: practical reversible capacities of 500, 580, 350 and 480 $\mathrm{mA\,h\,g^{-1}}$, respectively, have previously been reported over multiple cycles, with theoretical capacities even greater.[38,96,97] Tin shows a very high theoretical capacity of 847 $\mathrm{mA\,h\,g^{-1}}$ (based on complete conversion to $Na_{15}Sn_4$), and reported experimental capacities have been able to

approach this.[38,41] Furthermore, it has frequently been employed in binary systems, such as SnSb, CoSn and SnS, which can offer improved long-term performance.[39,98–101] Efforts to understand these more complex systems will be aided by a detailed understanding of the nature of sodium storage in the single-component tin system.

The electrochemical properties of the sodium–tin system were first investigated in 1920 when four NaSn alloys were discovered through electrochemical reactions in pyridine solutions, namely Na_4Sn, Na_2Sn, NaSn and $NaSn_2$.[102] Molten sodium batteries with tin counter-electrodes were investigated in the early 1990s, identifying three single-phase alloy regions and determining their approximate compositions.[103] A patent application in 2007 used tin as the anode in a full-cell configuration.[104] Recent intense interest in the sodium-tin electrochemical system began in 2011 when a theoretical voltage profile of Na-Sn was calculated by Chevrier *et al.* using known crystal structures from the Inorganic Crystal Structure Database (ICSD),[105] including $NaSn_5$, NaSn, Na_9Sn_4 and $Na_{15}Sn_4$.[43] A subsequent experimental work presented a galvanostatic electrochemical profile with four distinguishable plateaus, which were assigned to the mechanism proposed by Chevrier *et al.* although there was a large discrepancy between the calculated and experimental results.[38] Ellis *et al.* proposed a slightly different mechanism for the first plateau, where a composition of $NaSn_3$ was determined by coulometry.[106] The authors were the first to identify the formation of an amorphous species of approximate composition NaSn, and also demonstrate the formation of additional crystalline intermediates but, with the exception of $Na_{15}Sn_4$, their diffraction patterns do not match those of any known structures for these phases. An *operando* TEM study of tin nanoparticles suggested a different phase transformation: a first step two-phase reaction from pristine Sn to amorphous $NaSn_2$, followed by single-phase reactions resulting in amorphous Na_9Sn_4 and Na_3Sn phases, and finally a crystalline $Na_{15}Sn_4$ phase.[107] It should be noted that significant differences in the experimental setup used in the TEM study, such as a solid NaOH + Na_2O electrolyte in place of a conventional liquid electrolyte and the use of potential rather than current control, could have an effect on the observed sodium insertion mechanism.[108] Work by Baggetto *et al.* on tin thin films showed a more complex form of the electrochemical potential profile.[41] The first process around 0.4 V was shown to be composed of two processes on discharge, but only a single process on charge. Their experimental work was accompanied by a DFT calculation of theoretical voltages using the known Na-Sn phases and metastable phases generated using the cluster-expansion method. Using XRD, they furthered previous analysis by assigning the DFT calculated Na_5Sn_2-$R\bar{3}m$ (where $R\bar{3}m$ refers to the space group, specified here to distinguish between different possible polymorphs) structure to the phase formed at the end of the third process. In a more recent study, the same group performed a reinvestigation of Na_xSn phases with $x \geq 1$.[109] The XRD pattern of a phase synthesised by solid-state reaction methods matched Na_7Sn_3-$R\bar{3}m$, a defect variant of the Li_5Sn_2-$R\bar{3}m$ structure with sodium substituted for lithium; therefore it was postulated that this, not Na_5Sn_2, is the product of the electrochemical reaction with tin. The authors proposed that Na_7Sn_3 formed at the expense of the thermodynamically-stable Na_9Sn_4-$Cmcm$ phase due to its slow formation kinetics.

Clearly, there remain significant gaps in understanding of the phases formed during sodium insertion. In the following, we present an investigation into these phases using a combination

of structure prediction and experiment. *Operando* measurements circumvent problems associated with sample degradation, which can complicate the interpretation of *ex situ* data, and can additionally observe metastable intermediates that may be subject to relaxation effects during post-mortem analysis. We use *operando* XRD, PDF analysis and ssNMR to probe both local structure and longer-range in order to analyse the structure of the phases formed. In particular, the following questions are addressed: (i) the number and nature of the crystalline phase(s) formed during the first electrochemical process, about which little is known; (ii) the structural features of the amorphous phase formed during the second electrochemical process; (iii) the phase formed during the third process, where there remains a lack of consensus within the literature; Na_9Sn_4, Na_7Sn_3 and Na_3Sn, have all been suggested as potential candidates.

5.2 Experimental

Except were otherwise stated, all experiments were performed under ambient conditions.

5.2.1 Electrode Preparation

Tin powder (Sigma Aldrich, ≥99%, particle size ≤150 nm), carbon Super P (Timcal) and sodium carboxymethyl cellulose (Sigma Aldrich, DS = 0.7, MW = 700,000) (70:19:11) were ball-milled in a water:ethanol solvent (70:30) using a SPEX 8000M Mixer / Mill for 15 minutes. The resulting viscous slurry was cast onto Mylar foil using a 300 µm doctor blade, dried for 16 hours in air, and then a further 4 hours at 100 °C in vacuo. The resultant self-supporting films were used for all the electrochemical measurements reported here.

5.2.2 Electrochemical experiments

Cells were prepared under an argon atmosphere using metallic sodium (Sigma Aldrich, 99.9%) as an anode. The electrolyte was 1 M $NaPF_6$ (Alfa Aesar, ≥99%) in propylene carbonate (Sigma Aldrich, anhydrous), and the separator was borosilicate glass fibre (Whatman, GF/A). *Ex situ* electrochemical measurements were performed with standard 2032 coin cell parts using a Biologic MPG2 battery cycler.

Whilst commercial electrodes are usually fabricated by casting a slurry onto a metallic current collector (typically aluminium for NIBs), the presence of such a current collector does not allow *operando* PDF and NMR measurements to be performed. In the case of PDF, the inhomogeneity caused by rolling the metal foil causes inconsistencies in the background depending upon where the beam hits. For NMR the metal foil shields the RF radiation, attenuating the signal. As such, all reported electrochemical data in this chapter was performed using the self-supporting films described above. In order to maximize signal-to-noise for our

measurements, films of greater thickness than are often used in electrochemistry measurements were also used (typically around 300 µm). Such films, if optimised are, in principle, of commercial relevance as they maximize the energy density that can be obtained without using large quantities of an expensive current collector. Increasing the thickness necessitated a corresponding increase in the temperature at which the cells were cycled in order to achieve an acceptable rate performance. We note no significant differences to the features observed in reported electrochemical measurements as a result of these changes, aside from additional capacity above 0.5 V, which we attribute to a combination of SnO on the surface of the nanoparticles, and additional electrolyte breakdown as a result of the large surface area exposed.

5.2.3 PDF Analysis

Operando PDF measurements were performed at beamline I15 at Diamond Light Source using a modified Swagelok cell adapted for X-ray transmission (Figure 2.4c on page 10). Cells were prepared in an argon atmosphere glovebox (O_2, $H_2O < 0.1$ ppm) using the same materials as for the coin cell measurements. Electrochemical measurements were performed using an Ivium-n-Stat battery cycler. Cells were galvanostatically cycled in the potential range 2–0.001 V at a rate of C/30 (based on the mass of tin, corresponding to 3.75 Na per Sn in 30 hours) and held at the end of discharge for the remainder of the experiment (a further 32 hours).

Measurements were taken using an X-ray beam of energy 76 keV ($\lambda = 0.1631$ Å) and an amorphous silicon area detector (Perkin Elmer) in order to gather data to large values of momentum transfer.[110,111] Data were collected at 60 minute intervals, using a total exposure time of 60 s per scan.

Additional *operando* PDF and XRD measurements were performed at beamline 11-ID-B at the Advanced Photon Source, Argonne National Laboratory using the AMPIX cell (Figure 2.4b on page 10).[53] Cells were prepared in an argon atmosphere glovebox (O_2, $H_2O < 0.1$ ppm) using the same materials as for the coin cell measurements. Electrochemical measurements were performed using a Maccor 4300 battery cycler. Cells were galvanostatically cycled in the potential range 2–0.001 V at a rate of C/70 (based on the mass of tin, corresponding to 3.75 Na per Sn in 70 hours).

Measurements were taken using an X-ray beam of energy 86.7 keV ($\lambda = 0.1430$ Å) and an amorphous silicon area detector (Perkin Elmer) in order to gather data to large values of momentum transfer.[110,111] Data were collected at 60 minute intervals, alternating diffraction mode and PDF mode using an exposure time of 300 s at a temperature of 60 °C.

For all PDF and XRD experiments, background measurements were taken using identical cells, but without the active material present. A CeO_2 standard was used to determine the sample geometry and the sample-to-detector distance. The data were converted to a function of intensity vs. Q using FIT2D or DAWN.[65,112] Standard corrections (background, Compton scattering, detector effects) were applied, and the data Fourier transformed to obtain $G(r)$

using the software PDFGetX2.[66] Structural refinements were performed on the crystalline components using PDFGUI.[67]

Reverse Monte Carlo Refinements

RMC refinements were performed using RMCProfile.[113] We used a 10×10×10 supercell of an amorphous phase generated using *ab initio* MD as the starting model, which was refined against real- and reciprocal-space data simultaneously. The minimum distance was set to 2.63 Å, which is the observed minimum distance in the experimental PDF. The number density was set to 0.0325, which is the same as the starting model. The maximum distance for an individual movement was set to 0.05 Å. The refinement was stopped when no further improvement to the fit was observed.

Following the RMC refinements, real-space least-squares refinements were performed in PDFGUI.[67] As a starting model, a 61 atom subcell of the RMC refined $Na_{1.18}Sn$ was used with a spherical particle diameter of 40 Å, and $NaSn_2$ was used to account for the longer-range correlations. U_{iso} parameters for all atoms were set to an initial value of 0.01. Unit cell parameters, phase scale factor, $delta_1$ (low-r peak sharpening parameter) and the thermal parameters for both Na and Sn were all refined, along with the Sn atomic positions. Q_{damp} (instrument resolution parameter) was set to the value obtained from a refinement of the pristine material. For $NaSn_2$, $U_{33,Sn}$ was refined independently of U_{11} and U_{22} (which were constrained to be the same), this was not possible for Na. For $Na_{1.18}Sn$ the thermal displacement parameters were considered isotropically.

5.2.4 Solid-State NMR Spectroscopy

In-house designed cells based upon a cylindrical capsule (Figure 2.4d on page 10) were prepared in an argon atmosphere glovebox (O_2, $H_2O < 0.1$ ppm) using the same materials as for the coin cell measurements. Electrochemical measurements were performed using a Bio-Logic VSP battery cycler. Cells were galvanostatically cycled in the potential range 2–0.001 V at a rate of C/30 (based on the mass of tin, corresponding to 3.75 Na per Sn in 30 hours), and held at 1 mV until the applied current dropped to C/100, which ensures complete reaction of the electrode materials (a process commonly required for *operando* measurements, where there is an increased resistance of the electrochemical cell caused by modifications to allow external monitoring).[114] Cells were cycled at a temperature of 35 °C.

Operando SSNMR measurements were performed using a Bruker Avance 300 MHz spectrometer (^{23}Na Larmor frequency = 79.39 MHz). It was observed that the formation of intermetallic species during operation of the batteries radically changed the required tuning and matching parameters. Using a conventional static probe, with a resonance circuit fixed at the start of the experiment, thus resulted in a reduction in the quality of data gathered as the properties of the electrodes changed. In order to overcome these difficulties, a static

probe system with automatic tuning and matching capabilities (along with connections for an external battery cycler) was used.[68] The resonance circuit was recalibrated immediately prior to each measurement by minimising the standing wave ratio of the forward and reflected power for a low power (0.01 W) continuous wave pulse. The electrochemical cell was aligned such that the electrodes were perpendicular to the applied field.

In order to maximise the signal-to-noise ratio for a time-restricted measurement, a one-pulse sequence was used. A 90° pulse corresponded to 4.5 µs at 200 W using an 11 mm diameter silver coil. 25600 transients were collected for each spectrum, using a recycle delay of 0.05 s (30 minutes per spectrum). The ^{23}Na signals were referenced using a 1 M solution of NaCl at a shift of 0 ppm.[69] Spectra were Fourier transformed and individually phased using Bruker Topspin 3.2. Backgrounds were subtracted using fityk.[70] *Ex situ* ^{23}Na MAS ssNMR measurements were performed using a Bruker Avance III 200 MHz spectrometer (^{23}Na and ^{119}Sn Larmor frequencies of 52.92 and 74.61 MHz respectively). 1.3 mm zirconia rotors were spun at 60 kHz using a Bruker double resonance probehead. For the ^{23}Na measurements, a MAS speed synchronised Hahn-echo pulse sequence with 90–180° pulses corresponding to 2–4 µs at 25 W was applied and a recycle delay of 0.05 s was used. Spectra were referenced using NaCl powder at 7.21 ppm.[71] For the ^{119}Sn measurements, a Hahn-echo pulse sequence with 90–180° pulses corresponding to 1.38–2.76 µs at 43.5 W was applied and a recycle delay of 0.3 s was used. Spectra were referenced using SnO_2 powder at −604.3 ppm.[115]

Samples for *ex situ* MAS ssNMR investigations were prepared electrochemically; cells were cycled at a rate of C/20 (based on the mass of tin, corresponding to 3.75 Na per Sn in 20 hours) to the point of interest on the electrochemical curve at a temperature of 55 °C. The electrodes were recovered inside an argon atmosphere glovebox (O_2, H_2O < 0.1 ppm), washed with dimethylcarbonate (Sigma Aldrich, anhydrous, >99%) and immediately dried in vacuo. The respective electrode films were then individually ground and packed into rotors immediately. Decomposition was minimised by careful and rapid handling of the materials within a glovebox. However, the samples were found to degrade in under 5 minutes of exposure to the glovebox atmosphere, so it is possible that small quantities of decomposition products remain.

5.3 Results

5.3.1 Theory Overview

In Figure 5.1a, a plot of formation enthalpy as a function of sodium concentration for the structures obtained by *ab initio* random structure searching (AIRSS) and a swapping species method is presented. The convex hull shows three stable structures with a sodium content ≤ $Na_{0.5}Sn$: $NaSn_5$,[116] Na_5Sn_8[117] and a $NaSn_2$-$P6/mmm$, structure obtained by AIRSS. The predicted $NaSn_2$-$P6/mmm$ structure has a formation energy 0.015 eV/atom lower than the experimentally known $NaSn_2$-$C2/m$ Zintl phase.[118] Moving to higher concentrations, Na_1Sn_1-$I4_1/acd$ is the only stable phase found in Na_xSn 0.5 < x < 2. Beyond this (Na_2Sn to

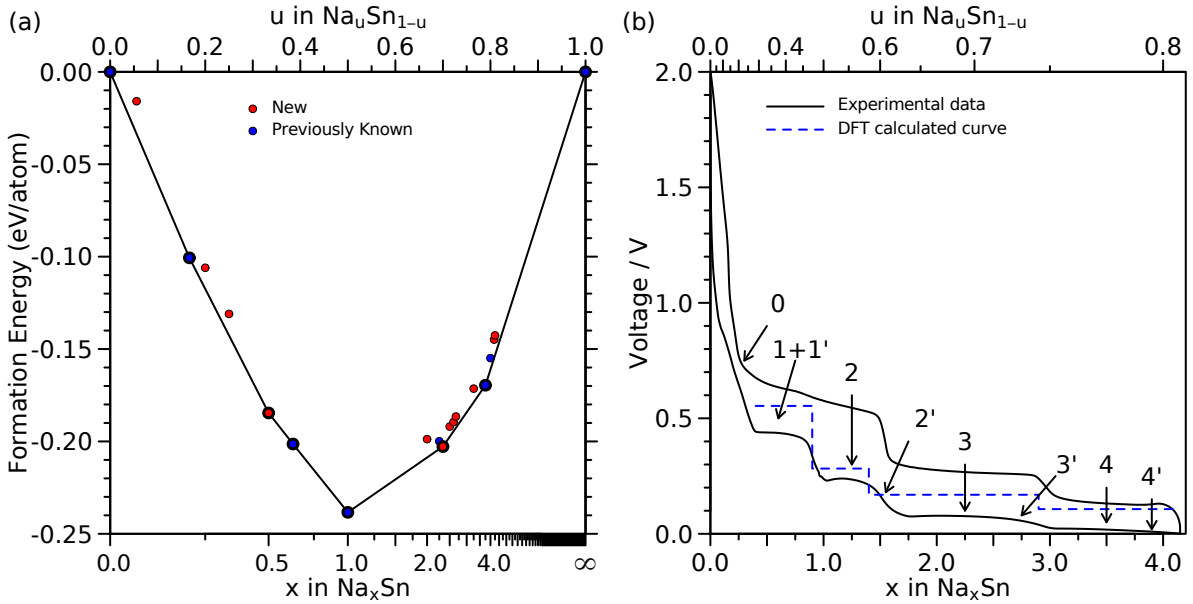

Figure 5.1: (a) Formation enthalpy per atom vs the fractional sodium concentration in the Na-Sn compound. The convex hull (tie-line) is constructed by joining the stable structures obtained by the searches. Only the lowest energy structure for each composition within 0.02 eV/atom of the convex hull is shown. (b) Electrochemistry data for a sodium–tin cell cycled at a rate of C/20 (corresponding to achieving a capacity of 847 mA h g^{-1} in 20 hours) between 2 and 0.001 V (black line). Observed electrochemical processes are indicated with arrows. Average potentials relative to sodium metal calculated by DFT are shown as a blue line for the structures which best fit the experimental observations (namely $NaSn_2$, *a*-NaSn, Na_5Sn_2 and $Na_{15}Sn_4$). The theoretical profile is aligned with the experimental profile (removing process "0") such that it starts with process 1. Experimental data are normalized (to allow ready comparison with theory) such that 3.75 Na are inserted (and removed) during processes 1 through 4′.

$Na_{3.5}Sn$), the structures exhibit Sn-Sn dumbbells. DFT calculations predict that the Na_7Sn_3 phase, obtained by swapping species from Li_7Si_3-$P3_212$, is stable whereas the experimentally reported Na_9Sn_4[119] phase is found 4 meV/atom above the convex hull tie-line. The lowest sodium content structure in this region is a metastable Na_2Sn-$P2_1/c$ AIRSS structure. The structure is formed of non-collinear Sn-Sn dumbbells. The Na_7Sn_3 and Na_9Sn_4 structures mentioned above are found on increasing in sodium further, followed by Na_5Sn_2, $Na_{13}Sn_5$, Na_8Sn_3 and $Na_{13}Sn_4$. All these metastable structures are very close to the tie line of the convex hull construction. The concentration of Sn-Sn dumbbells in Na_2Sn, Na_9Sn_4, Na_7Sn_3 and Na_5Sn_2 is gradually lowered as Na concentration is increased, forming a mixture of Sn-Sn dumbbells and isolated atoms in $Na_{13}Sn_5$, Na_8Sn_3 and $Na_{13}Sn_4$. At the highest sodium concentrations (>$Na_{3.5}Sn$) we find the stable $Na_{15}Sn_4$-$I\bar{4}3d$ phase, which consists of isolated Sn atoms. In the following sections, our experimental data is interpreted in the context of the phases shown on this hull.

5.3.2 Electrochemical Results

Figure 5.1b shows the experimental galvanostatic electrochemical profile obtained at a rate of C/20 and a temperature of 55 °C. In agreement with previous reports, we observe multiple electrochemical processes; we denote these as processes 0, 1, 2, 3, and 4, and these names will be used throughout the subsequent text. We also note that there are sloping regions towards the end of processes 2, 3 and 4, which account for a significant fraction of the capacity at these potentials. We refer to these as 2′, 3′ and 4′, respectively. The reasons underlying these distinctions will be discussed in the following sections. In addition, Baggetto *et al.* note the possibility that the first electrochemical process on discharge (around 450 mV) may in fact be two distinct processes;[41] we refer to these as processes 1 followed by 1′.

5.3.3 Overview of *Operando* Results

Operando PDF data, obtained by the Fourier transformation of X-ray total scattering data, are shown in Figure 5.2a. It is apparent that the pristine material (β-Sn) initially undergoes very little change (electrochemical process 0), which is followed by a transformation of β-Sn into one or more crystalline phases, with correlations extending beyond 50 Å (electrochemical processes 1 and 1′. The loss of extended connectivity during electrochemical processes 2 and 2′ is clear, with no major correlations found beyond 20 Å in this region. Finally, a return to long-range ordering is observed throughout the remaining electrochemical processes. In addition, it is clear that the sharp Sn-Sn nearest-neighbour peak, at approximately 3 Å, is not observed to change significantly during processes 0 through 3′.

Figure 5.2b shows the *operando* ^{23}Na NMR spectra obtained during the first discharge. Peaks at −10 ppm and 1140 ppm are observed throughout the measurement, including in the spectrum of the as-assembled electrochemical cell, and correspond to the $NaPF_6$ electrolyte and the sodium metal counter electrode, respectively. During electrochemical processes 1 and 1′, we observe the growth of a weak peak with a maximum at 620 ppm. This signal disappears, and a new resonance is observed at 50 ppm during process 2. Throughout process 2′, the peak at 50 ppm broadens and shifts to 75 ppm; it then shrinks as a further sodium environment is formed with a peak at a shift of 202 ppm, which corresponds to the phase formed during the third electrochemical process. The sloping region of the electrochemistry that follows, i.e. process 3′, sees this resonance shift gradually to 180 ppm. The final processes during discharge (processes 4 and 4′) result in the appearance of two additional sodium environments. We see a very broad resonance with maximum around −75 ppm, and a further peak with maximum around −260 ppm which appears later. The majority of the resonances observed have a shift whose magnitude is greater than 100 ppm; this is ascribed to the Knight shift, which is caused by the interaction of unpaired electrons at the Fermi level of the conduction band interacting with the nuclear spins — see section 2.3 on page 25 for further details.[78] The shift is a measure of the density of states at the Fermi level at the Na nucleus, and is indicative of metallic character of the material.

We now discuss the *operando* PDF and NMR results, in conjunction with additional *operando*

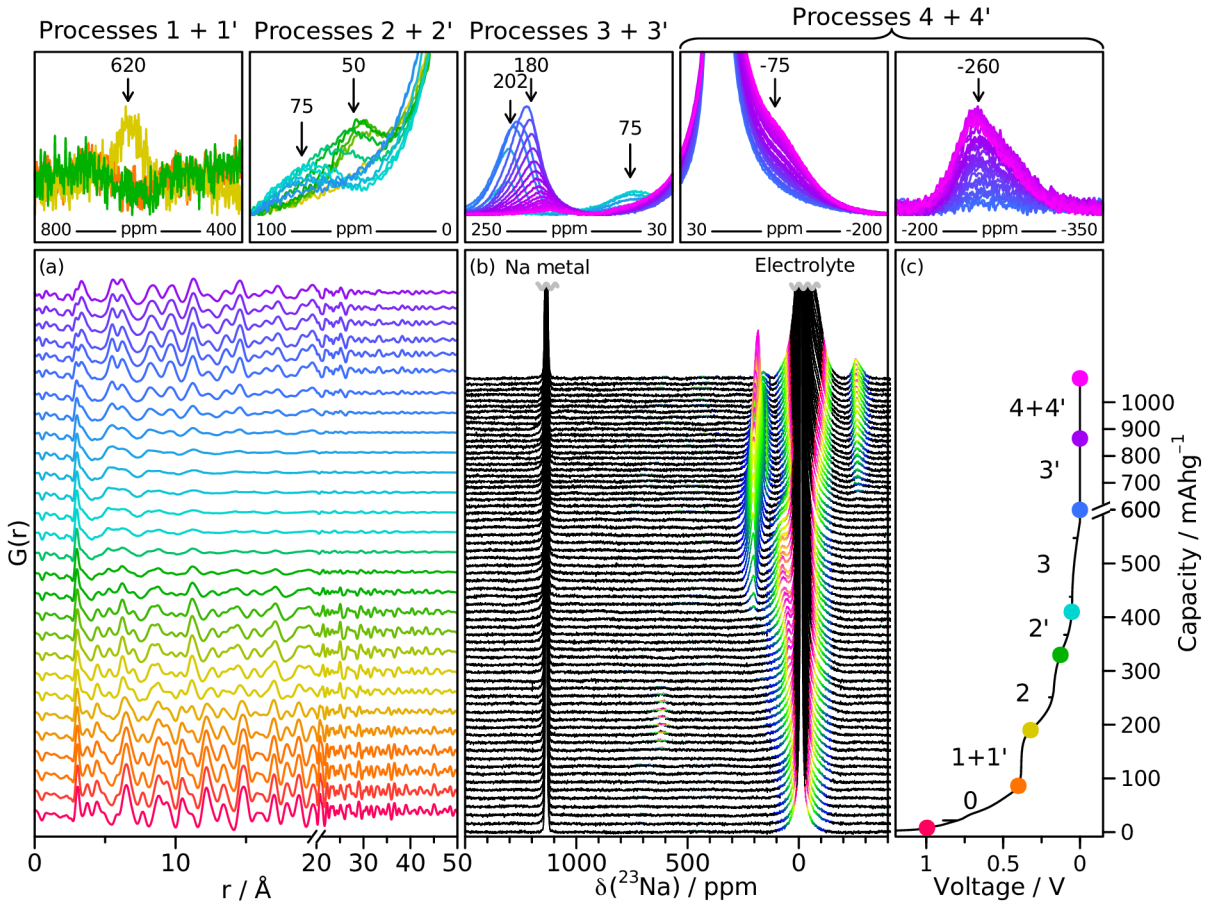

Figure 5.2: *Operando* measurements for electrochemical cells with sodium metal and tin electrodes, and a $NaPF_6$ electrolyte. (a) Selected PDFs obtained during the first discharge are vertically offset in time; the colours correspond to the points shown on the electrochemical curve. (b) ^{23}Na NMR spectra obtained during the first discharge, aligned with the corresponding electrochemistry (c). Strong features corresponding largely to the electrolyte or metal have been truncated for clarity. Spectra are coloured in the region −500–1000 ppm according to their intensity. Selected regions are highlighted above, where the colours now correspond to the points shown on the electrochemical curve. The cells were cycled at a rate of C/30 (corresponding to achieving a capacity of 847 mA h g^{-1} in 30 hours) between 2–0.001 V, and held at the end of discharge until the current dropped to below C/100.

XRD data together for each distinct electrochemical process, from 0 through to 4′.

5.3.4 Process 0

A slope from 1.4 V to around 0.5 V is observed in the electrochemistry. No significant capacity has been reported as a result of sodium–tin alloying reactions at these potentials. We, thus, attribute this capacity to three factors that do not involve Sn (hence our naming of this process as process 0): electrolyte decomposition to form a SEI layer, and sodium storage within the carbon additive are both commonly observed at these potentials.[24,25] In addition, *operando* XRD data for the pristine material indicates small amounts of SnO and SnO_2 are present in addition to β-Sn (Figure 5.3). During this period of the electrochemistry, our

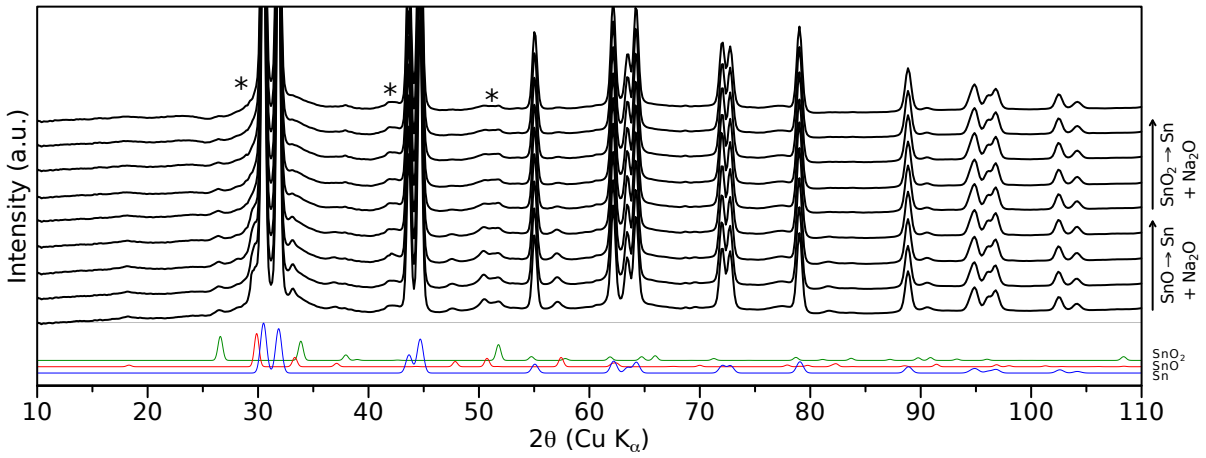

Figure 5.3: Diffraction patterns obtained during an *operando* experiment from the start of discharge until the end of the electrochemical process 0. Calculated patterns are shown for Sn (blue), SnO (red) and SnO_2 (green). Trace amounts of sodium from the cell background are indicated with an asterisk (∗). The cell was cycled at a rate of C/70 (corresponding to achieving the theoretical capacity in 70 hours) and data were gathered at 2 hour intervals. Data were gathered using X-rays of wavelength 0.1430 Å and converted to Cu K_α (1.54 Å).

diffraction data indicates that SnO and SnO_2 convert sequentially into Sn metal. Na_2O is also expected to form, but the low concentration compared with the bulk β-Sn, along with the much smaller X-ray structure factors of Na and O compared with Sn meant that we were unable to detect this. These reactions have previously been observed to result in a sloping electrochemical curve starting at 1 and 0.8 V respectively, and ending around 0.5 V in both cases.[120,121] As these reactions result in the formation of β-Sn, the material that we are investigating, the presence of these side-reactions prior to the reaction of tin metal is highly unlikely to impact our subsequent results.

^{23}Na *operando* ssNMR measurements during this process show no significant changes. This is consistent with forming very small amounts of Na_2O ($\delta = 55.1$ ppm[122]), which would give a signal too weak to show above the noise. Refinements of PDF data during this process indicate an increasingly good match to β-Sn (Table 5.1), consistent with the loss of the impurity oxide phases. Refinements were not made with either of the oxides as secondary phases owing to the very small concentrations observed in the Bragg diffraction data.

5.3.5 Processes 1 and 1′

The next feature in the electrochemistry is observed at approximately 450 mV *vs.* Na metal and appears as a flat plateau. During this step, intensity of the peaks associated with initial Sn in the XRD/PDF patterns progressively decrease, and peaks from a new phase start to appear (Figure 5.2a). PDF and diffraction data for the phase remaining at the end of this process provide an excellent match to the layered ($P6/mmm$) $NaSn_2$ structure (Figures 5.4b and 5.6d). This structure consists of honeycomb-like layers of tin separated by layers of sodium, whose atoms sit at the centre of the tin hexagons (Figure 5.4b and c). To the best of our knowledge, this structure has not previously been experimentally observed. It should

Table 5.1: Real-space least-squares refinements against PDF data were performed in PDFGUI.[67] A starting model of β-Sn was used. Thermal displacement parameters, U_{iso}, for all atoms were set to an initial value of 0.01. Unit cell parameters, phase scale factor, $delta_1$ (low-r peak sharpening parameter) and the thermal parameters were all refined. Q_{damp} (instrument resolution parameter) was set to the value obtained from a refinement of the pristine material. An increasingly good fit (as indicating by a decreasing R_w) is consistent with the removal of impurity oxide phases.

Capacity / mA h g^{-1}	a / Å	c / Å	U_{iso}	R_w
6.00	5.838	3.186	0.027	0.153
17.6	5.839	3.187	0.027	0.144
29.6	5.838	3.187	0.027	0.137
41.3	5.838	3.186	0.027	0.129
52.9	5.838	3.186	0.027	0.128
64.9	5.838	3.187	0.027	0.127
76.5	5.838	3.187	0.027	0.139
88.6	5.838	3.187	0.027	0.129
100.2	5.837	3.186	0.028	0.130
111.8	5.837	3.186	0.029	0.139
123.9	5.838	3.186	0.028	0.141
135.5	5.838	3.186	0.028	0.154
147.1	5.838	3.186	0.029	0.171
159.1	5.838	3.185	0.031	0.177
170.8	5.838	3.183	0.034	0.169
182.8	5.836	3.184	0.021	0.150
194.4	3.839	3.186	0.029	0.122
206.1	5.838	3.186	0.027	0.129

be noted that, whilst a diffraction pattern for the pure $NaSn_2$ phase has not been previously reported, patterns showing reflections consistent with this phase, along with one or more additional phases, have. A model has yet to be presented that explains these data.[41,106]

^{23}Na *operando* NMR measurements reveal a single peak with a shift of approximately 620 ppm, whose shift does not vary during this electrochemical process. This highly Knight shifted peak indicates a non-zero density of states at the Sn nuclei, consistent with metallic properties of this material and the extended tin structure. This is similar to the observed Knight shift for graphite intercalation compounds, whose structures show a good deal of similarity to $NaSn_2$.[123]

There is some debate in the literature as to whether a second, overlapping, plateau may also be present at a similar potential.[41] This is based upon electrochemical measurements of very thin films, and is not resolvable in our electrochemical data. In order to investigate

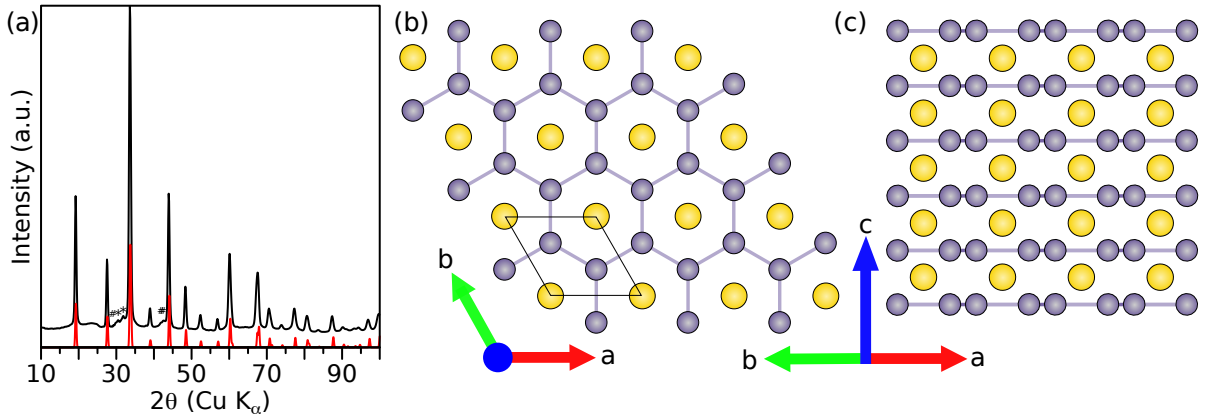

Figure 5.4: (a) A conventional powder diffraction pattern showing the intermediate formed at the end of process 1′ on discharge along with the calculated pattern for $NaSn_2$ (red). Trace amounts of Na and Sn are indicated by # and ∗ respectively. Data were gathered using X-rays of wavelength 0.1430 Å and converted to Cu K_α (1.54 Å). (b) A projection of the $NaSn_2$ structure viewed down the *c*-axis; (c) A projection of the $NaSn_2$ structure viewed down the (110) plane; sodium atoms are shown in yellow, tin in grey.

more closely whether it is possible to isolate two distinct phases forming in this region, we performed a second *operando* measurement. To increase the number of data points acquired, a cell was cycled considerably more slowly (a rate of C/70 was used) and data suitable for PDF analysis and higher resolution diffraction data were gathered alternately (either PDF or XRD once every hour). Bragg reflections corresponding to Sn decrease in intensity in this region as sodium is inserted, whilst reflections corresponding to a further two phases grow. It is unclear whether the two phases appear sequentially or concurrently, however, at the end of this region of the electrochemistry, only one — $NaSn_2$ — remains (Figure 5.5). Our diffraction data are, therefore, in agreement with the observation of two conjugated plateaus.

The PDF data obtained during these processes (which we now distinguish as process 1 followed by 1′) can be modelled simply as a combination of Sn (whose Bragg reflections are clearly observed in our diffraction data until the end of these two processes) and $NaSn_2$ at all points (Table 5.2 and Figure 5.6). This suggests that any additional intermediate must be structurally related to either Sn or $NaSn_2$, or is only present in very small concentrations. However, these two phases alone are not sufficient to reproduce the Bragg reflections observed (Figure 5.7b). In particular, the reflections at 16.4, 28.5, 38.0, and 40.8°, along with further peaks at higher angles, cannot be derived from the $NaSn_2$-$P6/mmm$ structure.

The additional reflections are consistent with a structure similar to $NaSn_2$, retaining the honeycomb-like tin layers, but with a reduction in symmetry resulting from the loss of the 6-fold rotation axis. As this phase is formed prior to $NaSn_2$, it must have a lower sodium content. We, therefore, generated lower symmetry structures solely through careful placement of the sodium atoms between the tin layers. However, all such structures we tried were unable to produce any significant intensity for the additional reflections. Intensity for these reflections can only be generated through changes to the tin structure.

It is clear from the PDF that there is no significant deviation from the honeycomb-like tin

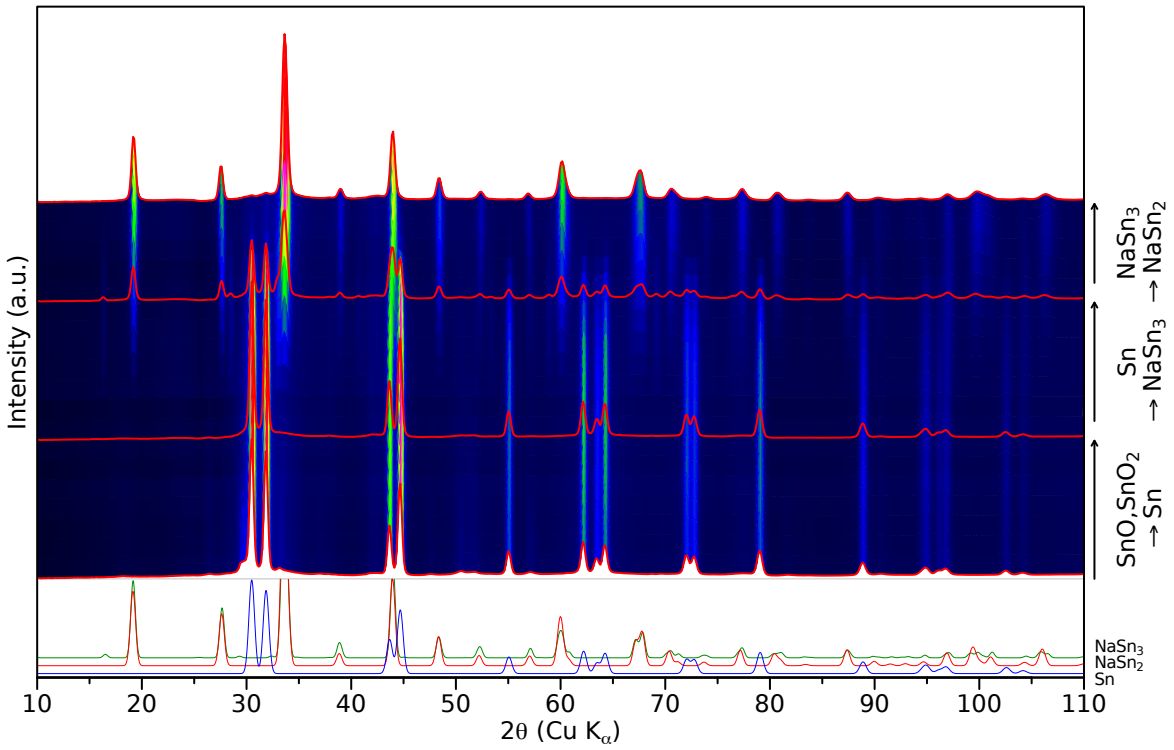

Figure 5.5: Diffraction patterns obtained during an *operando* experiment from the start of discharge until the end of the electrochemical processes 1 and 1′. Key frames are highlighted by solid red lines. Calculated patterns are shown for Sn (blue), $NaSn_3$ (green) and $NaSn_2$ (red). The cell was cycled at a rate of C/70 (corresponding to achieving the theoretical capacity in 70 hours) and data were gathered at 2 hour intervals. Data were gathered using X-rays of wavelength 0.1430 Å and converted to Cu K_α (1.54 Å).

layers, we therefore tested a model in which tin partially occupies sites within the sodium layers. It is possible to account for the lowered symmetry by replacing every other sodium atom in the $NaSn_2$ structure with a mixed $Na_{0.5}Sn_{0.5}$ occupancy in a *Pmmm* configuration (Figure 5.7a). This results in a stoichiometry of $NaSn_3$, which is consistent with that expected from the electrochemistry, and with a previous study using coulometry.[106] Although this structure does contain the additional reflections in the diffraction pattern, there remain minor differences in intensity (Figure 5.7b). This may be an artefact of the experimental setup (e.g. preferred orientation effects). In order to assess the stability of this structure, we generated a Na_4Sn_8 supercell of $NaSn_2$-*P*6/*mmm* in which we exchanged one sodium atom for a tin atom to give a stoichiometry of $NaSn_3$ (Na_3Sn_9). This phase was relaxed using the same DFT level of theory as used in the convex hull construction. The resulting $NaSn_3$-*Pmmm* structure was converged without any major ionic rearrangement and is found at only 0.007 eV/atom from the convex hull tie-line.

Whilst the *operando* ^{23}Na SSNMR measurement (Figure 5.2b) revealed a single peak, higher resolution measurements using *ex situ* ^{23}Na MAS SSNMR (Figure 5.7c) contained an additional asymmetrical broad feature with a maximum around 420 ppm. This signal could not be observed in the static *operando* measurement, the additional line broadening caused by the lack of MAS presumably leading to a broad feature that disappears into the baseline.

Table 5.2: Real-space least-squares refinements against PDF data were performed in PDFGUI.[67] A starting model of β-Sn and $NaSn_2$ was used. Thermal displacement parameters, U_{iso}, for all atoms were set to an initial value of 0.01. Unit cell parameters, phase scale factor, $delta_1$ (low-r peak sharpening parameter) and the thermal parameters were all refined. U_{33} was refined independently of U_{11} and U_{22} (which were constrained to be the same). Q_{damp} (instrument resolution parameter) was set to the value obtained from a refinement of the pristine material. In all cases a R_w of less than 0.20 indicates a good match to the experimental data. This means that the intermediate formed during process 1′ must be very structurally similar to either β-Sn or $NaSn_2$. The change in the lattice parameters for $NaSn_2$ during process 1 (after approximately 150 mA h g^{-1}) is due to the conversion from $NaSn_3$ to $NaSn_2$. $NaSn_3$ is not included in the model, however, the relatively high values of U_{33} for Sn towards the start of these processes are consistent with tin not solely being confined to planar layers.

	Sn			$NaSn_2$						
Capacity / mA h g^{-1}	a / Å	c / Å	U_{iso}	a / Å	c / Å	U_{Na}	$U_{33,Na}$	U_{Sn}	$U_{33,Sn}$	R_w
100.2	5.837	3.186	0.028	5.342	3.182	0.010	0.010	0.020	0.035	0.130
111.8	5.837	3.186	0.029	5.346	3.186	0.009	0.025	0.017	0.025	0.139
123.9	5.838	3.186	0.028	5.350	3.182	0.105	0.003	0.035	0.186	0.141
135.5	5.838	3.186	0.028	5.343	3.192	0.090	0.047	0.031	0.099	0.154
147.1	5.838	3.186	0.029	5.333	3.203	0.056	0.054	0.025	0.082	0.171
159.1	5.838	3.185	0.031	5.328	3.208	0.047	0.054	0.022	0.064	0.177
170.8	5.838	3.183	0.034	5.324	3.211	0.043	0.055	0.020	0.057	0.169
182.8	5.836	3.184	0.021	5.320	3.213	0.054	0.075	0.020	0.060	0.150
194.4	3.839	3.186	0.029	5.316	3.217	0.040	0.056	0.018	0.055	0.122
206.1	5.838	3.186	0.027	5.315	3.220	0.051	0.077	0.019	0.058	0.129

An additional sharp peak at 610 ppm emerges following further sodium insertion. *Ex situ* ^{119}Sn MAS SSNMR spectra (Figure 5.7d) show a sharp peak at 6890 ppm corresponding to residual Sn metal and a broad resonance centred around 6600 ppm. With higher sodium content, a sharp peak at 6275 ppm emerges. The sharp resonance in spectra of both nuclei is assigned to the $NaSn_2$ structure; the broad features reduce in intensity towards the end of the processes and are consistent with disordered sodium and tin atoms between the more ordered honeycomb-like tin layers in the phases with stoichiometry close to $NaSn_3$.

Therefore, we tentatively assign the first electrochemical process (1) to the formation of a phase similar to $NaSn_2$ of approximate composition $NaSn_3$, consisting of tin layers separated by disordered layers of mixed sodium and tin occupancy. Following this, $NaSn_2$-$P6/mmm$ forms during process 1′. Owing to the similarity of the structures formed, it is possible that process 1′ begins before process 1 has gone to completion as a result of an overpotential within the electrochemical cells.

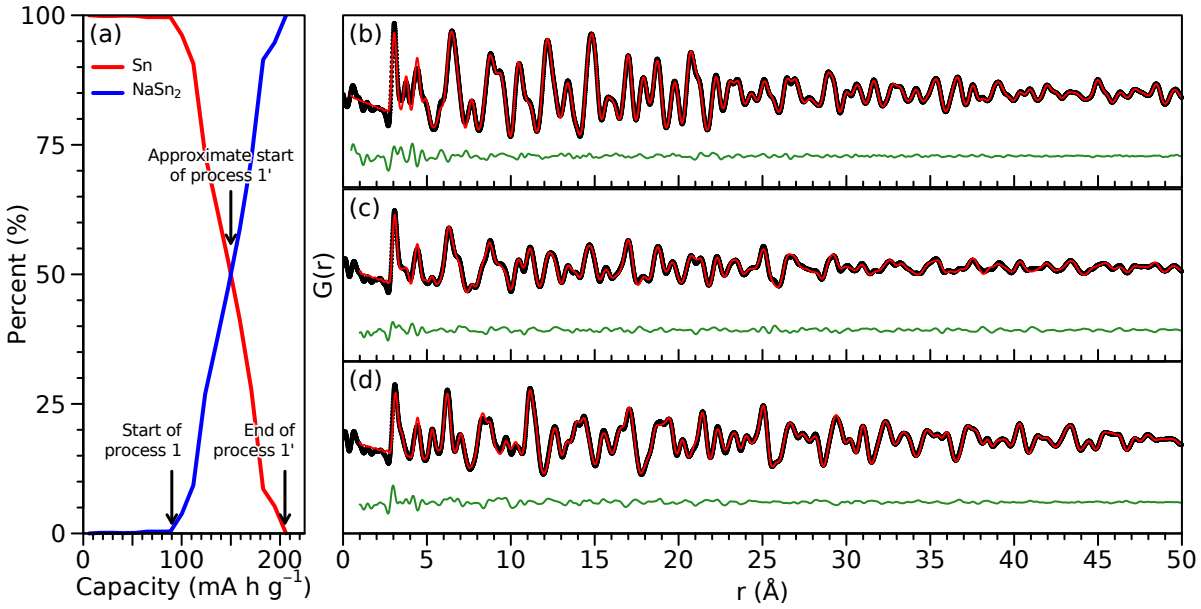

Figure 5.6: PDFs obtained during an *operando* measurement at the end of electrochemical processes (b) 0, (c) 1, and (d) 1′. Experimental data are shown as black circles, fits to (a) β-Sn (R_w=0.13), (b) a 1:1 mixture of β-Sn and $NaSn_2$ (R_w=0.18), and (c) $NaSn_2$ (R_w=0.13) are shown as red lines and the differences as green lines offset below. The proportion of Sn and $NaSn_2$ used in the refinements is shown in (a). The cell was cycled at a rate of C/70 (corresponding to achieving the theoretical capacity in 70 hours) and data were gathered at 2 hour intervals.

5.3.6 Processes 2 and 2′

PDF measurements reveal that the process(es) at approximately 220 mV result in the breakdown of almost all long-range structure, forming an amorphous solid. The stoichiometry of this phase has previously been suggested to be approximately $Na_{1.2}Sn$.[41,106] As PDF is a total scattering technique, which does not rely on long-range order, our measurements are able to probe some structural features of the amorphous intermediate. A PDF measurement taken at the end of these processes (Figure 5.8) reveals relatively strong features at low-r, which rapidly decay with increasing-r. Beyond approximately 15 Å, peaks in the PDF are approximately constant, with the decay in intensity consistent with instrument resolution as opposed to limited particle size. This would be consistent with having two phases present: a short-range, more disordered, phase with a correlation length around 15–30 Å; and a more ordered phase with a much greater correlation length. Similar behaviour has been observed in the sodium–antimony and lithium–FeOF systems.[124,125] Alternatively, it is possible that such a PDF could be generated through very anisotropic disorder. In this situation, the decay in intensity at low-r would be caused by strong disorder in one or two lattice directions, with a greater degree of ordering in the remaining direction(s) resulting in the retention of peaks at higher-r.

The strongest peak in the PDF, present at 3.00 Å, can only be the result of tin-tin connectivity. Such a peak would be present in extended structures such as $NaSn_2$, as well as one dimensional chains of tin atoms, tin tetrahedra or tin dumbbells. Na_1Sn_1-$I4_1/acd$ is the only stable phase found with a sodium concentration between $Na_{0.5}Sn$ and Na_2Sn. NaSn consists of tin

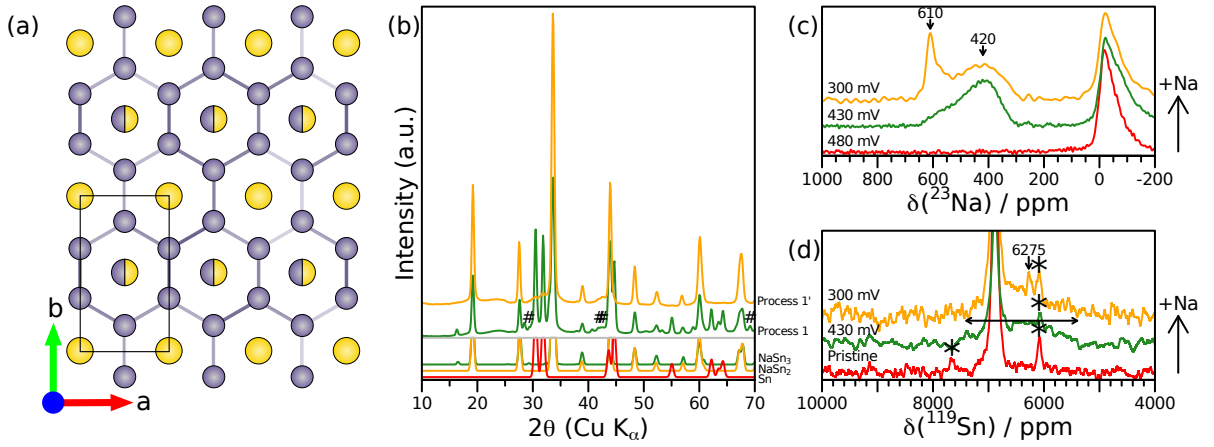

Figure 5.7: (a) A projection of the $NaSn_3$ *Pmmm* structure viewed down the *c*-axis, demonstrating the structural similarity to $NaSn_2$. Sodium atoms are shown in yellow, tin in grey, mixed occupancies are shown as a mixture of yellow and grey. (b) Frames from an *operando* XRD experiment taken at the end of electrochemical processes 1 (green) and 1′ (orange). Note in particular the peak at 16.5° in the data for process 1, which, along with others, cannot derive from $NaSn_2$. Calculated patterns are shown below for Sn (red), $NaSn_2$ (orange) and $NaSn_3$ (green) (large peaks have been truncated for clarity), trace amounts of Na from the cell background are indicated by #. Data were gathered using X-rays of wavelength 0.1430 Å and converted to Cu K_α (1.54 Å). *Ex situ* (c) ^{23}Na (d) ^{119}Sn 60 kHz MAS NMR spectra of tin anodes discharged to 480 mV (bottom, red), 430 mV (middle, green) and 300 mV (top, orange). Intensities have been normalised based on the sample mass and number of transients collected. Spinning sidebands are indicated with an asterisk (∗). In (c) shifts are indicated for peaks not resulting from SEI, sodium inserted into the Super P carbon additive or sodium within the carboxymethyl cellulose (CMC) binder (these constitute the broad peak between approximately −100–0 ppm). In (d) the shift of the peak arising from $NaSn_2$ is indicated at 6275 ppm. The broad peak arising from the $NaSn_3$ intermediate is indicated by a horizontal arrow. The strong peak resulting from β-Sn at 6890 ppm has been truncated for clarity.

tetrahedra, however, the inter-tetrahedra distances present in this structure are inconsistent with peaks found at higher-*r* (Figure 5.9).

In order to investigate the nature of this amorphous structure, we generated an Na_1Sn_1 amorphous phase using *ab initio* MD. Using this structure as a starting point, we performed a RMC refinement of a 10×10×10 supercell against a single scan from our *operando* PDF experiment, taking into account both real- and reciprocal-space data. Using only minimum distance constraints (based upon the measured PDF data) we were able to successfully reproduce the disordered (short-range) phase in the observed PDF.

RMC cannot readily be used to produce a complete model for materials, such as this, with both amorphous and crystalline components. We therefore performed additional real-space refinements using a least-squares method combining both a 61 atom subcell of the RMC refined $Na_{1.18}Sn$ model along with the crystalline phase described later (see section 5.2.3 for details). We used this method to quantify how the structure changed during the electrochemical process. Results are summarised in Table 5.3, note that phase fractions are not shown owing to the mixture of amorphous and crystalline components.

As RMC refinements are typically highly dependent upon the initial conditions, and the

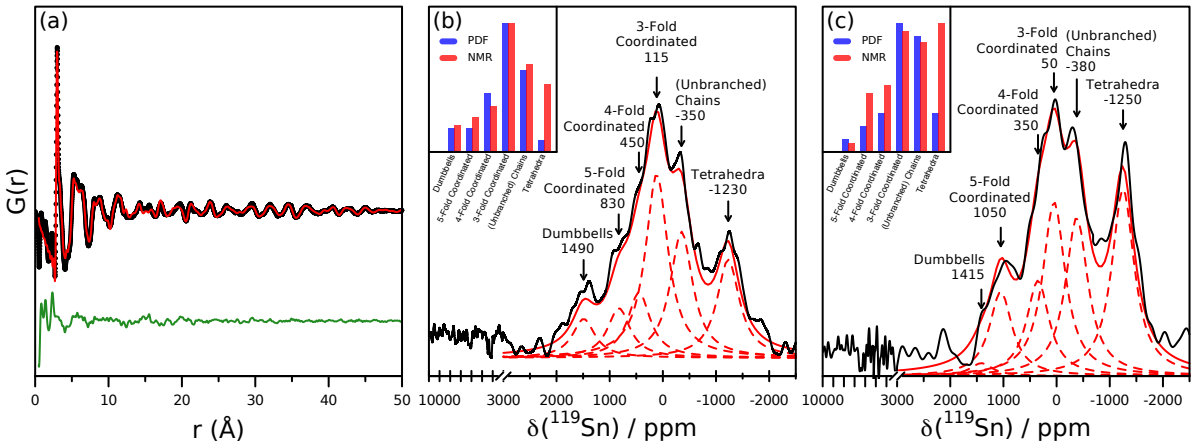

Figure 5.8: (a) PDF of a single frame from our operando experiment showing the intermediate formed at the end of processes 2 and 2′ on discharge. Two phases can be observed in the PDF: a short-range, disordered, phase below approximately 15 Å, and a longer-range phase whose peaks are clearly visible beyond 15 Å. Experimental data are shown as black circles, the red line represents the calculated PDF, with its difference to the experimental PDF offset below in green. (b and c) *Ex situ* ^{119}Sn 60 kHz MAS SSNMR spectra of tin discharged to the end of processes 2 (200 mV) and 2′ (120 mV), respectively. Experimental data are shown as solid black lines, deconvolutions are shown as red dashed lines, with arrows indicating the shifts and assignment of the deconvolved peaks. The overall fit is indicated with a solid red line. Data are plotted in the ranges −2500–3000 ppm and 3000–10 000 ppm. Inset: Histograms detailing the relative areas of the deconvolved peaks (red) along with the relative concentrations of each Sn-Sn connectivity in the structures refined against PDF measurements (blue). The PDF and NMR derived concentrations of each connectivity match well, with the exception of tetrahedral connectivity. We ascribe this discrepancy to the relaxation of this metastable intermediate into the thermodynamically stable NaSn phase, which is based on tin tetrahedra, relaxation occurring during the elapsed time between the end of the cell discharge, disassembly of the cell, and the *ex situ* NMR measurement.

resulting model does not necessarily represent a unique solution, it is important to assess the quality of this model through complementary experiments. In order to do so, we performed ^{119}Sn MAS SSNMR measurements on samples discharged to the end of these processes. The chemical shift is highly dependent on the Sn-Sn connectivity. We compared the relative concentration of each Sn-Sn connectivity in structures refined against PDF measurements during processes 2 and 2′ (blue histograms in Figure 5.8b and c) with the peak areas of the corresponding deconvolved NMR spectra (red histograms in Figure 5.8b and c). Spectra were fit using six Lorentzian curves, each with identical half widths at half maxima. The shifts for tin atoms in dumbbell or tetrahedral environments were derived from measurements on model compounds (Figure 5.10) with the remaining deconvolved peaks being tentative assignments based on the agreement with the expected concentrations and the ordering of the peaks.

Results are shown in Figure 5.8. As it is not possible to quantify all sources of error in the measurements and fitting, the discrepancies between the results from the two different techniques represent a measure of this error. There is reasonable agreement between the expected form of the spectrum and the measured data for every connectivity excluding tetrahedra. In both NMR spectra, we observe a much stronger signal from tetrahedra than

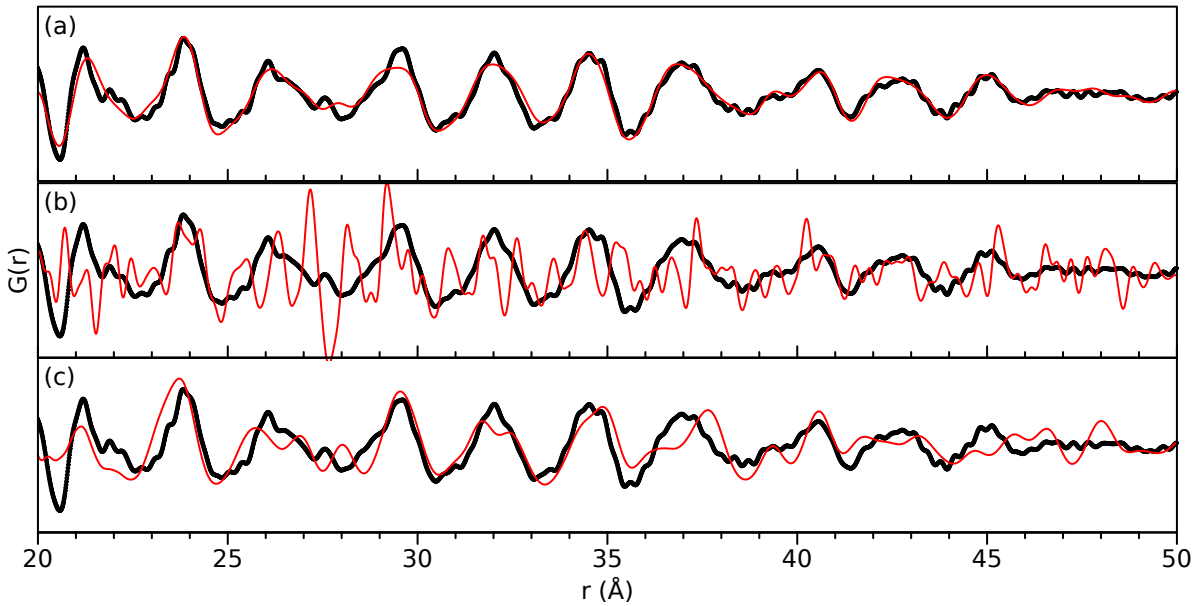

Figure 5.9: PDF obtained during an *operando* measurement at the end of electrochemical process 2′. Experimental data are shown as black circles, simulations of (a) expanded $NaSn_2$, (b) crystalline NaSn, and (c) crystalline NaSn with higher thermal displacement parameters are shown as red lines. PDF simulations were performed in PDFGUI.[67] For (a) and (b) U_{iso} parameters were set to 0.1 for Na atoms and 0.01 for Sn atoms, for (c) $U_{iso,Sn}$=0.05 and $U_{iso,Na}$=0.5. $Delta_1$ (low-r peak sharpening parameter) was set to 1.7 for all simulations, and Q_{damp} (instrument resolution parameter) was set to the value obtained from a refinement of the pristine material.

would be expected from the amount present in the model structures. A small amount of relaxation of the *ex situ* sample to the thermodynamically stable NaSn structure is likely, which accounts, at least in part, for the larger amount of tetrahedrally coordinated tin observed in the NMR spectra than the PDF derived models.

Ex situ ^{23}Na measurements (Figure 5.11) reveal a similar trend, with significant intensity in two major regions in addition to the signal resulting from SEI, sodium incorporated into carbon and CMC located around −17 ppm. These two regions are at approximately 19 ppm, which we assign to sodium atoms near four coordinate tin (tetrahedra) and 70 ppm, which corresponds to sodium near tin chains.

^{23}Na *operando* NMR measurements (Figure 5.2) corresponding to process 2 reveal a resonance at a shift of 45 ppm which grows throughout the process. During process 2′, the peak is observed to continually shift and broaden until it reaches 70 ppm. Combined, these observations suggest that a more ordered structure is formed at the start of the process, which then undergoes a solid-solution type phase transition into a more disordered structure consistent with observations of an amorphous structure formed in this region.

The periodic longer-range correlations found in the PDF data result from a more ordered component of this phase. They are consistent with the correlations found within structures based upon $NaSn_2$, but with significant changes required relative to the phase formed at the end of the first processes. A reduction in the a-lattice parameter is required, along with an expansion of the c-lattice parameter and a significant increase in the anisotropic

Table 5.3: Summary of the PDF refined parameters for the structures formed during electrochemical processes 2 and 2′.

	$NaSn_2$					Amorphous $\sim Na_{1.2}Sn$						
Capacity / mAh g^{-1}	a / Å	c / Å	U_{Na}	U_{Sn}	$U_{33,Sn}$	a / Å	b / Å	c / Å	Spherical Particle Diameter / Å	U_{Na}	U_{Sn}	R_w
219.632	5.308	3.226	0.057	0.027	0.026	11.650	12.490	12.218	41.196	0.014	0.007	0.165
247.170	5.308	3.226	0.057	0.027	0.026	11.650	12.490	12.218	41.196	0.014	0.007	0.137
274.248	5.307	3.227	0.057	0.029	0.026	11.621	12.570	12.237	30.155	0.013	0.009	0.160
301.786	5.304	3.231	0.057	0.023	0.028	11.584	12.584	12.205	34.253	0.018	0.013	0.224
329.323	5.292	3.233	0.057	0.027	0.065	11.615	12.591	12.229	31.818	0.019	0.014	0.246
356.860	5.230	3.572	0.057	0.059	0.284	11.612	12.446	12.276	28.629	0.024	0.015	0.265
384.398	5.197	3.618	0.129	0.071	0.241	11.709	12.437	12.269	29.058	0.014	0.024	0.273
411.476	5.197	3.618	0.129	0.071	0.241	11.709	12.437	12.269	29.058	0.014	0.024	0.260
439.013	5.200	3.614	0.129	0.060	0.191	11.709	12.437	12.269	29.058	0.014	0.024	0.255

thermal displacement parameter for tin in the c-lattice direction. Whilst it was not possible to refine sodium occupancies or positions owing to their very small contribution to the PDF, the expansion of the interlayer distances (c-direction) could be a result of additional sodium atoms between the tin layers. The increased thermal displacement parameter is indicative of changes to the planarity of the layers, likely resulting in significant changes to the electrical properties of the material. It is worth noting that similar effects in other systems are used as a means of electrochemical exfoliation.[126]

Performing further refinements based upon the intermediate PDF scans reveals that the changes in lattice parameters of the $NaSn_2$ structure occur when the electrochemical profile changes from a flat plateau-like region to a more sloping region (i.e. during process 2′). Sloping regions in electrochemical profiles indicate solid-solution mechanisms, this is consistent with the observed changes to the $NaSn_2$ structure. The shifting and broadening peak observed in the *operando* ^{23}Na ssNMR measurement further shows that the local environment around the sodium atoms is changing (i.e. a solid-solution mechanism) and becoming more disordered. The relatively low values of the NMR shift compared with other NaSn phases indicates that this material is much less metallic.

We tentatively suggest that processes 2 result in the formation of an amorphous structure consisting primarily of chains of tin atoms, with the higher-order connectivities observed as a result of branching within the chains. Further insertion of sodium atoms during process 2′ occurs between the tin layers of any remaining $NaSn_2$, causing an expansion of the interlayer distances and disorder along the c-lattice direction.

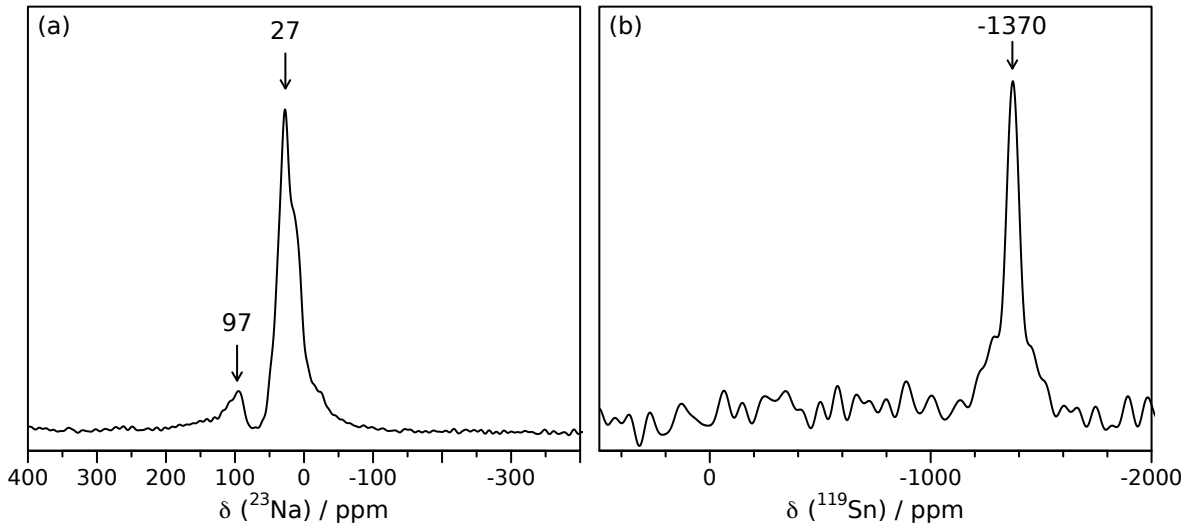

Figure 5.10: *Ex situ* (a) ^{23}Na (b) ^{119}Sn 60 kHz MAS NMR spectra of an NaSn model compound prepared by ball-milling. The shifts of the peak maxima are indicated. Tin powder (Sigma Aldrich, 99%, particle size 45 µm) and sodium (Sigma Aldrich, 99.9%) in a 1:1 ratio were ball-milled under argon in a zirconia ball mill jar using a SPEX 8000M Mixer / Mill for 8 hours. The resulting powder was stored in an argon atmosphere glove box (O_2, H_2O < 0.1 ppm) prior to use. Formation of NaSn was confirmed by XRD.

5.3.7 Processes 3 and 3′

During these electrochemical processes, the return to long-range ordering is evident from our PDF data. The low-*r* data are consistent with Sn-Sn dumbbells (Figure 5.12) as expected based upon the stable phases we predict in this regime of sodium concentration (Figure 5.1a). The simulated PDFs for all known structures containing parallel dumbbells are very similar below approximately 10 Å. However, differences in the sodium content of the phases causes differences in longer-range ordering.

Our *operando* ^{23}Na ssNMR experiment indicates that these processes do not result in the

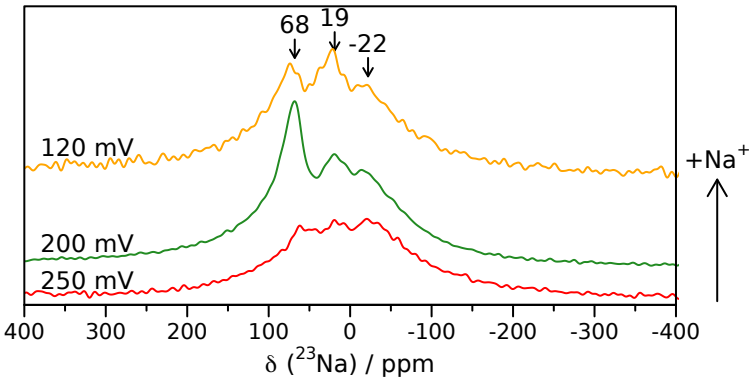

Figure 5.11: *Ex situ* ^{23}Na 60 kHz MAS NMR spectra of tin anodes discharged to 250 mV (bottom, red), 200 mV (middle, green) and 120 mV (top, orange). Shifts are indicated for all peak maxima. The peak with maxima around −22 ppm results from sodium within the SEI layer, carbon additive and CMC binder. Intensities have been normalised based on the sample mass and number of transients collected.

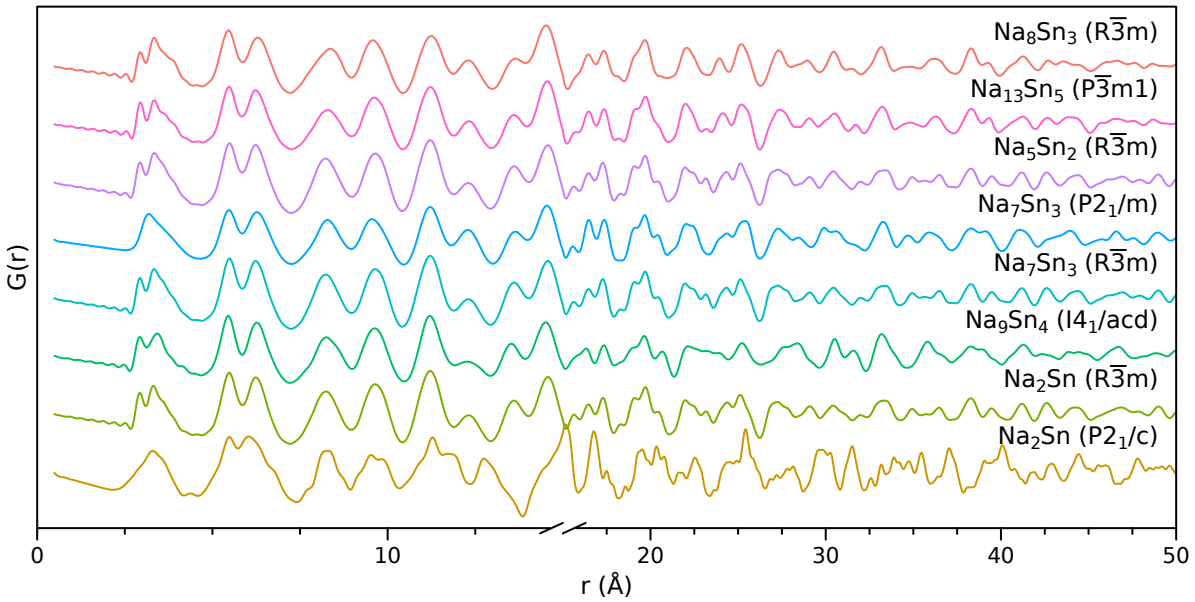

Figure 5.12: Simulated PDFs of several dumbbell phases. It is evident that the short-range structure of many of these structures is similar, there are, however, differences exist in the longer-range ordering. PDF simulations were performed in PDFGUI.[67] U_{iso} parameters were set to 0.05 for Na atoms and 0.01 for Sn atoms. $Delta_1$ (low-r peak sharpening parameter) was set to 1.7, and Q_{damp} (instrument resolution parameter) was set to the value obtained from a refinement of the pristine material.

formation of a single structure with fixed stoichiometry. We first see a single peak grow with a fixed shift of 203 ppm throughout process 3. However, upon reaching the end of the plateau, the peak continues to grow whilst simultaneously shifting to a final value of 183 ppm during the sloping process 3′ (Figure 5.2b). This suggests that this process proceeds firstly via a two-phase reaction, then by a solid solution reaction. In order to identify these structures, we performed refinements against multiple data sets from our *operando* PDF experiment. Initial refinements (Table 5.4 and Figure 5.13) suggested three potential structures, all of which were able to match the PDF data well: Na_2Sn, Na_7Sn_3 and Na_5Sn_2 (R_w=0.18, 0.18 and 0.19 respectively). These structures all belong to the $R\bar{3}m$ space group. The major difference between these three structures is the addition of a third sodium site in the Na_7Sn_3 and Na_5Sn_2 structures compared with the Na_2Sn structure (having an occupancy of 0.8 and 1, respectively), as highlighted in Figure 5.14a. Whilst they all provide a good match in terms of a low residual, the latter two structures required higher values for the thermal displacement parameters (U_{iso}) of the sodium atoms. This suggests that the contribution of sodium correlations to the fitted PDF is being broadened in order to match the experimental data, implying the sodium positions and / or stoichiometry in the model structures is incorrect. Through refining the thermal displacement parameter for the third sodium site independently of the other two, it is apparent that the sodium in this site has a substantially higher value for U_{iso}, indicating that the refinement is seeking to disorder these sites, i.e. the models are likely incorrect. We performed further refinements based upon the Na_5Sn_2 structure, but allowing the occupancy of this site to vary. This revealed a linear increase in the occupancy during the sloping electrochemical process 3′ (Figure 5.14b), starting at a value of approximately 0.4 and ending at approximately 0.75. The occupancy may also be indirectly derived from the observed volume expansion of the crystal lattice: the rate of increase of occupancy is

identical to that obtained through PDF refinements if an ionic radius for sodium of 1.10 Å is assumed. This is consistent with the sodium ions having a coordination number between 6 and 8.[127] An example of the fit to a measured PDF is given in Figure 5.14c, and results are summarised in Tables 5.5 and 5.6.

Table 5.4: Results of preliminary real-space least-squares refinements performed in PDFGUI.[67] for all known and predicted structures with appropriate stoichiometries for the structure formed during process 3. U_{iso} parameters for all atoms were set to an initial value of 0.01. Unit cell parameters, phase scale factor, delta$_1$ (low-r peak sharpening parameter) and the thermal parameters for both Na and Sn were all refined. Q_{damp} (instrument resolution parameter) was set to the value obtained from a refinement of the pristine material.

Structure	Space Group	Origin	U_{Na}	U_{Sn}	R_w	
$Na_{12}Sn_7$	$Pnma$		0.004	0.034	0.38	
Na_2Sn	$P2_1/c$		0.006	0.087	0.75	
Na_2Sn	$R\bar{3}m$		0.074	0.039	0.18	*
Na_2Sn	$Cmcm$	Ref 41	0.138	0.124	0.94	
Na_2Sn	$Cmcm$	Ref 41	0.330	0.069	0.73	
Na_9Sn_4	$Cmcm$	Ref 119	0.020	0.040	0.45	
Na_7Sn_3	$P2_1/m$		0.151	0.036	0.45	
Na_7Sn_3	$R\bar{3}m$	Ref 41	0.097	0.037	0.18	*
Na_5Sn_2	$R\bar{3}m$		0.104	0.036	0.19	*
$Na_{13}Sn_5$	$P\bar{3}m1$		0.079	0.037	0.32	
Na_8Sn_3	$R\bar{3}m$		0.056	0.048	0.40	
Na_3Sn	$Immm$	Ref 41	0.381	0.129	0.98	
Na_3Sn	$Pmnm$	Ref 41	0.017	0.108	0.55	
Na_3Sn	$Pmnm$	Ref 41	0.067	0.175	0.66	
$Na_{13}Sn_4$	$Pbam$		0.011	0.052	0.35	

* Selected for further study

We, therefore, propose that this electrochemical process starts with the formation of $Na_{4.4}Sn_2$ during process 3 followed by a solid solution of structures of the form $Na_{5-x}Sn_2$ during process 3′, ending at $Na_{4.75}Sn_2$. This is also consistent with the observed slope in the electrochemistry during process 3′, which is typically indicative of solid-solution behaviour.

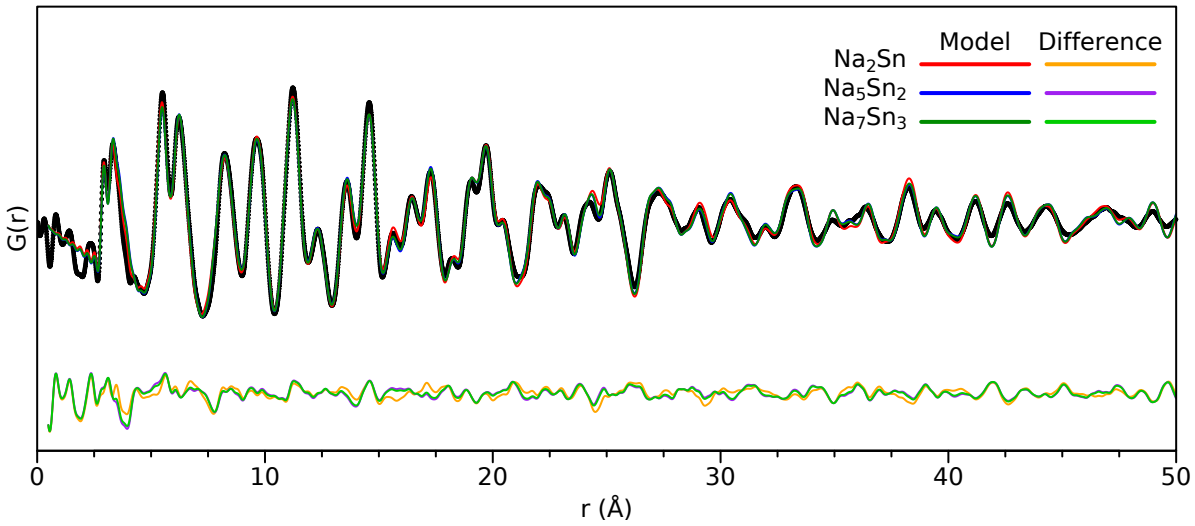

Figure 5.13: PDF obtained during an *operando* measurement at the end of electrochemical process 3′. Experimental data are shown as black circles, a fit to Na_2Sn is shown as a red line, Na_5Sn_2 as a blue line and Na_7Sn_3 as a green line. Differences are offset below as orange, purple and green lines, respectively.

5.3.8 Processes 4 and 4′

The final discharge product, $Na_{15}Sn_4$, is well-known in the literature.[38,41,106,128] We were not able to observe complete formation of this phase during our *operando* PDF measurement, which we believe was due to the increased resistance of the *operando* electrochemical cells. In addition, we were unable to hold the cell at the end of discharge for long enough to allow complete conversion owing to the limited amount of allocated beamtime; complete conversion was observed during the *operando* NMR measurement, however, owing to the greater amount of time spent holding the cell potential at 1 mV. *Ex situ* PDF measurements were able to confirm the formation of $Na_{15}Sn_4$, with no significant distortions from the average $Na_{15}Sn_4$ structure (Figure 5.15). During our *operando* ^{23}Na NMR experiment, however, we observed the formation of peaks at both -75 and −260 ppm at the end of discharge. The peak at −75 ppm is observed to grow first, and is tentatively ascribed to the formation of $Na_{15}Sn_4$. This structure consists of isolated tin atoms within an expanse of sodium atoms; the incorporation of an excess of sodium within this crystal structure would not require further breaking of Sn-Sn bonds and could therefore be expected to be relatively facile. It is to this ($Na_{15+x}Sn_4$) that we tentatively assign the signal at −260 ppm. This is analogous to the processes by which $Li_{15+x}Si_4$ and $Li_{15+x}Ge_4$ form electrochemically.[114,129] It should be noted that, whilst $Na_{15}Sn_4$ contains two crystallographically distinct sodium sites, the differing rates of growth of these two peaks suggests they result from different phases. Upon reversal of the current, the peak at −260 ppm almost immediately vanishes, and is replaced with a broader resonance around −360 ppm, which quickly disappears. The peak at −75 ppm shrinks much more gradually throughout the entire electrochemical process. This behaviour is identical to that seen in the lithium–silicon system.

Ex situ ^{119}Sn MAS SSNMR measurements for the material formed at the end of discharge (Figure 5.16b) reveal two sharp peaks at 122 ppm and 385 ppm. As $Na_{15}Sn_4$ only contains one

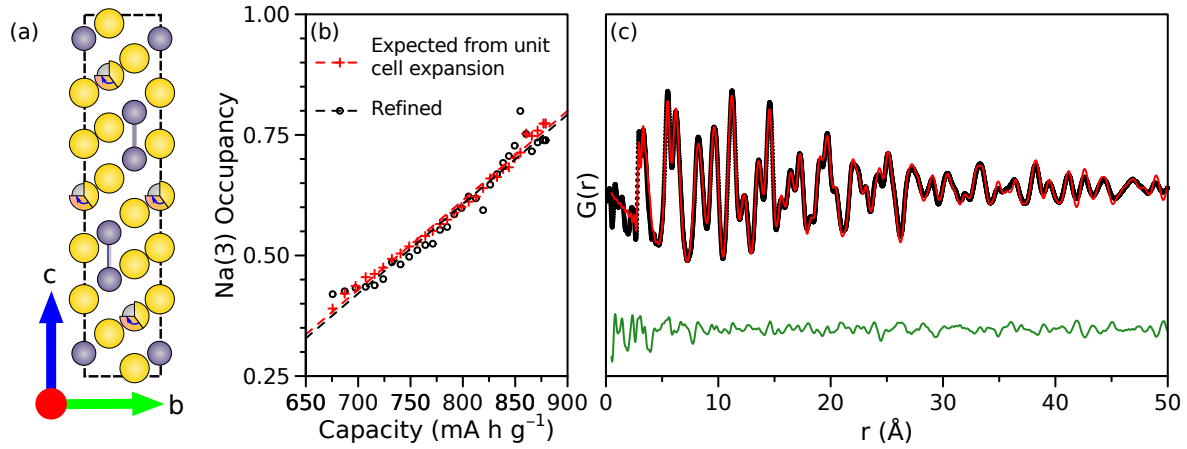

Figure 5.14: (a) A projection of the $Na_{5-x}Sn_2$ class of structures viewed down the *a*-axis. Sodium atoms are shown in yellow, tin in grey, the partial occupancies of the 3rd sodium site are indicated increasing from 0.4 to 0.75 by blue arrows. (b) A plot of the occupancy of Na site 3 vs time spent on this electrochemical process. Occupancies derived directly from PDF refinements are shown as black circles, occupancies determined from the volume expansion of the crystal lattice (assuming an Na ionic radius of 1.10 Å) are shown as red crosses. Trends are indicated for both data series as dashed lines. (c) Fit of the PDF corresponding to the first frame obtained during this process over the range 0–50 Å (R_w=0.19). Raw data are shown as black circles, the fit is shown as a red line, and the difference is shown as a green line offset below.

crystallographic tin site, this is further evidence for the formation of an additional structurally related phase at the end of discharge.

5.3.9 Relaxation

In order to verify that the structures formed during the 3rd electrochemical process are metastable as predicted by our calculations, we further performed an *in situ* ^{23}Na SSNMR experiment to observe how the structure relaxes upon removal of the applied current (Figure 5.17). We observe a continual shift and sharpening of the peak at 200 ppm formed upon discharge. This is a clear indication that the structure changes even without an applied current. During this time the measured potential is found to increase. The shift to higher frequencies is consistent with sodium removal from the structure, which is likely a result of reaction with the electrolyte or SEI. This would also be consistent with the increasing potential of the cell. Whilst detailed diffraction measurements have yet to be performed in order to identify the structure(s) formed, we present this as evidence supporting the use of *operando* measurements for both this system and other, highly reactive, alloying materials.

5.4 Discussion

Based on our PDF, XRD, SSNMR measurements and theoretical calculations, we propose the following discharge mechanism for the sodium–tin system (summarised in Figure 5.18):

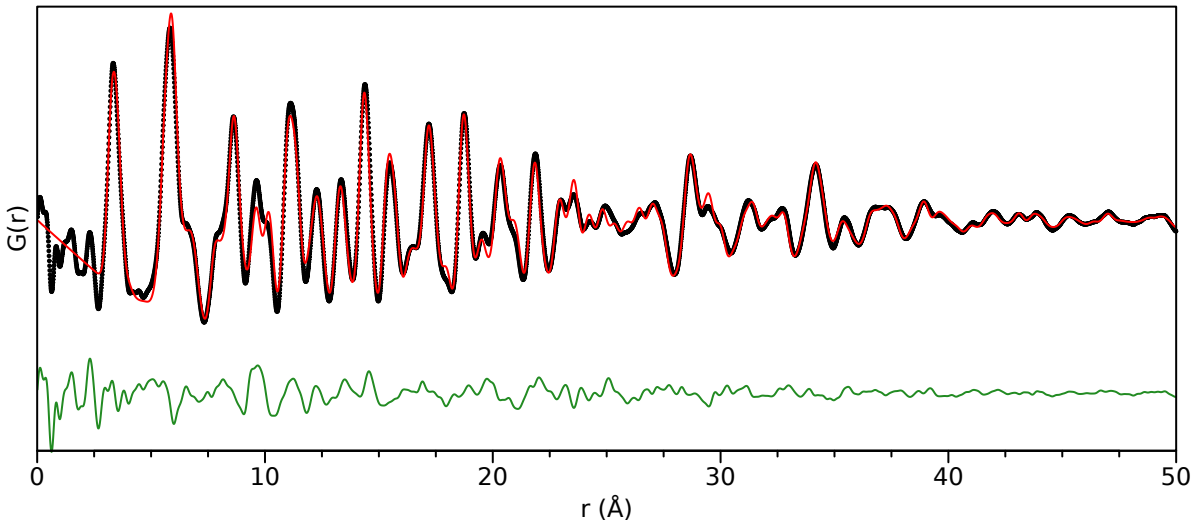

Figure 5.15: *Ex situ* PDF of a tin anode discharged to 1 mV. Experimental data are shown as black circles, a fit to $Na_{15}Sn_4$ (R_w=0.21) is shown as a red line and the difference as a green line offset below.

Process 1 : Sn $\longrightarrow$ $NaSn_3$
Process 1′: Sn, $NaSn_3$ $\longrightarrow$ $NaSn_2$
Process 2 : $NaSn_2$ $\longrightarrow$ a-$Na_{1.2}Sn$
Process 2′: a-$Na_{1.2}Sn$ + $NaSn_2$ $\longrightarrow$ a-$Na_{1.2}Sn$ + expanded $Na_{1+x}Sn_2$ (solid solution)
Process 3 : a-$Na_{1.2}Sn$ + expanded $Na_{1+x}Sn_2$ $\longrightarrow$ $Na_{4.4}Sn_2$
Process 3′: $Na_{4.4}Sn_2$ $\longrightarrow$ $Na_{4.75}Sn_2$ (solid solution)
Process 4 : $Na_{4.75}Sn_2$ $\longrightarrow$ $Na_{15}Sn_4$
Process 4′: $Na_{15}Sn_4$ $\longrightarrow$ $Na_{15+x}Sn_4$

The first transformation (Processes 1 and 1′) is from crystalline β-Sn to another crystalline material. This is in contrast to many alloying systems, notably sodium–antimony[96,124] and lithium–silicon,[130] where the first electrochemical process involves the formation of an amorphous structure due to the overpotential required to break up the crystalline lattice of the starting material. A transformation between two crystalline species without intermediate amorphisation suggests a relatively facile transition, requiring only small changes in tin connectivity. This is readily observable in our *operando* PDF data, with only minor changes observed at low-r (Figure 5.19a). These processes result in the conversion from β-Sn to a layered structure of composition $NaSn_2$ via an intermediate with a similar structure to $NaSn_2$ of approximate stoichiometry $NaSn_3$. Figure 5.19b and c demonstrates the similarity of the end-member structures, with significant short-range changes highlighted with coloured lines.

NMR measurements of this phase reveal strongly Knight shifted features consistent with the likely electronic properties of the stanine-like tin layer. The slow convergence of the phonon spectra with respect to the k-point sampling, could also hint at a strong electron-phonon coupling and a complex Fermi surface shape. These properties are consistent with the structural similarities of this phase to structures such as MgB_2, which are studied in the context of high-temperature superconductors.[131] The full understanding of the electronic

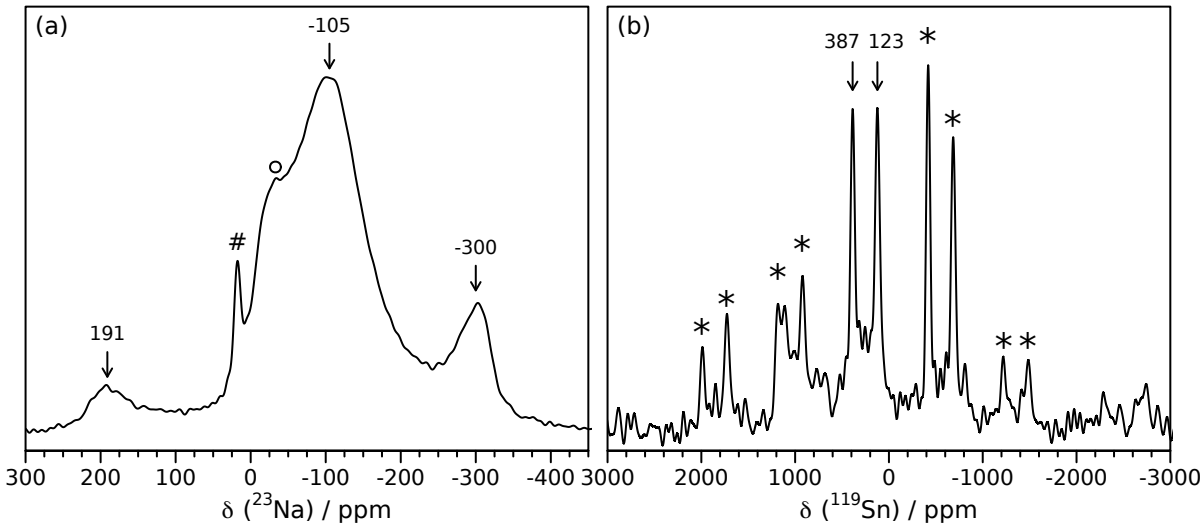

Figure 5.16: *Ex situ* (a) ^{23}Na (b) ^{119}Sn 60 kHz MAS NMR spectra of a tin anode discharged to 1 mV. Shifts are indicated for isotropic peak maxima. In (a), the small, broad peak around 191 ppm corresponds to the structures formed during electrochemical processes 3 and 3′. The peak labelled # corresponds to trace amounts of NaOH, and the peak labelled ∘ results from sodium within the SEI layer, carbon additive and CMC binder. In (b), a small, broad peak is also present around 1000 ppm, which corresponds to the structures formed during electrochemical processes 3 and 3′. Spinning sidebands are indicated with a ∗.

structure of $NaSn_2$ is, however, beyond the scope of this study.

The lower sodium-content phase, approximate composition $NaSn_3$, is almost identical to that of $NaSn_2$ noted earlier, but with a reduction in symmetry caused by the presence of tin atoms within the sodium layers. The formation of this additional intermediate implies that whilst the breakup of β-Sn is relatively facile compared to other alloying systems, there is a preference to go via an additional structurally related intermediate ($NaSn_3$) rather than phase separate into the two end member phases, β-Sn and $NaSn_2$. It is possible that this may help to mediate strain at the interface between the two phases.

The second electrochemical process is kinetically driven, resulting primarily in the formation of an amorphous phase, rather than the thermodynamically-stable NaSn. The high melting-point of the crystalline NaSn phase,[132] along with its low electrical conductivity, as observed by NMR, both point to low atomic mobility within the structure. This, combined with the large structural rearrangement that would be necessary to form Sn_4 clusters in the crystalline thermodynamic phase, is a likely reason for why it does not form.

The tin connectivity in the amorphous phase primarily consists of chains of tin atoms, likely a consequence of the fact that it forms from the layered $NaSn_2$ phase. Despite this, we observed a clear tendency towards a small amount of tetrahedral connectivity, which is present in the thermodynamically stable crystalline NaSn phase. This indicates that the transformation is not exclusively kinetically driven, and the relative concentrations of the different species in the amorphous phase are likely rate dependent. In this region, we additionally observe some expansion and disordering in the interlayer direction of the $NaSn_2$ structure, indicating that addition of sodium between the layers of $NaSn_2$ might be kinetically more facile than

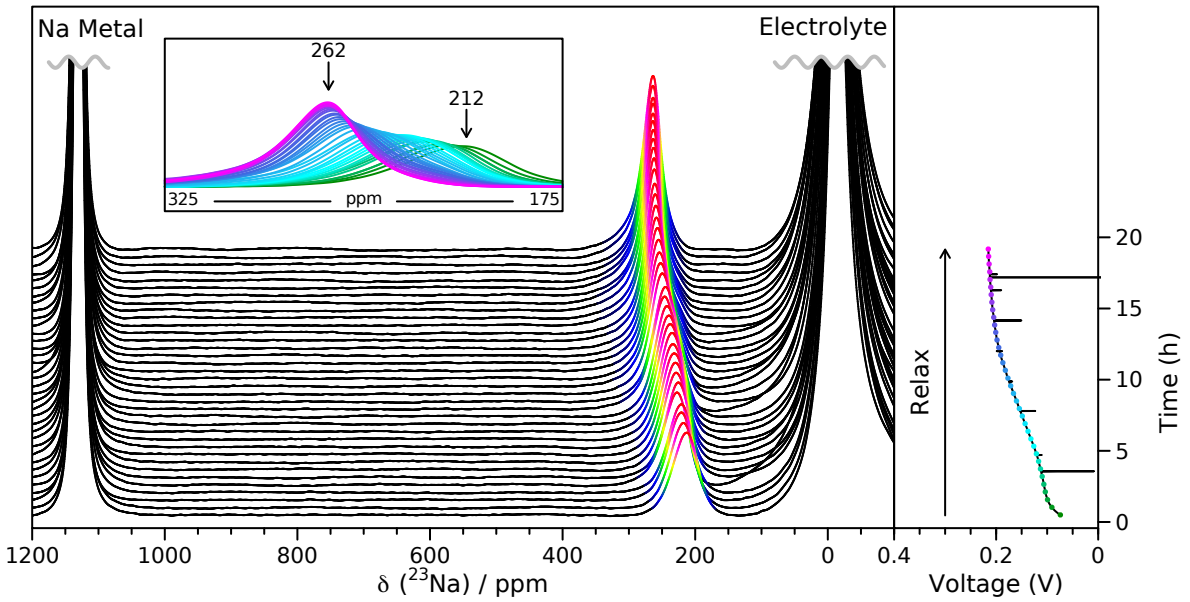

Figure 5.17: *In situ* ^{23}Na NMR measurement for a cell with sodium metal and tin electrodes, and a $NaPF_6$ electrolyte, which was allowed to relax after discharging to the end of electrochemical process 3. NMR data is shown on the left, with the corresponding electrochemistry on the right. Strong features corresponding largely to the electrolyte or metal have been truncated for clarity. Spectra are coloured in the region 100–1000 ppm according to their intensity. Inset: a close-up of the region between 175–325 ppm highlighting the shifting peak. The colours now correspond to the points shown on the electrochemical curve.

breaking up the extended lattice. This is not unexpected owing to the ability of other layered materials (notably graphite) to swell and, ultimately, exfoliate electrochemically.[126]

At sodium concentrations higher than Na_2Sn, structures based upon tin dumbbells are formed. Our DFT calculations predict numerous dumbbell phases at similar energies, similar behaviour also having been observed for a number of other chemically-related systems.[129,133] It is clear that the structures formed experimentally during these process are very similar to Na_2Sn, Na_7Sn_3 and Na_5Sn_2 — three structures that differ primarily through the occupancy of one of their sodium sites. The occupancy of this site was found (via refinement of the site occupancy) to increase linearly throughout the sloping electrochemical process 3′, thus providing an explanation for the solid-solution behaviour implied by the electrochemistry. The addition of further sodium to the existing phase, rather than the immediate nucleation of $Na_{15}Sn_4$, is once again kinetically driven. The presence of a number of related structures at similar energies allows for a relatively facile transition between them simply through adding additional sodium atoms between the dumbbells. Conversely breaking up the tin dumbbells requires a greater input of energy. This result implies metastability of the structures produced during these processes. A further consequence of this may be that the structures formed may be different upon discharge and charge, as well as relaxation effects upon removal of the current; this is discussed further in chapter 6.

Given the number of apparently flat plateaus in the electrochemical profile, along with the relatively high number of crystalline intermediates, it may appear at first glance that the Na–Sn system is thermodynamically driven. The calculated voltage curve obtained from

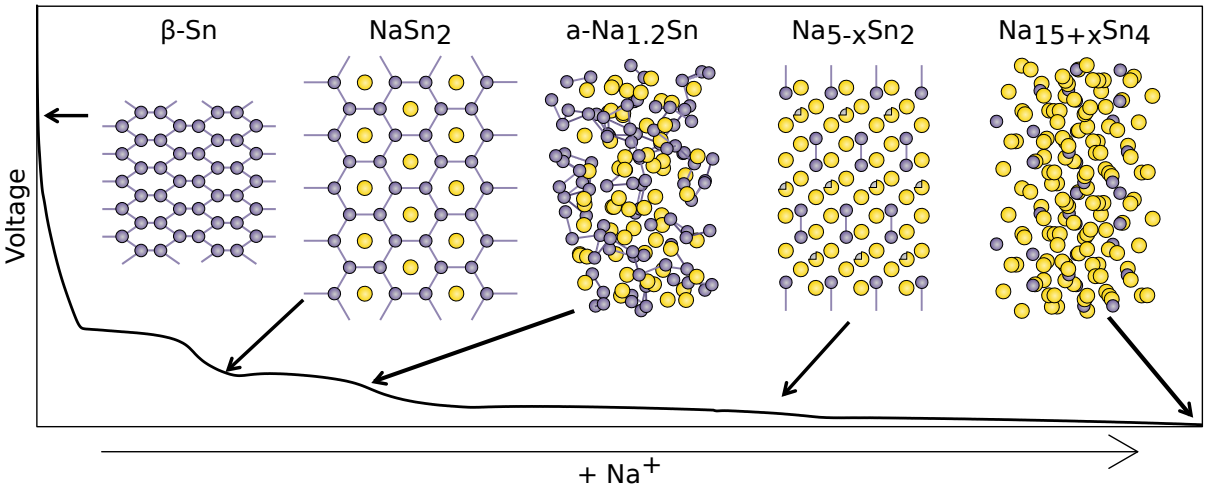

Figure 5.18: A summary of the major structural changes that occur during the discharge of a sodium–tin battery.

the structures predicted to be stable in DFT calculations matches the experimental curve fairly well, demonstrating the predictive capability of the theoretical methods used. The disagreement between the theoretical and experimental voltages (as shown by the difference between the blue and black lines in Figure 5.1b) can be attributed mainly to experimental effects such as finite particle size, surface and kinetic effects including overpotentials, which are not included in the modeling. From our experimental data, it is also clear that kinetic considerations are very important to the transformations taking place, and understanding these additional complexities is necessary in order to understand the complex electrochemical behaviour of the system. We note that the behaviour during the kinetically-driven regions is likely to be highly dependent on the overpotential at which the cell operates. This can be affected by electrode formulation, charge rate and experimental setup, among other things, and can explain differences between the electrochemistry presented here and in other studies, most notably in thin films. These differences are also important to understand in the context of binary and ternary alloys with tin as a component, as the presence of additional inactive matrices, other active elements and interfaces between nanosized regions is likely to have an effect on the kinetic pathways taken. For these electrodes to be implemented in practical systems, a full understanding of these processes as a function of experimental details such as rate and electrode formulation will be required.

5.5 Conclusions

We were able to fully model our *operando* PDF and XRD data, which, combined with information from *operando* SSNMR measurements, provide a comprehensive understanding of the sodium–tin electrochemical system. Experimental evidence for the formation of $NaSn_2$ during the first electrochemical processes, a phase predicted by our DFT calculations to be thermodynamically stable is presented. The results represent the first structural evidence that these processes result in the formation of two phases (the other being of approximate

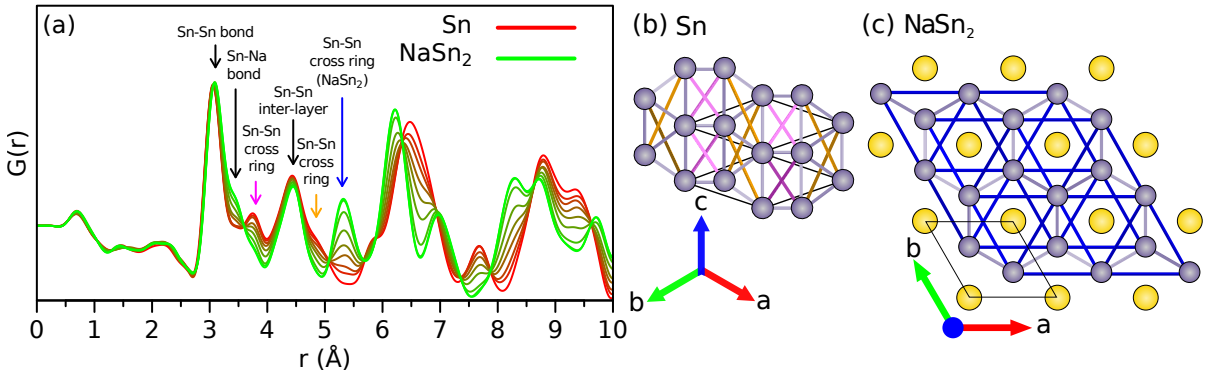

Figure 5.19: (a) PDFs obtained during an operando measurement corresponding to electrochemical processes 1 and 1′. The first scan during this process corresponds to β-Sn (red), the last to $NaSn_2$ (green). The cell was cycled at a rate of C/70 (corresponding to achieving the theoretical capacity in 70 hours) and data were gathered at 2 hour intervals. (b) A projection of the β-Sn structure viewed in the [111] direction. The short-range correlations lost during the structural transformation are indicated as orange and magenta lines, and are shown with the same colour arrows in (a). (c) A projection of the $NaSn_2$ structure viewed down the *c*-axis. The short-range Sn-Sn correlations gained during the structural transformation are indicated with blue lines, and are shown with a blue arrow in (a). Tin atoms are shown in grey, sodium in yellow; Sn-Sn bonds are shown as grey lines.

composition $NaSn_3$, which bears a strong similarity to $NaSn_2$, with the addition of tin atoms within the sodium layers).

Reverse Monte–Carlo refinements against models produced by *ab initio* molecular dynamics were able to extract structural information about the amorphous intermediate formed during the second process, constraining the simulations with information from *operando* PDF measurements. The resulting model consists primarily of chains of tin atoms, and is consistent will all known experimental data on this phase. ^{119}Sn MAS SSNMR measurements were used to examine the connectivity present in the amorphous sodium–tin phases, with the value of the shift being found to be highly dependent upon the tin–tin connectivity. The relative concentration of each connectivity was shown to support the MD / RMC model.

Operando SSNMR data presented evidence for a solid-solution process during the process around 60 mV (labelled 3′). Detailed PDF refinements revealed an increase in occupancy of a single sodium site in dumbbell structures of the form $Na_{5-x}Sn_2$. Furthermore, our NMR data reveals for the first time the possibility of further sodium storage within the $Na_{15}Sn_4$ structure, formed towards the end of discharge, as an off-stoichiometry phase $Na_{15+x}Sn_4$, in a process analogous to that observed in the lithium–silicon system.

The first evidence for significant solid solution behaviour and resulting metastability in the sodium–tin system is presented. The study provides a clear demonstration of the need for a variety of techniques probing both short- and long-range structures, along with a detailed theoretical underpinning of model structures, in order to comprehensively understand the mechanism of sodium insertion. Our results have further implications beyond the sodium–tin system, highlighting the fact that even a system under apparent thermodynamic control, the nature of electrochemical alloying means that kinetic considerations remain very important.

Table 5.5: Results of real-space least-squares refinements in PDFGUI for Na_5Sn_2 against *operando* PDF data obtained during electrochemical process 3′. U_{iso} parameters for all atoms were set to an initial value of 0.01. Unit cell parameters, phase scale factor, $delta_1$ (low-r peak sharpening parameter) and the thermal parameters for both Na (all sites independently) and Sn were all refined. In addition, the z-positions of the sodium atoms were refined, and the occupancy of the Na_3 site. Q_{damp} (instrument resolution parameter) was set to the value obtained from a refinement of the pristine material. A range of initial values were attempted for the occupancy values, in all cases the result was the same.

Capacity / mAh g^{-1}	a / Å	c / Å	U(Na_1)	U(Na_2)	U(Na_3)	U(Sn)	z(Na_1)	z(Na_2)	z(Sn)	Occupancy (Na_3)	$Na_{15}Sn_4$ (%)	R_w
662.43	5.461	22.533	0.085	0.076	0.189	0.039	0.359	0.206	0.065	0.420	5.4	0.175
675.58	5.462	22.538	0.083	0.077	0.161	0.038	0.358	0.206	0.065	0.426	5.9	0.171
687.05	5.463	22.542	0.082	0.078	0.162	0.038	0.357	0.207	0.065	0.433	6.7	0.175
697.51	5.464	22.544	0.082	0.078	0.151	0.037	0.358	0.207	0.065	0.435	8.3	0.171
707.15	5.464	22.546	0.082	0.078	0.151	0.037	0.358	0.207	0.065	0.438	8.9	0.172
715.67	5.465	22.548	0.080	0.079	0.162	0.037	0.358	0.207	0.065	0.451	9.9	0.173
723.93	5.466	22.552	0.077	0.081	0.183	0.037	0.358	0.208	0.065	0.486	11.0	0.175
732.19	5.467	22.553	0.078	0.081	0.182	0.038	0.358	0.208	0.065	0.481	11.8	0.173
740.45	5.467	22.556	0.076	0.085	0.182	0.038	0.358	0.208	0.065	0.497	12.7	0.176
748.71	5.468	22.557	0.077	0.087	0.184	0.038	0.358	0.209	0.065	0.511	13.4	0.177
756.54	5.469	22.559	0.079	0.091	0.175	0.038	0.358	0.209	0.065	0.522	14.1	0.180
764.11	5.469	22.562	0.081	0.095	0.162	0.039	0.357	0.210	0.065	0.524	14.6	0.183
771.24	5.470	22.564	0.077	0.099	0.182	0.039	0.357	0.210	0.065	0.553	15.3	0.186
778.13	5.471	22.565	0.080	0.100	0.170	0.040	0.357	0.210	0.065	0.559	15.9	0.190
785.01	5.471	22.568	0.077	0.104	0.187	0.040	0.357	0.210	0.065	0.585	16.5	0.194
791.78	5.472	22.569	0.081	0.106	0.171	0.041	0.357	0.211	0.065	0.598	17.4	0.197
798.67	5.473	22.572	0.077	0.108	0.192	0.041	0.357	0.211	0.065	0.622	17.8	0.201
805.55	5.473	22.572	0.083	0.106	0.170	0.042	0.357	0.212	0.065	0.619	18.5	0.205
812.44	5.474	22.576	0.078	0.108	0.198	0.043	0.357	0.212	0.065	0.594	18.9	0.208
819.32	5.476	22.578	0.069	0.114	0.202	0.043	0.358	0.211	0.065	0.647	19.5	0.213
826.09	5.476	22.577	0.080	0.111	0.180	0.044	0.357	0.212	0.065	0.669	20.3	0.216
832.65	5.477	22.580	0.083	0.112	0.174	0.045	0.357	0.213	0.065	0.692	20.9	0.218
838.46	5.477	22.580	0.083	0.113	0.173	0.046	0.357	0.213	0.065	0.706	21.2	0.223
843.97	5.478	22.583	0.083	0.117	0.168	0.046	0.356	0.213	0.065	0.728	22.0	0.226
849.47	5.479	22.584	0.083	0.117	0.168	0.047	0.356	0.214	0.065	0.800	22.9	0.230
854.89	5.480	22.603	0.086	0.118	0.175	0.047	0.357	0.214	0.065	0.752	23.7	0.241
860.40	5.481	22.595	0.086	0.120	0.178	0.048	0.357	0.214	0.065	0.716	23.4	0.243
865.90	5.482	22.592	0.079	0.125	0.183	0.050	0.356	0.214	0.065	0.734	23.4	0.249
871.41	5.483	22.594	0.080	0.125	0.177	0.051	0.356	0.214	0.065	0.739	23.9	0.251
876.92	5.483	22.594	0.080	0.125	0.177	0.051	0.356	0.214	0.065	0.739	23.9	0.257
878.94	5.483	22.594	0.080	0.125	0.177	0.051	0.356	0.214	0.065	0.739	23.9	0.267

Table 5.6: Data used for the expected occupancy values shown in Figure 5.14. In addition to directly refining the Na_3 occupancy, the expected increase in occupancy was inferred using the unit cell volume expansion. A radius of 1.10 Å was assumed for the sodium ion, consistent with sodium having a coordination number between 6 and 8,[127] and a starting occupancy of 0.40 was also assumed based upon the refined value. The unit cell volume was calculated as $a^2c\sin\gamma$, and the expected occupancy as $\frac{1}{3}\cdot\frac{V_i-V_{i-1}}{\frac{4}{3}\pi(1.10)^3}+0.4$ where V_i is the refined volume of the unit cell for the ith dataset.

Capacity / mA h g^{-1}	Volume / Å^3	Expansion / Å^3	Additional Na	Expected Occupancy
662.43	581.91	0.00	0.00	0.40
675.58	582.26	0.35	0.06	0.42
687.05	582.53	0.62	0.11	0.44
697.51	582.84	0.92	0.17	0.46
707.15	582.95	1.04	0.19	0.46
715.67	583.17	1.26	0.22	0.47
723.93	583.47	1.56	0.28	0.49
732.19	583.66	1.75	0.31	0.50
740.45	583.90	1.99	0.36	0.52
748.71	584.05	2.14	0.38	0.53
756.54	584.27	2.36	0.42	0.54
764.11	584.44	2.53	0.45	0.55
771.24	584.68	2.77	0.50	0.57
778.13	584.84	2.93	0.52	0.57
785.01	585.07	3.16	0.57	0.59
791.78	585.28	3.37	0.60	0.60
798.67	585.46	3.55	0.63	0.61
805.55	585.64	3.73	0.67	0.62
812.44	585.94	4.02	0.72	0.64
819.32	586.27	4.36	0.78	0.66
826.09	586.32	4.41	0.79	0.66
832.65	586.60	4.69	0.84	0.68
838.46	586.66	4.75	0.85	0.68
843.97	586.98	5.06	0.91	0.70
849.47	587.17	5.26	0.94	0.71
854.89	587.83	5.92	1.06	0.75
860.40	587.75	5.84	1.04	0.75
865.90	587.94	6.02	1.08	0.76
871.41	588.18	6.27	1.12	0.77
876.92	588.18	6.27	1.12	0.77
878.94	588.18	6.27	1.12	0.77

6 Mechanistic Insights into Sodium Removal Effects in Tin Anodes

6.1 Introduction

Considering the large amount of solid-solution behaviour found to take place on sodium insertion into tin, there is reason to believe that the sodium removal process may be different. This is a common phenomenon amongst alloying materials; for example, both Li-Ge, and Na-Sb demonstrate different mechanisms on charge and discharge.[96,129] Looking beyond the first discharge (sodium insertion) for Na-Sn, a number of studies have investigated the first charge and beyond. In 2012, Ellis *et al.* used *operando* XRD to conclude that, with the possible exception of the formation of the first (lowest sodium content) phase on discharge, the reaction mechanisms are completely reversible, i.e. that the charge mechanism simply follows the inverse of the discharge.[106] A later *operando* TEM study reached the same conclusion, although they noted that the morphology of their nanoparticles had altered significantly following sodium removal, whilst they started spherical, they presented an irregular shape after charging.[107] The same authors suggest that the structure reconstruction plays a significant role in the shape change. Baggetto *et al.* noted a consistent difference in XRD peak intensities for analogous phases on charge and discharge.[41] They ultimately attributed these differences to preferred orientation effects rather than structural changes. Furthermore, they noted that the "amorphous" phase (approximately $Na_{1.2}Sn$) produced on discharge consisted of both amorphous and nanocrystalline components, whereas the phase produced during charging contained only the amorphous component. Finally, two later studies by Nam *et al.*, using electrodeposited tin electrodes, and Cheng *et al.*, using tin nanoparticles prepared by $NaBH_4$ reduction of $SnCl_2$, reached similar conclusions to the previous studies, again suggesting that the charge mechanism followed the reverse of discharge.[128,134]

In this chapter we seek to investigate the charging mechanism in greater detail. Whilst the analysis of these phases reported in the literature so far has used XRD as its principal technique, we focus instead on the use of local structural probes. Specifically, we aim to identify any differences in the structures formed on sodium removal *vs.* sodium insertion through a combination of PDF and ssNMR.

6.2 Experimental

Except were otherwise stated, all experiments were performed under ambient conditions.

6.2.1 Electrode Preparation

Electrode materials were prepared in an identical manner to section 5.2.1 on page 63.

6.2.2 PDF Analysis

Operando PDF measurements were performed at beamline I15-1 (XPDF) at Diamond Light Source using a modified Swagelok cell adapted for X-ray transmission (Figure 2.4c on page 10). Cells were prepared in an argon atmosphere glovebox (O_2, H_2O < 0.1 ppm) using metallic sodium (Sigma Aldrich, 99.9%) as an anode. The electrolyte was 2 M $NaPF_6$ (Acros, 98.5%) in propylene carbonate (Sigma Aldrich, anhydrous) with 5 w.t.% fluoroethylene carbonate (FEC; Sigma Aldrich, anhydrous). The separator was borosilicate glass fibre (Whatman, GF/A). Electrochemical measurements were performed using an Ivium-n-Stat battery cycler. The cell was held at 5 mV prior to the start of the experiment, the sodium anode replaced, then galvanostatically cycled in the potential range 0.005–2 V at a rate of C/30 (based on the mass of tin, corresponding to 3.75 Na per Sn in 30 hours).

Measurements were taken using an X-ray beam of energy 76 keV (λ = 0.1631 Å) and an amorphous silicon area detector (Perkin Elmer) in order to gather data to large values of momentum transfer.[110,111] Data were collected at 60 minute intervals, using a total exposure time of 60 s per scan.

Background measurements were taken using identical cells, but without the active material present. A Si standard was used to determine the sample geometry and the sample-to-detector distance. The data were converted to a function of intensity vs. Q using DAWN.[65] Standard corrections (background, Compton scattering, detector effects) were applied, and the data Fourier transformed to obtain $G(r)$ using the software PDFGetX3.[135] Structural refinements were performed using the DiffPy-CMI complex modelling infrastructure software.[88]

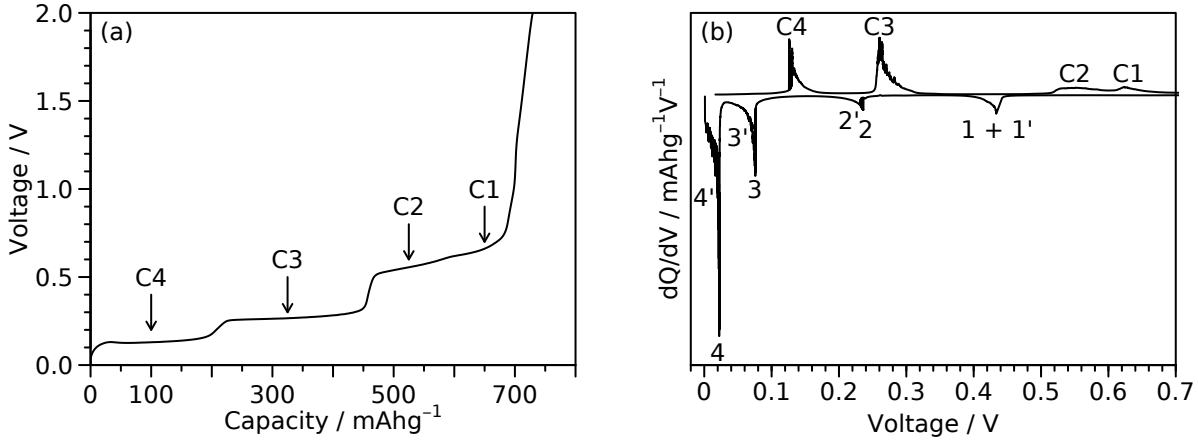

Figure 6.1: (a) Electrochemistry data for a sodium–tin cell cycled at a rate of C/20 (corresponding to achieving a capacity of 847 mA h g^{-1} in 20 hours) between 2 and 0.001 V (black line). Only the charge data are shown. Observed electrochemical processes are indicated with arrows. (b) Differential capacity data corresponding to the data shown in (a); discharge data for the same cell (Figure 5.1b on page 67) is also included).

6.2.3 Solid-State NMR Spectroscopy

Measurements were performed in an identical manner to section 5.2.4 on page 65, with the following exceptions: the electrolyte was 2 M $NaPF_6$ (Alfa Aesar, ≥99%) in propylene carbonate (Sigma Aldrich, anhydrous) with 5 w.t.% Fluoroethylene carbonate (FEC; Sigma Aldrich, anhydrous); and the cell was held at 5 mV prior to the start of the experiment, then galvanostatically cycled in the potential range 0.005–2.000 V at a rate of C/30 (based on the mass of tin, corresponding to 3.75 Na per Sn in 30 hours).

6.3 Results

6.3.1 Electrochemical Results

Figure 6.1a shows the experimental galvanostatic electrochemical profile obtained at a rate of C/20 and a temperature of 55 °C. In agreement with previous reports, we observe multiple electrochemical processes at potentials of approximately 0.13 V, 0.26 V, 0.54 V, and 0.63 V. We denote these as processes C4, C3, C2, and C1, respectively, such that the designated number for each process is the same as that for the discharge process that occurs at a similar potential. These names will be used throughout the subsequent text.

6.3.2 Overview of *Operando* Results

Operando PDF and ssNMR data are shown in Figure 6.2. It is apparent from the PDF data that there are three main regions during the charge phase: an period where the material is

crystalline, followed by an amorphous region with no strong ordering beyond the first peak at 2.96 Å, finally a return to crystallinity is observed after all sodium has been removed. PDFs obtained during the second discharge are similar to the first discharge (chapter 5) with four main regions during sodium insertion.

Operando ^{23}Na NMR spectra obtained during the first charge, second discharge and charge are presented in Figure 6.2b. Peaks at −10 ppm and 1140 ppm are observed throughout the measurement, and correspond to the $NaPF_6$ electrolyte and the sodium metal counter electrode, respectively. It is immediately obvious that sodium removal does not occur simply through the reverse of the mechanisms by which sodium is inserted. During process C4, we see the immediate disappearance of the peaks at −260 ppm (corresponding to $Na_{15+x}Sn_4$) and 180 ppm (residual $Na_{4.75}Sn_2$), and the appearance of a peak at 220 ppm. During process C3, the peak at 220 ppm shifts to 265 ppm, without any significant changes in peak shape. Following this (process C2), the peak at 265 ppm disappears and is replaced by a sharp peak at 43 ppm, which itself disappears during the final process (C1). During the second discharge, the same features are observed as in the first discharge. The second charge results in the same features as the first charge. Those peaks with a shift with magnitude greater than 100 ppm result from a Knight shift, which is indicative of metallic character of the material (section 2.3 on page 25).[78]

6.3.3 Process C4

Our previous work (chapter 5) has confirmed the final discharge (sodium insertion) product to be $Na_{15+x}Sn_4$. Unfortunately, experimental constraints at the beamline prevented the full conversion of the cell used for PDF measurements, the measured material being only approximately 16% $Na_{15}Sn_4$; there is also a trace amount of $Na_{4.75}Sn_2$ remaining in the cell used for NMR measurements.

Upon discharge, we found that a range of structures of the form $Na_{5-x}Sn_2$ ($R\bar{3}m$) formed at these potentials. This structure consists of tin dumbbells separated by sodium in two of the three crystallographic directions. By moving the dumbbells closer or further apart, different amounts of sodium can be accommodated. Crystallographically, this occurs by changing the occupancy of one of the three sodium sites (see Figure 5.14a on page 84 for an example of this). We found evidence for this occurring electrochemically through changing NMR shifts, finding (through comparison with PDF refinements) that higher shifts resulted from lower occupancies. The shift of the NMR peak formed during this process was found to be greater than those formed on the analogous discharge processes (220 ppm *vs.* 180–202 ppm). Our NMR data would therefore suggest that the mechanism for this electrochemical process could be explained by a transformation from $Na_{15+x}Sn_4$ to $Na_{5-x}Sn_2$ with $x > 0.6$. A refinement of a frame from our *operando* PDF data (Figure 6.3) performed whilst allowing the occupancy of this site to vary supports this, suggesting, in fact, that there is no sodium present on this site (i.e. $x = 1$). We therefore propose that this electrochemical process results in the conversion of $Na_{15+x}Sn_4$ into Na_2Sn).

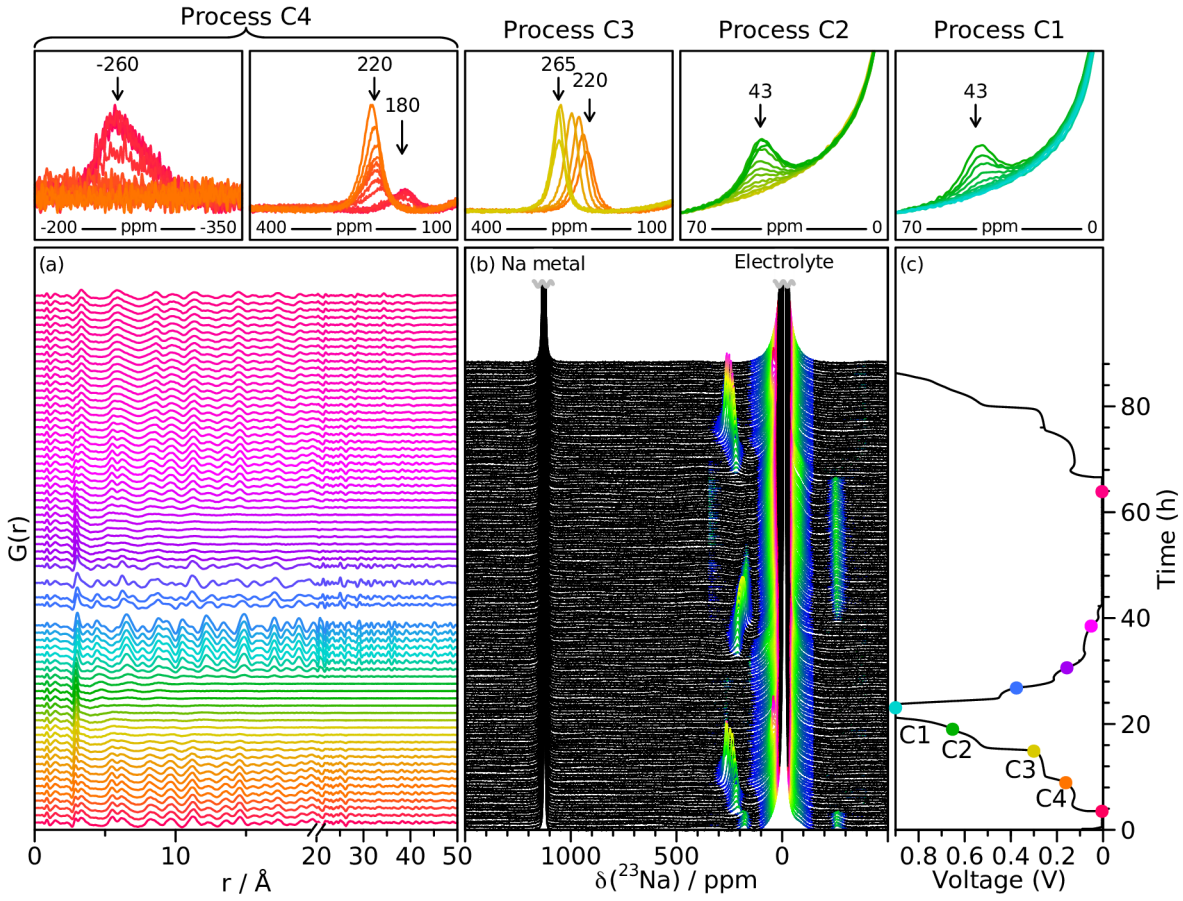

Figure 6.2: *Operando* measurements for electrochemical cells with sodium metal and tin electrodes, and a $NaPF_6$ electrolyte. (a) PDFs obtained during the first charge and second discharge are vertically offset in time; the colours correspond to the points shown on the electrochemical curve. (b) ^{23}Na NMR spectra obtained during the first charge, second discharge and second charge, aligned with the corresponding electrochemistry (c). Strong features corresponding largely to the electrolyte or metal have been truncated for clarity. Spectra are coloured in the region −500–1000 ppm according to their intensity. Selected regions are highlighted above, where the colours now correspond to the points shown on the electrochemical curve. The cells were cycled at a rate of C/30 (corresponding to achieving a capacity of 847 mA h g^{-1} in 30 hours) between 2–0.001 V, and held at the end of the first discharge prior to taking the PDF and NMR measurements. Gaps in the PDF data (a) occurred when the beamline was unable to collect data.

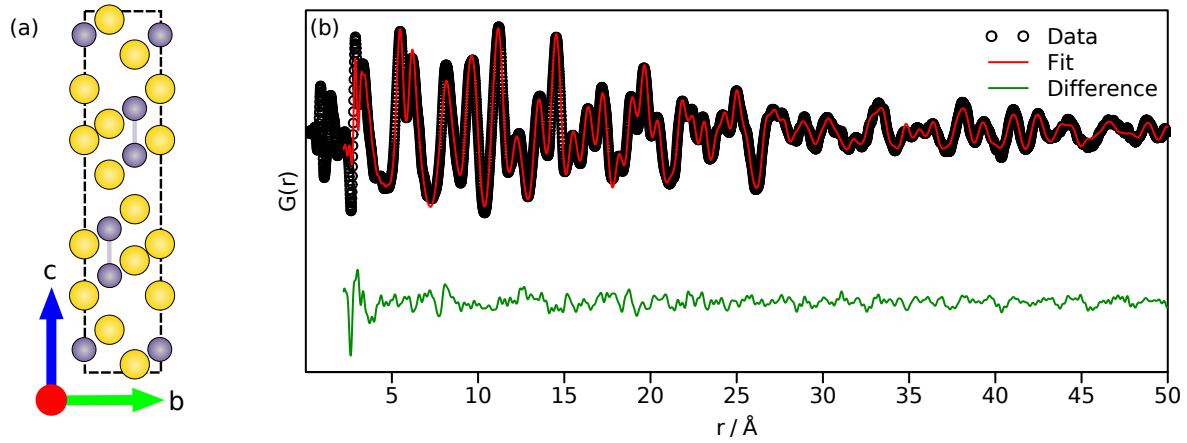

Figure 6.3: (a) A projection of the Na_2Sn structure (a special case of the $Na_{5-x}Sn_2$-type structures) viewed down the a-axis. Sodium atoms are shown in yellow, tin in grey, the unit cell is shown as a dashed black line. (b) Fit of the PDF corresponding to the first frame obtained during this process over the range 0–50 Å (R_w=0.21). Raw data are shown as black circles, the fit is shown as a red line, and the difference is shown as a green line offset below.

6.3.4 Process C3

During process C3, we see a shift in the NMR resonance by 45 ppm to 265 ppm. The relative similarity of the shift being indicative of only minor changes to the local sodium environments. Based on the previous discussion (section 6.3.3) we might expect this further shift towards higher frequencies to result from the further removal of sodium from the $Na_{5-x}Sn_2$ ($R\bar{3}m$) structure. However, the only site that has been found to have a variable occupancy is already devoid of sodium atoms. Our PDF data reveal a distinct loss of crystallinity during this stage of the charging mechanism. A single sharp peak at 2.96 Å is observed, with broad features at approximately 5.85 Å, 8.4 Å, 9.8 Å, 12.0 Å, and 14.1 Å. The PDF returns to the baseline beyond approximately 16 Å. Preliminary refinements of structures based on Na_2Sn with a spherical particle diameter of approximately 10 Å or less (Figure 6.4) suggest that the dumbbell motif is maintained (consistent with the NMR data), with some segregation of the sodium and tin atoms into distinct layers.

The shifting peak in the NMR could be indicative of a solid-solution type mechanism for this process. In order to test for this, intermediate data sets of this process were modelled using linear combinations of the end member data sets (Figure 6.5a). In principle, this can determine whether there are any other structures formed during this phase of the electrochemistry and / or significant changes to the structure of the phases that are formed in a solid-solution type mechanism. Each PDF was modelled by minimising x in the following equation:

$$\sum_a [G_i(r_a) - (xG_1(r_a) + (1-x)G_n(r_a))]^2 \tag{6.1}$$

Where $G_1(r)$, $G_n(r)$, and $G_i(r)$ correspond to the first, last, and ith PDF obtained during this process. The results show that all intermediate frames can be well modelled with a simple linear combination. As the PDF is strongly weighted towards the tin positions (tin having significantly more electrons than sodium) this suggests that the solid-solution behaviour

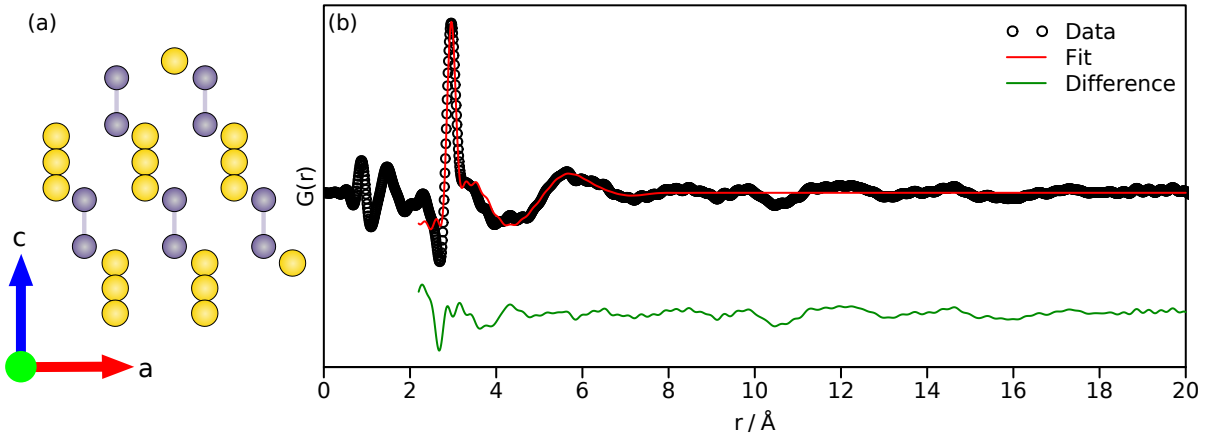

Figure 6.4: (a) A projection of the Na_2Sn-derived cluster used to fit the PDF in (b) viewed down the *b*-axis. Sodium atoms are shown in yellow, tin in grey. (b) Fit of the PDF corresponding to the first frame obtained during this process over the range 0–20 Å (R_w=0.31). Raw data are shown as black circles, the fit is shown as a red line, and the difference is shown as a green line offset below.

suggested by the NMR is primarily due to the positions of the sodium atoms, the tin positions being well explained by a two-phase reaction mechanism. We therefore propose that during this process Na_2Sn transforms into an amorphous phase consisting of tin-tin dumbbells with approximate composition $Na_{\approx 1.5}Sn$, the sodium content of this amorphous phase can change in a solid-solution type mechanism.

6.3.5 Process C2

Whilst our NMR data reveal a striking change during process C2 — the peak at 265 ppm being replaced by a sharp peak at 43 ppm — our PDF data suggests a much more subtle difference between the structures at the start and end of the process. Throughout this phase of the electrochemistry, the structure remains amorphous, with no notable correlations beyond approximately 15 Å; PDFs corresponding to the structures present at the beginning and end of this process are shown in Figure 6.6a. From DFT calculations, it is known that in the compositional range possible at this point in the electrochemistry, there is only one stable phase, NaSn (Figure 5.1a on page 67). NaSn consists of tin tetrahedra; whilst it is clearly kinetically unfavourable to form NaSn as a crystalline phase, it is possible that the amorphous tin-tin dumbbells could rearrange into tetrahedra during this process. The NMR peak at 43 ppm is within the expected region for tetrahedra (Figure 5.10 on page 80), and its unusual sharpness suggests a high degree of local ordering.

In order to test for the presence of tin tetrahedra, we prepared a model consisting of 8 such tetrahedra arranged on the corners of a cube. We calculated the reduced structure function $F(Q)$ for this model using the Debye equation, and the real-space PDF as its Fourier transform (see section 2.2.2 on page 19 for more details on the calculation method). We then refined the tin-tin bond length, the centre and orientation of each tetrahedra along with $delta_1$ (low-*r* peak sharpening parameter) and inter- and intra-tetrahedron isotropic thermal displacement parameters (the latter using the method outline by Billinge *et al.*).[91] Results are shown in

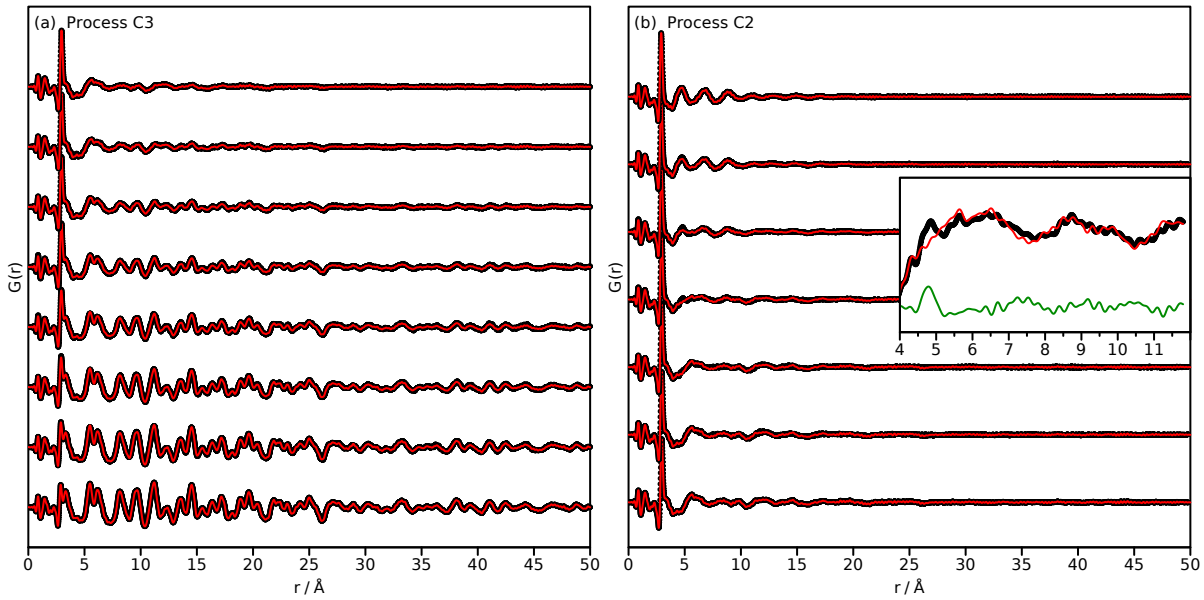

Figure 6.5: PDFs obtained during electrochemical process (a) C3 and (b) C2 fitted using a linear combinations of the PDFs from the start and end of the respective process. Black points correspond to the raw data, red lines to the fitted data. Inset: A close-up of the fit to the PDF obtained halfway through process C2 showing some deviation from two-phase behaviour. Black points correspond to the raw data, red lines to the fitted data, the green line offset below represents the difference.

Figure 6.7. In this preliminary model, there are no sodium atoms present; this may account for some of the discrepancies between the model and the experimental data. Nevertheless, it is clear that the data are adequately modelled using tetrahedra. Further work is needed to identify the likely location of sodium atoms within this model.

The electrochemical profile during this process is notably more sloping than the preceding processes. It is notable that previously reported electrochemistry data on very thin films also shows this behaviour,[41] suggesting that this is not simply a result of sluggish kinetics in our experimental setup. Typically sloping processes would indicate solid-solution behaviour. However, there are no peaks which shift significantly during this process in our NMR data. It is, however, possible that such a shift could be lost in the broad features inherent in static

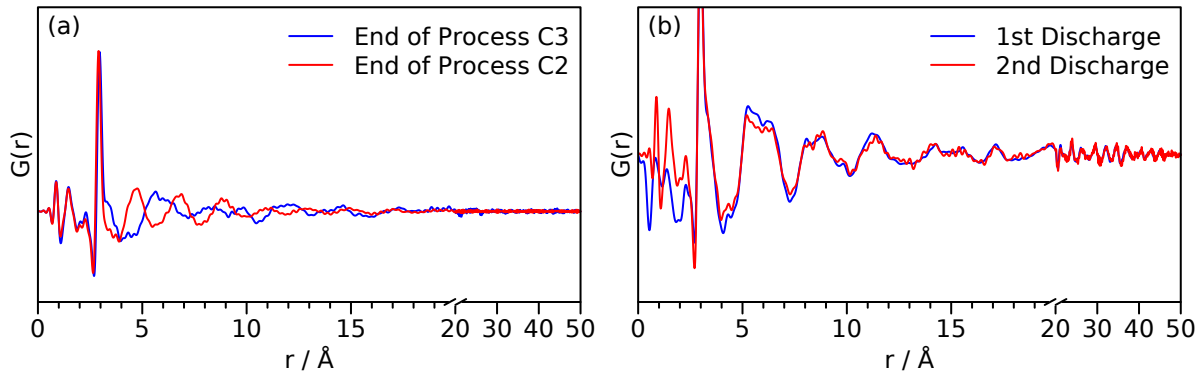

Figure 6.6: (a) A comparison of the PDFs for the amorphous phases formed at the end of processes C3 (blue) and C2 (red). (b) A comparison of PDFs for the amorphous phases formed on (blue) first discharge and (red) second discharge.

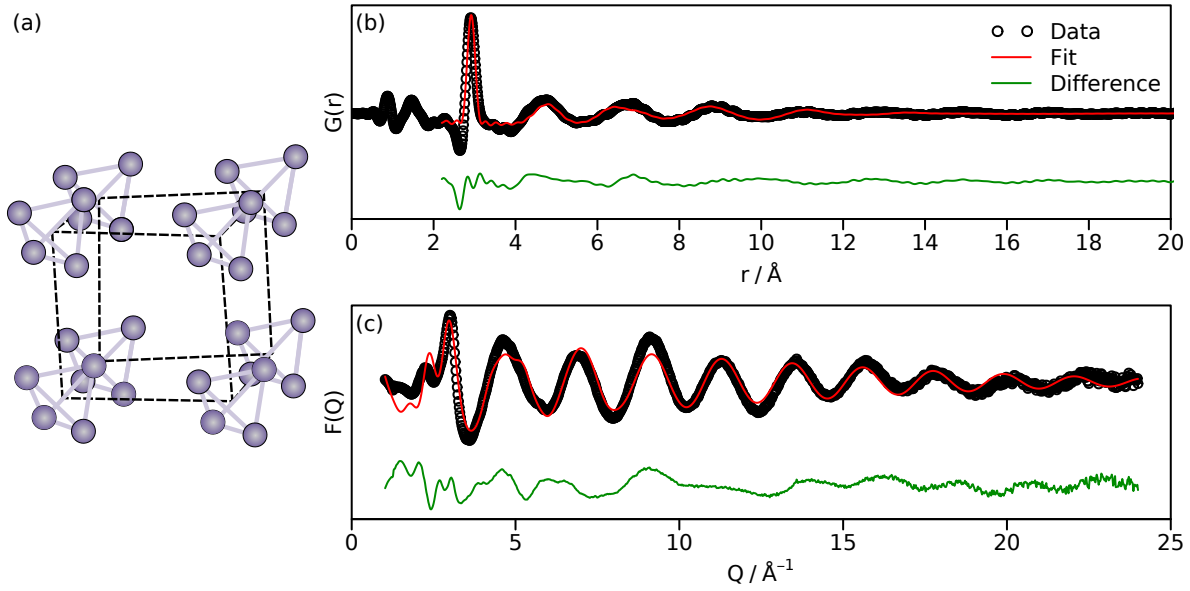

Figure 6.7: (a) The model of tin tetrahedra arranged on an approximately cubic lattice that was used to fit (b) and (c). The dashed lines join the centres of the tetrahedra. (b) Fit of the PDF corresponding to the first frame obtained during this process over the range 0–20 Å (R_w=0.32). (c) Fit of the reduced structure function $F(Q)$ corresponding to the first frame obtained during this process over the range 1–24 Å^{-1} (R_w=0.41). Raw data are shown as black circles, the fit is shown as a red line, and the difference is shown as a green line offset below.

ssNMR if it were sufficiently small, or that the change from a metallic phase to a diamagnetic phase has masked this information. We thus repeated the linear combination fitting used in process C3 for the PDF data obtained during this process. Results are shown in Figure 6.5b. Whilst the overall fit is good, there are some discrepancies between the measured data and the linear combination fit, particularly around halfway through the process. This may be evidence of solid solution behaviour, or of another intermediate phase; further work will be needed to confirm this.

6.3.6 Process C1

The final process on charge sees a return to the crystalline β-Sn structure (Figure 6.8). There are no notable distortions from the structure at the start of discharge. NMR data reveal only two regions of intensity: sodium metal at 1140 ppm and the electrolyte at −10 ppm. The electrolyte signal is notably broader than at the start of discharge, we attribute this to electrolyte breakdown to form the SEI layer resulting in additional diamagnetic contributions to the signal at similar shifts to the electrolyte. This confirms that no sodium–tin phases remain in the electrode following the completion of charging.

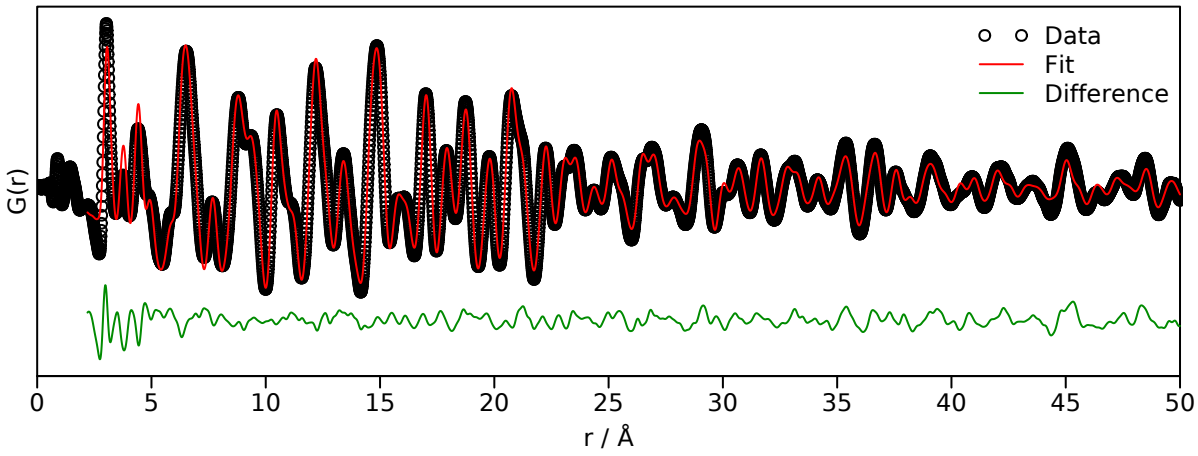

Figure 6.8: Fit of the PDF corresponding to the top of charge using a β-Sn model over the range 0–50 Å (R_w=0.18). Raw data are shown as black circles, the fit is shown as a red line, and the difference is shown as a green line offset below.

6.3.7 Beyond the First Cycle

Looking to the second discharge and beyond, we note that the return to a structure identical to the starting material means that it is unlikely that a different mechanism is followed on the second and subsequent cycles to the first. To confirm this, we collected PDF data for the second discharge, and NMR data for the second discharge and second charge (Figure 6.2). Unfortunately, software crashes at the beamline prevented some PDF data being saved during the initial stages of the second discharge. Both datasets are consistent with the data obtained for the first cycle. This is most obvious from the NMR data where it is clear that the peaks appear in the same places and shift in the same manner. It is also the case for the PDF data; an example is presented in Figure 6.6b where the most disordered phases from the first and second discharge are plotted together — a complex two-phase amorphous and crystalline structure discussed in section 5.3.6 on page 75.

6.4 Discussion

Based on our PDF, XRD, SSNMR measurements and theoretical calculations, we propose the following charge mechanism for the sodium–tin system):

Process C4: $Na_{15+x}Sn_4 \longrightarrow Na_2Sn$
Process C3: $Na_2Sn \longrightarrow a\text{-}Na_{\approx 1.5}Sn$
Process C2: $a\text{-}Na_{\approx 1.5}Sn \longrightarrow a\text{-}NaSn$
Process C1: $a\text{-}NaSn \longrightarrow Sn$

The first step in the sodium removal mechanism sees the reformation of tin-tin dumbbells from the isolated tin atoms in $Na_{15}Sn_4$ (and oversodiated forms). The particular structure formed is of the same type as those seen on discharge, however, a lower sodium content is found. Na_2Sn is found further from the convex hull than Na_5Sn_2, however, this difference is

only slight (0.14 eV).[136]

It is likely that on discharge the thermodynamic penalty of breaking the tin-tin bonds outweighs the difficulty in adding more sodium ions to the structure initially formed. Similarly, during charging, the system seeks to reform the tin-tin bonds as soon as possible, resulting in the nucleation and growth of the metastable phase with a lower sodium content (requiring less atomic reorganisation). This suggests that there may be some variation in the stoichiometry of this phase based on kinetic factors governed by the experimental setup, i.e. that setups with faster kinetics may favour the slightly more stable stoichiometries with higher sodium content.

Following the formation of Na_2Sn the system becomes amorphous, and remains that way until crystalline β-Sn is reformed at the top of charge. This is kinetically driven, the only stable crystalline phase at these compositions is NaSn — a phase with a low atomic mobility as evidenced by a high melting-point and low electrical conductivity.[132] We initially observe the retention of tin dumbbells, with the breakdown of long-range ordering a result of the removal of sodium from the structure, and kinetic difficulty in rearranging to the thermodynamically stable crystalline phase. Subsequently, the dumbbells rearrange into tetrahedra. Given that tetrahedra form the building block of NaSn, this is thermodynamically driven. Interestingly, the voltage calculated using crystalline NaSn (tetrahedra) for this process is 0.4 V, whereas that for the amorphous NaSn phase found on discharge (more chain-like connectivity) is 0.28 V.[136] The former being closer to the charge potential for this process and the latter closer to discharge. Whilst overpotentials play an important role in the difference between (dis)charge potentials, this is further evidence for the primary connectivity of this phase being tin tetrahedra.

Unusually for an alloying system, the insertion and subsequent removal of sodium ions from the structure does not result in an amorphous material. At the end of charge, we see a return to the crystalline starting material β-Sn. This is in contrast to other such systems, e.g. Li-Si,[114], Li-Ge,[129] and Na-Sb.[96] This means that the active material at the start of each cycle is identical, explaining the observation that subsequent cycles seem to follow the same sodium insertion / removal mechanisms. However, the propensity for forming crystalline phases, and the high number of kinetically driven transformations on both discharge and charge are suggestive of low sodium ion mobility. This is a likely reason for the comparatively poor rate capability of tin when compared to systems, such as Na-Sb, where the crystalline starting material does not reform.[42] This implies that significant work is required optimising the electrode formulation if tin, or tin-based, anode materials are to become viable. Much of this work is already ongoing, for example, tin nanofibres perform much better than the bulk metal, able to retain 776.3 mA h g^{-1} after 100 cycles *vs.* 125.3 mA h g^{-1} after 40 cycles for the bulk material.[137] Nanocompositing with carbon, has also been effective, having been shown to allow for a stable capacity of 415 mA h g^{-1} after 500 cycles at a rate of 1000 mA g^{-1}.[138]

6.5 Conclusions

The charge process of tin anodes was determined using *operando* PDF and ssNMR. We note in particular the formation of two distinct amorphous phases linked by an amorphous-to-amorphous phase transition. The first such phase bears a strong similarity to the crystalline Na_2Sn phase from which it forms. It consists of tin-tin dumbbells, separated by disordered sodium layers. The second phase has a local structure that tends more towards the thermodynamically stable crystalline NaSn phase. The principle tin-tin connectivity is tetrahedra, this strong local ordering giving an unusually sharp feature in our ssNMR spectra. Finally, we note that (similarly to the discharge mechanism) many of these transformations seem to lie under kinetic, rather than thermodynamic control. This suggests that optimisation of the electrode formulation will be vital to improve the rate-performance of tin anodes. Further work is necessary to confirm the structures formed, in particular, further PDF simulations and ^{119}Sn ssNMR measurements will help confirm the connectivity in the amorphous phases. Additional refinements of PDF data obtained during processes C3 and C2 could also provide further insights into possible solid-solution behaviour.

7 Conclusions and Future Work

The major objective of this thesis was to gain a better understanding of the mechanisms by which sodium inserts into different anode materials. To that end, two systems were chosen for study: hard carbons represent the anode material that is closest to commercialisation, yet the sodium insertion mechanism is still widely debated. Secondly, tin represents one of the highest capacity anode materials, its numerous electrochemical features suggesting an interesting (dis)charge mechanism. It has previously been shown that both of these systems proceed through disordered phases, and as such, we chose to focus on local structure probes for our structural characterisation. Furthermore, to avoid relaxation effects in metastable intermediates, much of this work used *operando* methods.

Chapter 3 presented *operando* ^{23}Na NMR data, demonstrating that sodium inserts into hard carbon in a two-phase mechanism. Initially, we see a single resonance close to 0 ppm, which is consistent with charge localisation, presumably near defects. At lower voltages, the ions become progressively more metallic, forming Na clusters or domains with coherence lengths of > 10 Å (as determined by *ex situ* PDF). PDF data further revealed that the graphene-like fragments exhibit significant curvature.

This work was expanded upon in chapter 4. Here, we looked at a number of different carbons, both commercially made and synthesised through the pyrolysis of glucose. We used a novel method to fit PDF data for the pristine materials: using curved aperiodic, stacked graphene layers to generate the simplest model (fewest number of atoms) that explains all features of the data. We then linked the different structural features to differences in the synthesis of the carbons. *Operando* measurements on the carbons demonstrated clearly the expansion of the shortest carbon-carbon bonds during the first electrochemical process, occurring simultaneously with the appearance of a new discorded phase in the PDF data. We further presented compelling evidence for the formation of sodium nano-clusters during the second process in the form of differential PDF data, which is almost identical for that calculated for sodium metal.

Chapter 5 presented an analysis of the discharge mechanism for tin anodes. We found sodium insertion to begin by conversion into $NaSn_2$, an interesting phase consisting of stanene layers separated by sodium ions. This conversion was not found to be simply a two-phase reaction, proceeding instead by an intermediate similar to $NaSn_2$, but with lower symmetry by virtue of containing some tin atoms within the sodium layers. Following this, we used RMC refinements of *ab initio* MD models to determine some structural features of the amorphous phase which forms next. We found that it consists primarily of chains of tin atoms, confirming this connectivity by means of ^{119}Sn NMR. We also used our PDF data to demonstrate that some exfoliation of any remaining $NaSn_2$ occurs in this region. The next process was found to result in the formation of structures of the form $Na_{5-x}Sn_2$. Detailed PDF refinements revealed evidence of solid-solution behaviour via a continual increase in occupancy of a single sodium site within the structure during this region of the electrochemistry. Finally, we observed the formation of $Na_{15}Sn_4$, and presented ^{23}Na NMR evidence for the possibility of further sodium storage as an off-stoichiometry phase $Na_{15+x}Sn_4$, by drawing analogies to the lithium–silicon

system.

The sodium removal (charge) process was investigated in chapter 6. We found significant differences from the discharge mechanism that have not previously been reported. Initially we see the conversion from $Na_{15}Sn_4$ to a similar $Na_{5-x}Sn_2$ dumbbell phase to that found on discharge. However, in this case both PDF and NMR data suggest no occupancy of the sodium site previously found to vary, i.e. Na_2Sn stoichiometry. Following this, the structure loses all long-range order. The resulting structure has significantly different local-ordering to the disordered phase found on discharge. We proposed that the major connectivity is tin-tin dumbbells owing to the similarity of the NMR shift to the previous phase, preliminary PDF refinements were shown to support this. A second amorphous phase is then found with lower sodium content. Its diamagnetic nature, and unusually sharp NMR peak, suggesting that the immediate connectivity is tin tetrahedra as found in the only thermodynamically stable phase around this composition. Further support of this came in the form of PDF refinements of tin tetrahedra arranged on a distorted primitive cubic lattice. This model was found to give a good fit to our data, discrepancies being attributed to a lack of sodium atoms in the model. Finally, we see a return to β-tin, with no crystalline intermediate analogous to $NaSn_2$ being found.

Overall, we have demonstrated the success of PDF and NMR as local structural probes for the analysis of complex electrochemical behaviour. Further work is necessary to expand the analysis of the sodium-hard carbon system to additional carbons, and to provide further evidence in support of, or against, the proposed mechanisms for sodium insertion. The techniques developed, in particular the notion of an amorphous analogue to a unit cell, could then be applied to other carbon based materials, for example the higher surface area carbons typically used in supercapacitors. The suggested mechanism for charging tin anodes also requires further confirmation; NMR measurements could confirm the proposed tin coordination, which would assist in more detailled modelling of the PDF data already acquired. In addition, the metastability observed in some of the sodium–tin alloys upon removal of the applied current, has not been investigated in detail. For practical applications of battery materials, understanding of these relaxation processes is particularly important as batteries are not typically subject to a continuous current drain outside of research. Furthermore, there are many more systems that exhibit complex behaviour precluding analysis by conventional techniques. For example, binary and ternary alloys are frequently reported to improve on the electrochemical performance of their single component cousins, but often lack any long-range order following electrochemical reactions. A focus on local structural techniques will prove vital to understand how they work, and ultimately in designing new materials with improved functionality.

References

(1) Department for Business, Energy & Industrial Strategy *Digest of UK Energy Statistics (DUKES)*; 2018.

(2) Sabihuddin, S.; Kiprakis, A. E.; Mueller, M. *Energies* **2015**, *8*, 172–216.

(3) Sternberg, A.; Bardow, A. *Energy Environ. Sci.* **2015**, *8*, 389–400.

(4) International Energy Agency *Technology Roadmap: Energy Storage*; 2014.

(5) Whittingham, M. S. *Chemical Reviews* **2004**, *104*, 4271–4302.

(6) Wakihara, M.; Yamamoto, O., *Lithium ion batteries: fundamentals and performance*; Kodansha: 1998.

(7) Jaskula, B. W. *Lithium*; U.S. Geological Survey, 2009.

(8) Jaskula, B. W. *Lithium*; U.S. Geological Survey, 2011.

(9) Tahil, W. *The trouble with lithium*; Meridian International Research, 2008.

(10) Evans, R. K. An abundance of lithium, http://www.evworld.com/library/KEvans_LithiumAbunance_pt2.pdf (accessed 30/09/2018).

(11) Evans, R. K. *Northern Miner* **2010**, *96*, 2–6.

(12) Yaksic, A.; Tilton, J. E. *Resources Policy* **2009**, *34*, 185–194.

(13) Sverdrup, H. U. *Resources, Conservation and Recycling* **2016**, *114*, 112–129.

(14) Peters, J.; Weil, M. *Resources* **2016**, *5*, 46.

(15) S&P Global Market Intelligence Battery Watch – Lithium in focus, pages.marketintelligence.spglobal.com/Lithium-in-focus-MS.html (accessed 30/09/2018).

(16) British Geological Survey World mineral statistics archive, www.bgs.ac.uk/mineralsuk/statistics/worldArchive.html (accessed 30/09/2018).

(17) Yabuuchi, N.; Kubota, K.; Dahbi, M.; Komaba, S. *Chemical Reviews* **2014**, *114*, 11636–11682.

(18) Haynes, W. M. *CRC Handboox of Chemistry and Physics. 92nd Edition*.

(19) Ong, S. P.; Chevrier, V. L.; Hautier, G.; Jain, A.; Moore, C.; Kim, S.; Ma, X.; Ceder, G. *Energy & Environmental Science* **2011**, *4*, 3680–3688.

(20) Ma, X.; Chen, H.; Ceder, G. *Journal of The Electrochemical Society* **2011**, *158*, A1307–A1312.

(21) Harry, K. J.; Hallinan, D. T.; Parkinson, D. Y.; Macdowell, A. A.; Balsara, N. P. *Nature materials* **2013**, *13*, 69–73.

(22) Ge, P.; Fouletier, M. *Solid State Ionics* **1988**, *28–30*, 1172–1175.

(23) Doeff, M. M.; Ma, Y.; Visco, S. J.; De Jonghe, L. C. *Journal of The Electrochemical Society* **1993**, *140*, L169–L170.

(24) Stevens, D. A.; Dahn, J. R. *Journal of The Electrochemical Society* **2001**, *148*, A803–A811.

(25) Slater, M. D.; Kim, D.; Lee, E.; Johnson, C. S. *Advanced Functional Materials* **2013**, *23*, 947–958.

(26) Kim, S.-W.; Seo, D.-H.; Ma, X.; Ceder, G.; Kang, K. *Advanced Energy Materials* **2012**, *2*, 710–721.

(27) Wen, Y.; He, K.; Zhu, Y.; Han, F.; Xu, Y.; Matsuda, I.; Ishii, Y.; Cumings, J.; Wang, C. *Nature Communications* **2014**, *5*, 1–10.

(28) Tsai, P.-c.; Chung, S.-C.; Lin, S.-k.; Yamada, A. *Journal of Materials Chemistry A* **2015**, *3*, 9763–9768.

(29) Dresselhaus, M. S.; Dresselhaus, G. *Advances in Physics* **1981**, *30*, 139–326.

(30) Komaba, S.; Hasegawa, T.; Dahbi, M.; Kubota, K. *Electrochemistry Communications* **2015**, *60*, 172–175.

(31) Wang, Z.; Selbach, S. M.; Grande, T. *RSC Advances* **2014**, *4*, 4069–4079.

(32) Franklin, R. E. *Proceedings of the Royal Society A: Mathematical, Physical and Engineering Sciences* **1951**, *209*, 196–218.

(33) Bommier, C.; Mitlin, D.; Ji, X. *Progress in Materials Science* **2018**, *97*, 170–203.

(34) Irisarri, E.; Ponrouch, A.; Palacin, M. R. *Journal of The Electrochemical Society* **2015**, *162*, A2476–A2482.

(35) Besenhard, J.; Yang, J.; Winter, M. *Journal of Power Sources* **1997**, *68*, 87–90.

(36) Todd, A. D. W.; Ferguson, P. P.; Fleischauer, M. D.; Dahn, J. R. *International Journal of Energy Research* **2010**, *34*, 535–555.

(37) Zhang, W. J. *Journal of Power Sources* **2011**, *196*, 13–24.

(38) Komaba, S.; Matsuura, Y.; Ishikawa, T.; Yabuuchi, N.; Murata, W.; Kuze, S. *Electrochemistry Communications* **2012**, *21*, 65–68.

(39) Xiao, L.; Cao, Y.; Xiao, J.; Wang, W.; Kovarik, L.; Nie, Z.; Liu, J. *Chemical Communications* **2012**, *48*, 3321–3323.

(40) Datta, M. K.; Epur, R.; Saha, P.; Kadakia, K.; Park, S. K.; Kumta, P. N. *Journal of Power Sources* **2013**, *225*, 316–322.

(41) Baggetto, L.; Ganesh, P.; Meisner, R. P.; Unocic, R. R.; Jumas, J.-C.; Bridges, C. A.; Veith, G. M. *Journal of Power Sources* **2013**, *234*, 48–59.

(42) Lao, M.; Zhang, Y.; Luo, W.; Yan, Q.; Sun, W.; Dou, S. X. *Advanced Materials* **2017**, *1700622*, 1–23.

(43) Chevrier, V. L.; Ceder, G. *Journal of The Electrochemical Society* **2011**, *158*, A1011–A1014.

(44) Kohandehghan, A.; Cui, K.; Kupsta, M.; Ding, J.; Memarzadeh Lotfabad, E.; Kalisvaart, W. P.; Mitlin, D. *Nano Letters* **2014**, *14*, 5873–5882.

(45) Ellis, L. D.; Wilkes, B. N.; Hatchard, T. D.; Obrovac, M. N. *Journal of The Electrochemical Society* **2014**, *161*, A416–A421.

(46) Jung, S. C.; Jung, D. S.; Choi, J. W.; Han, Y. K. *Journal of Physical Chemistry Letters* **2014**, *5*, 1283–1288.

(47) Winter, M.; Brodd, R. J. *Chemical Reviews* **2004**, *104*, 4245–4270.

(48) Nernst, W. *Zeitschrift für Physikalische Chemie* **1889**, *4U*, 129–181.

(49) IUPAC, *Compendium of Chemical Terminology, 2nd ed. (the "Gold Book")*; Blackwell Scientific Publications, Oxford: 1997.

(50) Tarascon, J.-M.; Armand, M. *Nature* **2001**, *414*, 359–367.

(51) Weppner, W.; Huggins, R. A. *Journal of The Electrochemical Society* **1977**, *124*, 1569.

(52) Wen, C. J.; Boukamp, B. A.; Huggins, R. A.; Weppner, W. *Journal of The Electrochemical Society* **1979**, *126*, 2258.

(53) Borkiewicz, O. J.; Shyam, B.; Wiaderek, K. M.; Kurtz, C.; Chupas, P. J.; Chapman, K. W. *Journal of Applied Crystallography* **2012**, *45*, 1261–1269.

(54) Egami, T.; Billinge, S. J., *Underneath the Bragg Peaks*; Pergamon: 2003; Vol. 16.

(55) Juhás, P.; Granlund, L.; Duxbury, P. M.; Punch, W. F.; Billinge, S. J. *Acta Crystallographica Section A: Foundations of Crystallography* **2008**, *64*, 631–640.

(56) Farrow, C. L.; Billinge, S. J. L. *Acta Crystallographica Section A: Foundations of Crystallography* **2009**, *65*, 232–239.

(57) Kodama, K.; Iikubo, S.; Taguchi, T.; Shamoto, S.-i. *Acta Crystallographica Section A Foundations of Crystallography* **2006**, *62*, 444–453.

(58) Stevens, D. A.; Dahn, J. R. *Journal of The Electrochemical Society* **2000**, *147*, 1271–1273.

(59) Stevens, D. A.; Dahn, J. R. *Journal of The Electrochemical Society* **2000**, *147*, 4428–4431.

(60) Gotoh, K.; Ishikawa, T.; Shimadzu, S.; Yabuuchi, N.; Komaba, S.; Takeda, K.; Goto, A.; Deguchi, K.; Ohki, S.; Hashi, K.; Shimizu, T.; Ishida, H. *Journal of Power Sources* **2013**, *225*, 137–140.

(61) Bommier, C.; Surta, T. W.; Dolgos, M.; Ji, X. *Nano Letters* **2015**, *15*, 5888–5892.

(62) Zhang, B.; Ghimbeu, C. M.; Laberty, C.; Vix-Guterl, C.; Tarascon, J. M. *Advanced Energy Materials* **2016**, *6*, 1–9.

(63) Matei Ghimbeu, C.; Górka, J.; Simone, V.; Simonin, L.; Martinet, S.; Vix-Guterl, C. *Nano Energy* **2018**, *44*, 327–335.

(64) Jin, Y.; Sun, S.; Ou, M.; Liu, Y.; Fan, C.; Sun, X.; Peng, J.; Li, Y.; Qiu, Y.; Wei, P.; Deng, Z.; Xu, Y. et al. *ACS Applied Energy Materials* **2018**, *1*, acsaem.8b00354.

(65) Basham, M.; Filik, J.; Wharmby, M. T.; Chang, P. C. Y.; El Kassaby, B.; Gerring, M.; Aishima, J.; Levik, K.; Pulford, B. C. A.; Sikharulidze, I.; Sneddon, D.; Webber, M. et al. *Journal of Synchrotron Radiation* **2015**, *22*, 853–858.

(66) Qiu, X.; Thompson, J. W.; Billinge, S. J. L. *Journal of Applied Crystallography* **2004**, *37*, 678.

(67) Farrow, C. L.; Juhas, P.; Liu, J. W.; Bryndin, D.; Boin, E. S.; Bloch, J.; Proffen, T.; Billinge, S. J. L. *Journal of Physics: Condensed Matter* **2007**, *19*, 335219.

(68) Pecher, O.; Bayley, P. M.; Liu, H.; Liu, Z.; Trease, N. M.; Grey, C. P. *Journal of Magnetic Resonance* **2016**, *265*, 200–209.

(69) Harris, R. K.; Becker, E. D. *Journal of Magnetic Resonance* **2002**, *156*, 323–326.

(70) Wojdyr, M. *Journal of Applied Crystallography* **2010**, *43*, 1126–1128.

(71) Hayashi, S.; Hayamizu, K. *Bulletin of the Chemical Society of Japan* **1989**, *62*, 2429–2430.

(72) Forse, A. C.; Merlet, C.; Allan, P. K.; Humphreys, E. K.; Griffin, J. M.; Aslan, M.; Zeiger, M.; Presser, V.; Gogotsi, Y.; Grey, C. P. *Chemistry of Materials* **2015**, *27*, 6848–6857.

(73) Dowell, M.; Howard, R. *Carbon* **1986**, *24*, 311–323.

(74) Kureha Battery Materials Japan Co., Ltd. – Carbotron P(J), www.kureha.co.jp/development/story/pdf/catalog_hc_eg_20120924.pdf (accessed 01/09/2018).

(75) Petkov, V.; Difrancesco, R. G.; Billinge, S. J. L.; Acharya, M.; Foley, H. C. *Philosophical Magazine Part B* **1999**, *79*, 1519–1530.

(76) Dahn, J. R.; Zheng, T.; Liu, Y.; Xue, J. S. *Science* **1995**, *270*, 590–593.

(77) Blanc, F.; Leskes, M.; Grey, C. P. *Accounts of Chemical Research* **2013**, *46*, 1952–1963.

(78) Trease, N. M.; Zhou, L.; Chang, H. J.; Zhu, B. Y.; Grey, C. P. *Solid State Nuclear Magnetic Resonance* **2012**, *42*, 62–70.

(79) Lazzeretti, P. *Progress in Nuclear Magnetic Resonance Spectroscopy* **2000**, *36*, 1–88.

(80) Forse, A. C.; Griffin, J. M.; Presser, V.; Gogotsi, Y.; Grey, C. P. *The Journal of Physical Chemistry C* **2014**, *118*, 7508–7514.

(81) Letellier, M.; Chevallier, F.; Clinard, C.; Frackowiak, E.; Rouzaud, J.-N.; Béguin, F.; Morcrette, M.; Tarascon, J.-M. *The Journal of Chemical Physics* **2003**, *118*, 6038–6045.

(82) Letellier, M.; Chevallier, F.; Béguin, F.; Frackowiak, E.; Rouzaud, J.-N. *Journal of Physics and Chemistry of Solids* **2004**, *65*, 245–251.

(83) Bommier, C.; Luo, W.; Gao, W.-y.; Greaney, A.; Ma, S.; Ji, X. *Carbon* **2014**, *76*, 165–174.

(84) Ding, J.; Zhou, H.; Zhang, H.; Stephenson, T.; Li, Z.; Karpuzov, D.; Mitlin, D. *Energy and Environmental Science* **2017**, *10*, 153–165.

(85) Alcántara, R.; Lavela, P.; Ortiz, G. F.; Tirado, J. L. *Electrochemical and Solid-State Letters* **2005**, *8*, A222–A225.

(86) Morita, R.; Gotoh, K.; Fukunishi, M.; Kubota, K.; Komaba, S.; Nishimura, N.; Yumura, T.; Deguchi, K.; Ohki, S.; Shimizu, T.; Ishida, H. *Journal of Materials Chemistry A* **2016**, *4*, 13183–13193.

(87) Deringer, V. L.; Merlet, C.; Hu, Y.; Lee, T. H.; Kattirtzi, J. A.; Pecher, O.; Csányi, G.; Elliott, S. R.; Grey, C. P. *Chemical Communications* **2018**, *54*, 5988–5991.

(88) Juhás, P.; Farrow, C. L.; Yang, X.; Knox, K. R.; Billinge, S. J. *Acta Crystallographica Section A: Foundations and Advances* **2015**, *71*, 562–568.

(89) Newport, R. J.; Honeybone, P. J.; Cottrell, S. P.; Franks, J.; Revell, P.; Cernik, R. J.; Howells, W. S. *Surface and Coatings Technology* **1991**, *47*, 668–676.

(90) Opletal, G.; Petersen, T.; O'Malley, B.; Snook, I.; Mcculloch, D. G.; Marks, N. A.; Yarovsky, I. *Molecular Simulation* **2002**, *28*, 927–938.

(91) Prill, D.; Juhás, P.; Schmidt, M. U.; Billinge, S. J. *Journal of Applied Crystallography* **2015**, *48*, 171–178.

(92) Tucker, M. G.; Dove, M. T.; Keen, D. A. *Journal of Applied Crystallography* **2001**, *34*, 630–638.

(93) Nixon, D. E.; Parry, G. S. *Journal of Physics C: Solid State Physics* **1969**, *2*, 1732–1741.

(94) Li, Z.; Bommier, C.; Chong, Z. S.; Jian, Z.; Surta, T. W.; Wang, X.; Xing, Z.; Neuefeind, J. C.; Stickle, W. F.; Dolgos, M.; Greaney, P. A.; Ji, X. *Advanced Energy Materials* **2017**, *1602894*, 1602894.

(95) Dahn, J. R.; Xing, W.; Gao, Y. *Carbon* **1997**, *35*, 825–830.

(96) Darwiche, A.; Marino, C.; Sougrati, M. T.; Fraisse, B.; Stievano, L.; Monconduit, L. *Journal of the American Chemical Society* **2012**, *134*, 20805–20811.

(97) Baggetto, L.; Keum, J. K.; Browning, J. F.; Veith, G. M. *Electrochemistry Communications* **2013**, *34*, 41–44.

(98) Zhou, D.; Slater, M.; Kim, D.; Lee, E.; Jorne, J.; Johnson, C. *ECS Transactions* **2014**, *58*, 59–64.

(99) Wu, L.; Hu, X.; Qian, J.; Pei, F.; Wu, F.; Mao, R.; Ai, X.; Yang, H.; Cao, Y. *Journal of Materials Chemistry A* **2013**, *1*, 7181–7184.

(100) Prikhodchenko, P. V.; Yu, D. Y. W.; Batabyal, S. K.; Uvarov, V.; Gun, J.; Sladkevich, S.; Mikhaylov, A. A.; Medvedev, A. G.; Lev, O. *Journal of Materials Chemistry A* **2014**, *2*, 8431–8437.

(101) Zhu, J.; Deng, D. *The Journal of Physical Chemistry C* **2015**, *119*, 21323–21328.

(102) Kremann, R.; Gmachl-Pammer, J. *Zeitschrift für Metallkunde* **1920**, *12*, 257.

(103) Crouch-Baker, S.; Deublein, G.; Tsai, H.-C.; Zhou, L. Z.; Huggins, R. A. *Solid State Ionics* **1990**, *42*, 109–115.

(104) Inoue, T.; Saito, M.; Fujimoto, M.; Itaya, M., U.S. Patent Application 20070218361, 2007.

(105) Inorganic Crystal Structure Database, icsd.fiz-karlsruhe.de (accessed 31/01/2017).

(106) Ellis, L. D.; Hatchard, T. D.; Obrovac, M. N. *Journal of the Electrochemical Society* **2012**, *159*, A1801–A1805.

(107) Wang, J. W.; Liu, X. H.; Mao, S. X.; Huang, J. Y. *Nano letters* **2012**, *12*, 5897–5902.

(108) Li, Z.; Ding, J.; Mitlin, D. *Accounts of Chemical Research* **2015**, *48*, 1657–1665.

(109) Baggetto, L.; Bridges, C. A.; Jumas, J.-C.; Mullins, D. R.; Carroll, K. J.; Meisner, R. a.; Crumlin, E. J.; Liu, X.; Yang, W.; Veith, G. M. *Journal of Materials Chemistry A* **2014**, *2*, 18959–18973.

(110) Chupas, P. J.; Qiu, X.; Hanson, J. C.; Lee, P. L.; Grey, C. P.; Billinge, S. J. L. *Journal of Applied Crystallography* **2003**, *36*, 1342–1347.

(111) Chupas, P. J.; Chapman, K. W.; Lee, P. L. *Journal of Applied Crystallography* **2007**, *40*, 463–470.

(112) Hammersley, A. P.; Svensson, S. O.; Hanfland, M.; Fitch, A. N.; Hausermann, D. *High Pressure Research* **1996**, *14*, 235–248.

(113) Tucker, M. G.; Keen, D. A.; Dove, M. T.; Goodwin, A. L.; Hui, Q. *Journal of Physics: Condensed Matter* **2007**, *19*, 335218.

(114) Ogata, K.; Salager, E.; Kerr, C. J.; Fraser, A. E.; Ducati, C.; Morris, A. J.; Hofmann, S.; Grey, C. P. *Nature Communications* **2014**, *5*, 3217.

(115) Clayden, N. J.; Dobson, C. M.; Fern, A. *Journal of the Chemical Society, Dalton Transactions* **1989**, 843.

(116) Fässler, T. F.; Kronseder, C. *Angewandte Chemie International Edition* **1998**, *37*, 1571–1575.

(117) Fässler, T. F.; Hoffmann, S. *Inorganic Chemistry* **2003**, *42*, 5474–5476.

(118) Dubois, F.; Schreyer, M.; Fässler, T. F. *Inorganic Chemistry* **2005**, *44*, 477–479.

(119) Müller, W.; Volk, K. *Zeitschrift für Naturforschung B* **1978**, *33*, 275–278.

(120) Su, D.; Xie, X.; Wang, G. *Chemistry – A European Journal* **2014**, *20*, 3192–3197.

(121) Wang, Y.-X.; Lim, Y.-G.; Park, M.-S.; Chou, S.-L.; Kim, J. H.; Liu, H.-K.; Dou, S.-X.; Kim, Y.-J. *Journal of Materials Chemistry A* **2014**, *2*, 529–534.

(122) Klösters, G.; Jansen, M. *Solid State Nuclear Magnetic Resonance* **2000**, *16*, 279–283.

(123) Basu, S.; Zeller, C.; Flanders, P.; Fuerst, C.; Johnson, W.; Fischer, J. *Materials Science and Engineering* **1979**, *38*, 275–283.

(124) Allan, P. K.; Griffin, J. M.; Darwiche, A.; Borkiewicz, O. J.; Wiaderek, K. M.; Chapman, K. W.; Morris, A. J.; Chupas, P. J.; Monconduit, L.; Grey, C. P. *Journal of the American Chemical Society* **2016**, *138*, 2352–2365.

(125) Wiaderek, K. M.; Borkiewicz, O. J.; Castillo-Martínez, E.; Robert, R.; Pereira, N.; Amatucci, G. G.; Grey, C. P.; Chupas, P. J.; Chapman, K. W. *Journal of the American Chemical Society* **2013**, *135*, 4070–4078.

(126) Lu, J.; Yang, J.-x.; Wang, J.; Lim, A.; Wang, S.; Loh, K. P. *ACS Nano* **2009**, *3*, 2367–2375.

(127) Shannon, R. D. *Acta Crystallographica Section A* **1976**, *32*, 751–767.

(128) Nam, D.-H.; Hong, K.-S.; Lim, S.-J.; Kim, T.-H.; Kwon, H.-S. *The Journal of Physical Chemistry C* **2014**, *118*, 20086–20093.

(129) Jung, H.; Allan, P. K.; Hu, Y.-Y.; Borkiewicz, O. J.; Wang, X.-L.; Han, W.-Q.; Du, L.-S.; Pickard, C. J.; Chupas, P. J.; Chapman, K. W.; Morris, A. J.; Grey, C. P. *Chemistry of Materials* **2015**, *27*, 1031–1041.

(130) Key, B.; Morcrette, M.; Tarascon, J.-M.; Grey, C. P. *Journal of the American Chemical Society* **2011**, *133*, 503–512.

(131) Choi, H. J.; Roundy, D.; Sun, H.; Cohen, M. L.; Louie, S. G. *Nature* **2002**, *418*, 758–760.

(132) Sangster, J.; Bale, C. W. *Journal of Phase Equilibria* **1998**, *19*, 76–81.

(133) Morris, A. J.; Grey, C. P.; Pickard, C. J. *Physical Review B* **2014**, *90*, 054111.

(134) Cheng, Y.; Huang, J.; Li, R.; Xu, Z.; Cao, L.; Ouyang, H.; Li, J.; Qi, H.; Wang, C. *Electrochimica Acta* **2015**, *180*, 227–233.

(135) Juhás, P.; Davis, T.; Farrow, C. L.; Billinge, S. J. *Journal of Applied Crystallography* **2013**, *46*, 560–566.

(136) Stratford, J. M.; Mayo, M.; Allan, P. K.; Pecher, O.; Borkiewicz, O. J.; Wiaderek, K. M.; Chapman, K. W.; Pickard, C. J.; Morris, A. J.; Grey, C. P. *Journal of the American Chemical Society* **2017**, *139*, 7273–7286.

(137) Nam, D. H.; Kim, T. H.; Hong, K. S.; Kwon, H. S. *ACS Nano* **2014**, *8*, 11824–11835.

(138) Liu, Y.; Zhang, N.; Jiao, L.; Tao, Z.; Chen, J. *Advanced Functional Materials* **2015**, *25*, 214–220.